Numerical Simulation of Impurity Transport in Tokamak Edge Plasmas

February 2018

Shohei YAMOTO

Numerical Simulation of Impurity Transport in Tokamak Edge Plasmas

Shohei YAMOTO

Adviser : Akiyoshi HATAYAMA

February 2018

Keio University
Graduate School of Science and Technology
School of Fundamental Science and Technology

A thesis submitted for the degree of
Doctor of Philosophy in Engineering

Contents

Chapter 1

Introduction

1.1 Energy resource problems and nuclear fusion

To develop new energy resources is one of the critical issues regarding the sustainable prosperity of the human beings. In these days, various approaches to obtain eco-friendly energy are being developed such as wind energy, and solar energy. However, these kinds of power generation cannot cover a baseload power supply. Therefore, it is very difficult to cover the whole energy demands. In order to obtain CO_2-free stable energy, the nuclear fusion energy is considered as one of the most promising candidates for alternative energy resources of the future. The nuclear fusion reacter achieves energy by means of the nuclear fusion reaction of light atoms.

The *nuclear fusion reaction* (abbreviated *fusion*) is a reaction where lighter atomic nuclei fuse together to make a heavier nucleus. In a such fusion process, the mass deffect $\varDelta m$, which causes enormous energy gain through the fusion reaction, takes place. The amount of the obtained enegy can be described by the relativistic theory ($\varDelta E = c^2 \varDelta m$, where c is the speed of light).

A reaction between the hydrogen isotopes, i.e., deuterium (D) and tritium (T), is now considered as the most feasible candidate for the controlled fusion. The reaction is called D-T reaction (Fig. 1.1).

$$^{2}\mathrm{D} + {}^{3}\mathrm{T} \longrightarrow {}^{4}\mathrm{He}(3.52\,\mathrm{MeV}) + {}^{1}\mathrm{n}(14.06\,\mathrm{MeV}). \tag{1.1}$$

The energy production by the D-T reaction has the following advantages.

Abundance: The deuterium and tritium are in ample supply [1]. The deuterium is obtained by hydrolysis of the sea water, in economically sustainable way. The tritium is produced by neutron bombardment on lithium, which is also available in abundance.

Safety: The D-T reaction stops immediately if the power supply to the plant stops. Therefore,

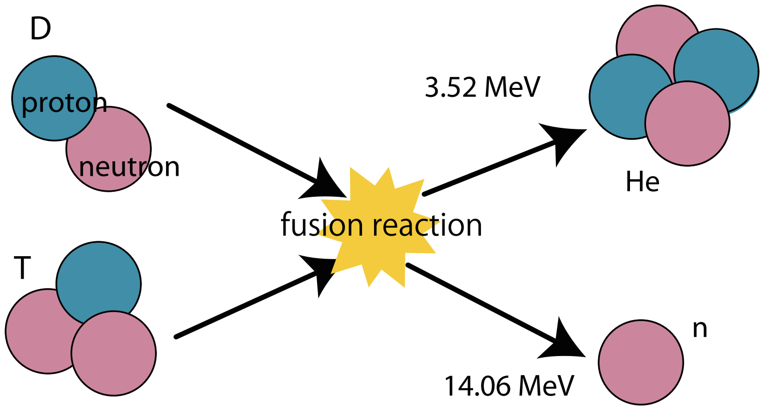

Figure 1.1: The schematic view of the D-T fusion reaction.

there are no worries of a loss-of-coolant accident like a fission reaction of uranium. However, it should be noted that the fusion plant handles radioactive elements such as tritium. These must be handled in a well organized method. Even though, the hazard potential of tritium is 10^{-3} times lower than typical fission products such as iodine-131.

The fusion reaction rate coefficients as a function of the temperature are shown in Fig. 1.2. As seen from Fig. 1.2, the D-T reaction reaches the peak of the rate coeffient at 40 keV, which means more than 100 milion K. In order to achieve the continuous D-T fusion reaction, we have to keep the temperature at that high.

At such high temperature, all atoms are ionized. The heated D-T gas becomes an electrically neutral mixture of ions and electrons, defined as *plasma*. We keep such D-T plasma (hereafter, we simply express D-T plasma as *fuel plasma*) in a stable state, for the fusion reactions to occur continuously.

A performance of fusion reactors is described by a product of the number density of plasma ions n m^{-3}, the energy confinement time of plasma τ_{E} s, and the plasma temperature T keV. The product is called the *fusion triple product*. In order to yield the energy to sustain the plasma itself, the fusion triple product has to satisfy the condition called *self-ignition criterion* [1] and is described as:

$$n\tau_{\mathrm{E}}T > 3.1 \times 10^{21} \ \ \mathrm{m}^{-3}\mathrm{s\ keV}. \tag{1.2}$$

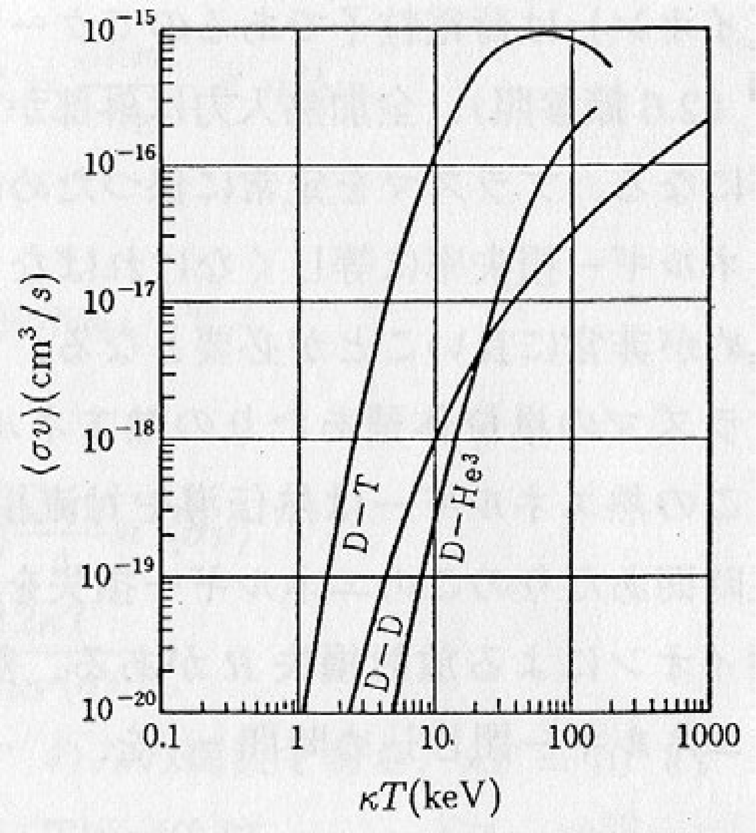

Figure 1.2: Rate coefficients of nuclear fusion reactions. (cited from Ref. [2].)

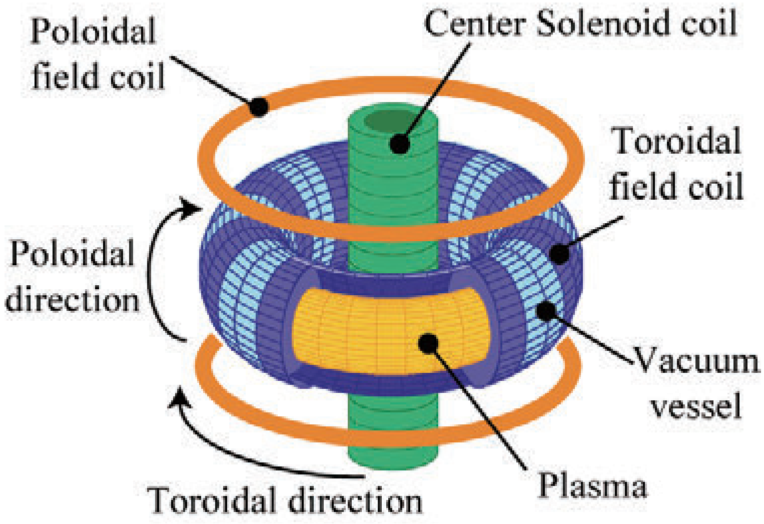

Figure 1.3: Tokamak plasma device.

1.2 Tokamak device

1.2.1 Basic concept of Tokamak device

As described in Eq. (1.2), the plasma must be kept to be denser, longer, and hotter to achieve the fusion energy. The effective method is to confine the plasma by a magnetic field. The tokamak confines a hot and dense plasma by a magnetic field. Figure 1.3 shows the schematic view of the tokamak. The plasma is confined in the torus-shaped vacuum vessel. The circumferential direction of the torus is called the toroidal direction. The cross-section of the torus is called the poloidal surface and the circumferential direction of the poloidal cross-section is called the poloidal direction. The median plane of the poloidal surface is called the midplane. The direction outward from the center of the torus along the midplane surface is called major radial direction. On the other hand, the direction outward from the center of the poloidal surface is called minor radial direction.

First, the magnetic field is induced by a toroidal coil. The magnetic field is called toroidal magnetic field $\mathrm{B_t}$. Then, the electric field in the vacuum vessel is induced along the toroidal direction by changing the current applied to the central solenoid coil. The electric field drives the plasma current along the toroidal direction. The current induces the poloidal magnetic field $\mathrm{B_p}$. The combination of $\mathrm{B_t}$ and $\mathrm{B_p}$ forms a helical-shaped magnetic field B ($\mathrm{B} = \mathrm{B_t} + \mathrm{B_p}$), shown in Fig. 1.4.

1.2.2 Tokamak device experiments and energy gain

To realize controlled fusion energy production, many tokamak experimental devices have been developed so far. Actual tokamak devices such as JT-60 U (Japan) [4, 5, 6], ASDEX Upgrade (Germany) [7] and JET (United Kingdom) [8, 9] can operate at a core plasma density $n \approx 10^{20}$

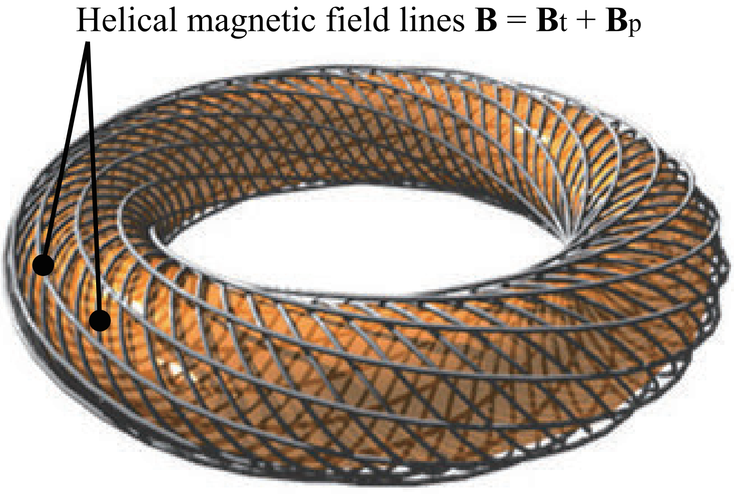

Figure 1.4: Tokamak magnetic field line in helically winding shape. (cited from Ref. [3].)

m^{-3}, a core temperature $T \approx 20\,\mathrm{keV}$, and a confinement time $\tau_{\mathrm{E}} \approx 0.1{-}1$ s. Their achievements in energy production are measured with the energy gain factor Q,

$$Q = \frac{P_{\text{Fusion}}}{P_{\text{Heating}}} = \frac{\text{Fusion energy released by D-T reaction}}{\text{Plasma heating energy required}}. \tag{1.3}$$

The energy gain factor $Q = 1$ has already been achieved by the JT-60U and JET tokamak. The international thermonuclear experimental reactor ITER [10, 11, 12] was designed and is now being constructed in France by international collaboration. The ITER is expected to operate at $Q \geq 10$ with an industrial-scale fusion power $P_{\text{Fusion}} = 500$ MW for 400-600 s in 2027. Based on the physics and engineering achievements of ITER experiments, the first real fusion power plant DEMO [13] will be constructed in the near future, in order to supply electrical energy to the society.

1.3 Impurity particles in tokamak divertor configuration

1.3.1 Problems of impurities

Due to the cross-field transport processes, such as the diffusion, the drifts, and the turbulence, a part of the fuel plasma may escape from the closed magnetic field and may reach to the plasma facing components (PFCs) of the device. The impinging of plasma ions into the PFCs causes the sputtering of the materials of the PFCs (Be, C, Fe, W, etc.). The sputtered materials are called impurities.

Once these impurity particles enter the core plasma, they prevent (or even stop) the fusion reaction by the radiation cooling and the dilution of the core plasma. Therefore, understanding

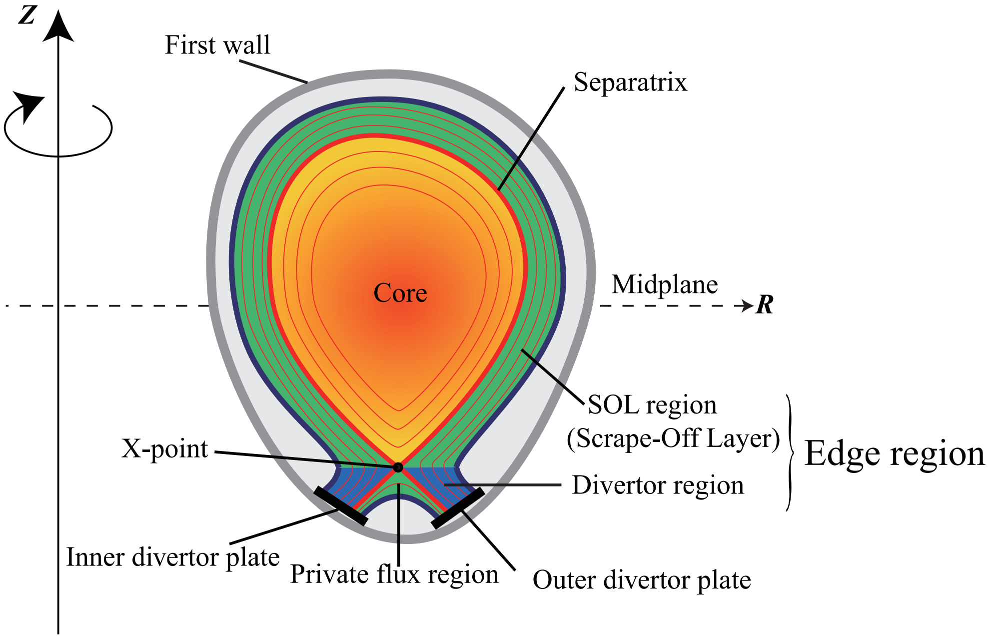

Figure 1.5: Poloidal cross section of the divertor configuration.

and controlling the impurity transport process is one of the most critical issues to achieve a sustainable fusion plasma operation.

1.3.2 Divertor magnetic configuration

One of the most feasible concept to avoid the plasma-wall interactions is the divertor magnetic configuration. Figure 1.5 shows the schematic view of the divertor configuration. Such a shape of the magnetic field shown in Fig. 1.5 can be formed by the plasma current and the equivalent current applied to the divertor coil which is placed underneath the vacuum vessel. The point where the poloidal magnetic field becomes zero is called the *null point*, or *the X-point*. The surface of the magnetic field which passes through the X-point is called the separatrix magnetic field surface, or simply, the separatrix. The closed magnetic field surface region inside the separatrix is called the core region. The peripheral region outside the separatrix is called the Scrape-Off Layer (SOL) region. The divertor plates are installed at the end of the SOL region. Therefore, in the SOL region, the open magnetic field is formed. Most of the leaked fuel plasma from the core region transported towards the divertor plates along the magnetic field line before they reach the first wall by the cross-field transport process. The region outside the separatrix, and below the X-point is called the divertor region. On the other hand, the region inside the separatrix, and below the X-point is called the private region. The region including the divertor region and the SOL region is called the edge plasma region.

The divertor configuration enables to localize plasma-wall interaction region mainly at the divertor plate. The leaked plasma has chances to lose its energy by radiation and collisions before they reach at the divertor plates.

The core plasma performance has been drastically improved owing to the divertor configuration by mitigating the impurity concentration of the core plasma. However, on the other hand, the interactions between the leaked plasma and the wall is limited to the divertor plates. Therefore, the divertor plates have to receive whole the particle/heat load from the core plasma. The concentration of the particle/heat load to the divertor plates is one of the most critical issue for realizing commercial use of the fusion power.

For example, the ITER expects its maximum thermal output from the core will be ~ 120 MW and might be recieved whole the output by the divertor plates. The areas of the outer divertor S_{outer}, and the inner divertor S_{inner} are $S_{\mathrm{outer}} \sim 6.9\mathrm{m}^2$, and $S_{\mathrm{inner}} \sim 5.4\mathrm{m}^2$, respectively. It should be noted that the output energy from the core does not equally distributed to both the inner/outer divertor plates due to the asymmetry of the tokamak plasma. Therefore, the heat load to the outer divertor plate possibly reaches $16\mathrm{MW/m}^2$ if no countermeasures were taken [14]. From the engineering point of view, the heat load to the divertor plates must be lower than $10\mathrm{MW/m}^2$ [15].

In order to achieve this objective, the ITER is plannning to reduce the heat load towards the divertor plates by operating under the *partially detachment state* (the mechanism of the detached state and the requirement to the divertor plasma will be described in Sec. 1.4.2). The detachment state prevents the divertor plate from the particle/heat load by the neutral-gas layer in front of the plate. The detachment state can be obtained by following strategies: (i) intentionally inject impurities such as nobel gases, or nitrogen molecules from the gas puff port so that the plasma energy in the SOL can be dissipated by radiation, and (ii) inclease the core density. Again, please see Sec. 1.4.2 for the further description of the detachment state.

1.4 Edge plasma characteristics

1.4.1 Flow structure of edge plasma

The impurity transport process is strongly related to the fuel plasma profiles leaked from the core. Therefore, to understand its characteristics is necessary. As shown in Fig.1.6, the plasma which leaked from the core region to the edge region transport toward the divertor. A stagnation point ($s = 0$) exists at the upstream region of the SOL. The plasma is transported from the stagnation point to the inner and outer divertor regions.

The basic characteristics of the background plasma profiles are shown in Fig. 1.7. Here, the symbol s indicates the parallel length along the magnetic field line with the stagnation point $s = 0$ m. The parallel background ion flow velocity $V_{\parallel}$, the background ion density n, and the background ion temperature T vary as Fig. 1.7. The ion flow velocity gradually increases from the stagnation point s=0 to the divertor plate s=L. The plasma becomes the neutral particle by recycling process mentioned before. The neutral particle ionizes again near the divertor plate. Therefore, the background ion density increases near the divertor plate.

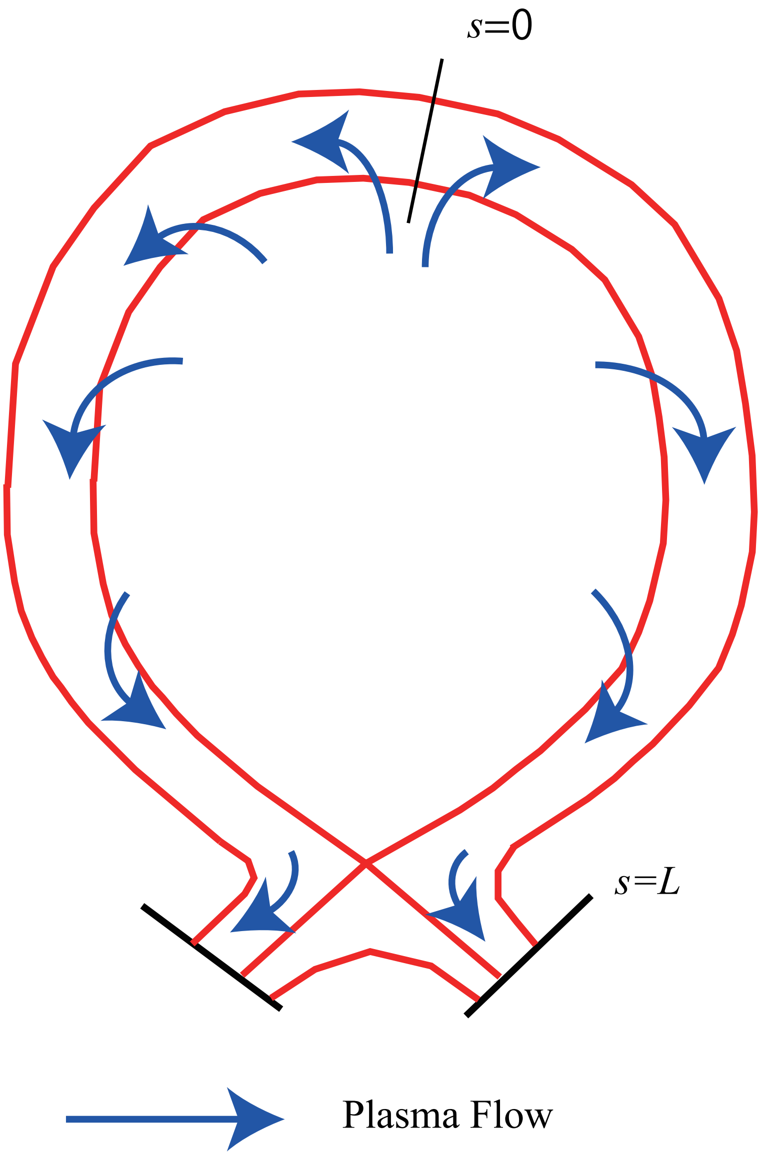

Figure 1.6: Plasma flow structure in the poloidal cross-section. The plasma leaking from the core region is transported toward the inner/outer divertor plates ($s = -L$, and $s = L$). The position $s = 0$ is called the stagnation point.

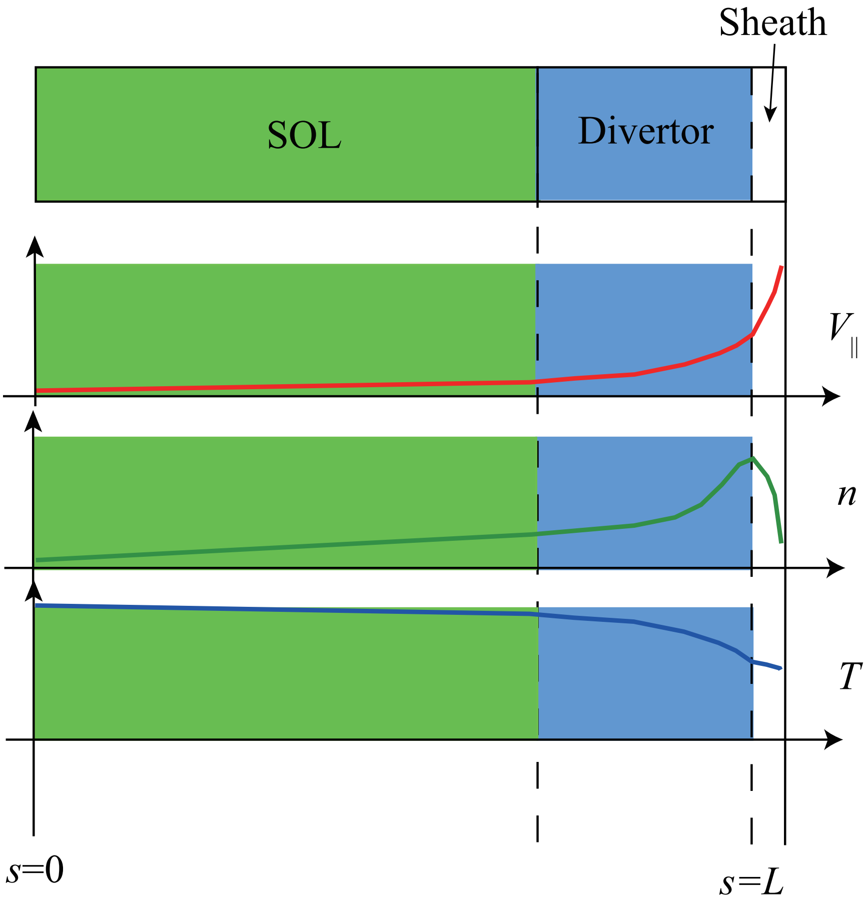

Figure 1.7: Basic characteristics of edge plasma parameters.

1.4.2 Basic characteristics of the edge plasma

As described in the previous section, a sheath potential drop exists in front of the divertor plate. The mass of a electron is extremely small compared with that of ion. Thus, electrons reach divertor plate first and they are absorbed into plate. As a result, potential drop is formed in front of the divertor plate. The sheath potential drop accelerates ions to ion sound speed c_s ($c_\mathrm{s} = \sqrt{2kT/m_\mathrm{i}}$, where the symbols m_i, and k are a mass of ion, and the Boltzmann constant, respectively) towards the divertor plate. On the other hand, electrons are decelerated due to the potential drop. This is called *Bohm criterion* [16]. A stationaly potential drop (sheath potential drop) is formed when the ion flux and the electron flux reaching divertor plates are balanced. Generally, thickness of the sheath is determined by the Larmor radius under the existence of the magnetic field.

The particle flux density Γ_d and the heat flux density q_d are given by following equations:

$$\Gamma_\mathrm{d} = n_\mathrm{d} c_\mathrm{s}, \tag{1.4}$$

$$q_\mathrm{d} = \gamma \Gamma_\mathrm{d} T_\mathrm{d}, \tag{1.5}$$

where γ is the heat transfer coefficient along the sheath. The parameters n_d and T_d are the plasma density and the plasma temperature in front of the divertor plate, respectively. The particle flux and the heat flux are related to the particle load and the heat load of the divertor plate. Therefore, according to Eq. (1.4) and Eq. (1.5), the plasma density, the flow velocity, and the temperature are related to the particle load and the heat load i.e. they are related to the impurity generation process.

Here, we will examine simple model [17] in order to understand dominant parameters affects n_d and T_d. Let us start from the following equations:

$$\frac{d}{ds}\left(m_\mathrm{i} n V_\parallel^2 + P\right) = 0, \tag{1.6}$$

$$\frac{d}{ds}\left(-\kappa_\parallel \frac{dT}{ds}\right) = 0. \tag{1.7}$$

Equation (1.6) is a momentum balance equation parallel to the magnetic field. The first term of Eq. (1.6) is a dynamic pressure of plasma ion and the second term is a static pressure $P = 2nT$. Here, the difference of temperature and density between ions and electron are neglected for simplicity i.e., they have the same value. Equation (1.7) is the heat transfer equation parallel to the magnetic field. The parallel heat conductivity $\kappa_\parallel$ is given as $\kappa_\parallel = \kappa_0 T^{2.5}$ ($\kappa_0 = const.$). The momentum loss and the energy loss are assumed to be negligible in Eq. (1.6) and Eq. (1.7). By integrating Eq. (1.6) and Eq. (1.7) from the upstream stagnation point (where $V_\parallel = 0$) to the divertor plate, we obtain

$$T_{\mathrm{u}}^{3.5} - T_{\mathrm{d}}^{3.5} = 3.5\left(q_{\mathrm{in}}L/\kappa_0\right), \tag{1.8}$$

$$n_{\mathrm{u}}T_{\mathrm{u}} = 2n_{\mathrm{d}}T_{\mathrm{d}}. \tag{1.9}$$

where n_{u} and T_{u} are the plasma density and the plasma temperature at the stagnation point, respectively. The Eq. (1.8) and Eq. (1.9) are called *two point model* since they denotes relation between the stagnation point and the point at the divertor plate. Substituting Eq. (1.8) and Eq. (1.9) into Eq. (1.4) and Eq. (1.5) leads to the relations

$$n_{\mathrm{d}} \propto n_{\mathrm{u}}^{3}q_{\mathrm{in}}^{-8/7}L^{6/7}, \tag{1.10}$$

$$T_{\mathrm{d}} \propto n_{\mathrm{u}}^{-2}q_{\mathrm{in}}^{10/7}L^{-4/7}, \tag{1.11}$$

where q_{in} is the energy flux across the SOL region from the core region (we call it the *input power* hereafter). As seen from Eq. (1.10) and Eq. (1.11), the plasma density and the plasma temperature in front of the divertor plates strongly related to the upstream density and the input power.

i) Low recycling state (attached state)

   While the core plasma density is low, the particle flux reaches the divertor plate is low. The plasma leaked from the core reaches the divertor plate directly, i.e., the plasma profile in front of the divertor plate become high temperature and low density. In this case, a low recycling state or an attached state.

ii) High recycling state

   High recycling state can be obtained by increasing the core plasma density. The particle flux reaches the divertor plate increases and recycling occurs quite often. The increase of plasma density near the divertor plate lowers the plasma temperature to 10-20 eV. As a result, the divertor plasma becomes low temperature and high density state.

iii) Detached state

   A detached state can be obtained when T_{d} becomes lower than 5 eV. In such low temperature regime, divertor plasma cannot reach divertor plates. The characteristic of detachment state is the enormous decrease of heat load and particle load to the divertor plates. Therefore, for example, the ITER will be operated with a partially detached state.

   A detached state can be divided into following three steps:

   a) Heat detachment

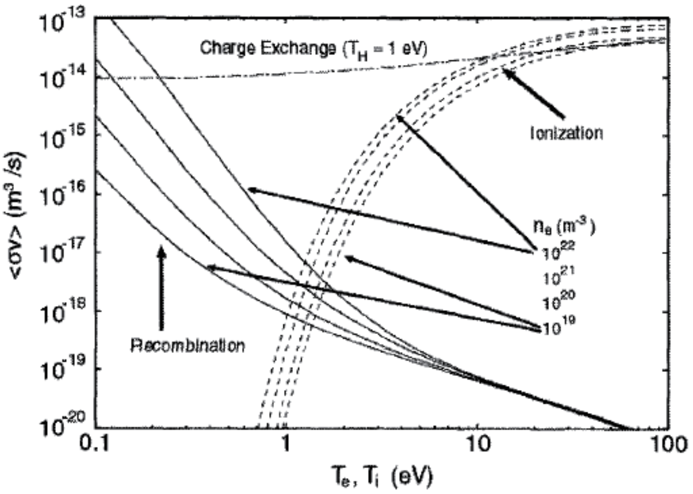

Figure 1.8: The rate coefficients of the ionization, the recombination, and the charge exchange of a hydrogen ion. (cited from Ref.[18])

Since as the intensity of recycling increases, the associated strong radiation losses also increase. As a result, the plasma temperature of divertor region decreases and the heat load to the divertor plates decreases. This is called heat detachment.

b) Pressure detachment

At very low T_d, namely, T_d <5 eV, the ionization rate coefficient rapidly decreases (Fig. 3). Therefore, the neutrals can get out from the front of the divertor plates and transport toward upstream of SOL. Since as the ionization rate coefficient decreases, charge exchange between plasma and neutral become dominant. High energy ions become neutrals and low energy neutrals become ions by charge exchange reaction. Since neutrals can move independently from the magnetic field, charge exchange reaction can spread momentum of high energy ions. Therefore, the pressure pushes divertor plates decreases. This is called pressure detachment.

c) Particle detachment

For the lowest T_d, around 1 eV, both neutral frictional drag and volume recombination may become strong, resulting the divertor region with significantly reduced plasma density, temperature and particle flux, which further reduces particle load and heat load. This condition is called a particle detachment.

At first, a detachment occurs near the separatrix due to the large ion flux. Generally, a state that the detachment occur whole place of the divertor plate is called fully detachment. However, such extremely low temperature regime could be suffer from the impurity radiation near the X-point (X-point MARFE [19, 20, 21]). In order to avoid both X-point MARFE and particle/heat load to the divertor plate, the ITER will be basically operated by partially detached state i.e. detachment only occurs near the separatrix. To increase core plasma density is not the only way to achieve detachment state. For example, neutral gas injection from the outside, or artificial impurity injection can also achieve detachment state. A detachment has been observed in several tokamak devices [22, 23, 24].

1.4.3 Application of heavy metal as divertor plate material

In an attached state, physical sputtering tends to take place since the high energy ions hit the divertor plates. Therefore, in order to avoid impurity radiation cooling of the core plasma, carbon is used for materials for the divert plates in conventional tokamak devices due to its low charge number. However, the realization of a detachment state can decrease particle/heat load to the divertor plates.

Since a detachment can decrease physical sputtering yield, the discussion of the feasibility to use a material with a high melting point such as tungsten as a divertor plate material has arose. There is no concern about chemical sputtering yield with tungsten. In addition, compared with carbon, the energy threshold of physical sputtering of tungsten is high. It is expected that the sputtering amount of impurity decreases when tungsten is used for the divertor plate material. As mentioned above, tungsten has been considered as a candidate material for divertor plates and first wall for the ITER and DEMO reactors. However, due to its high atomic number and charge number, non-negligible radiation cooling of the core plasma is expected to occur even if a very small amount of tungsten penetrates the core. The tungsten impurity density n_{W} in the core region is usually compared with electron density n_{e} in the core region. The ratio of n_{W} to n_{e} which is tolerant for continuous ITER operation is expected to be $C_{\mathrm{W}} = n_{\mathrm{W}}/n_{\mathrm{e}} \sim 10^{-5}$ [25, 26, 27]. In order to realize fusion power generation under such severe requirement, correct understanding and modeling of the tungsten transport in the SOL and the divertor region is one of the most important research subjects for designing future fusion reactors.

1.5 Impurity transport in the edge plasma

In Fig. 1.9, the schematic drawing of the impurity transport parallel to the magnetic field line is shown. Main forces acting on the impurity ion are mainly classified into two categories: 1) the friction force[28], and 2) the thermal force[29]. The impurity transport is mainly characterized by the force balance between two forces.

1.5.1 Impurity transport process parallel to the magnetic field lines

Friction force

The friction force on the impurity ions is exerted by the background ions moving with parallel flow velocity. The friction force due to background plasma flow from the core drives impurities

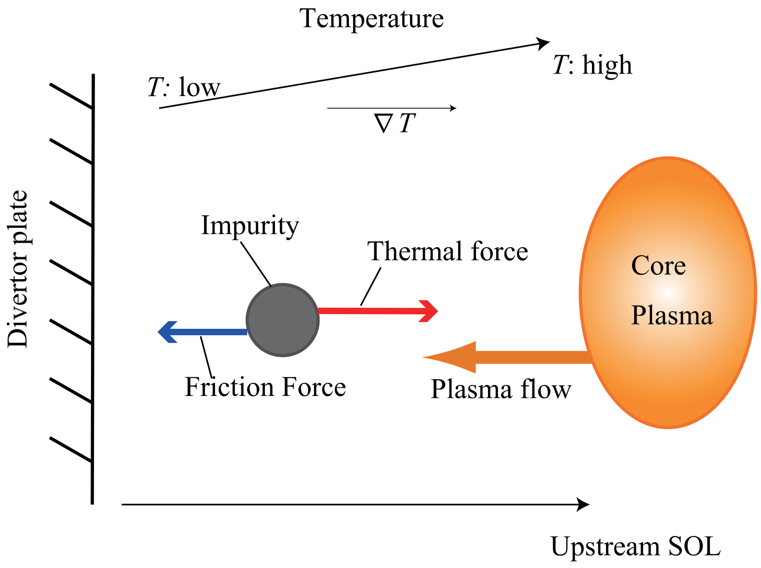

Figure 1.9: The schematic view of the parallel transport process of the impurity ion. The friction force exerted by the relative velocity between the plasma flow and the impurity velocity pushes the impurity back to the divertor plate. The thermal force exerted by the parallel temperature gradient transports the impurity ion towards the upstream of the SOL. (cited from Ref. [30])

toward the divertor plate.

Thermal force parallel to the magnetic field lines [30, 31]

The thermal force is caused by the fact that the Coulomb collision frequency ν_{b} depends on the background temperature T_{b}. When a temperature gradient exists, the coming background ions have different energy, i.e. different temperatures as shown in Fig. 1.10. The amount of momentum which is transferred to the test impurity by collisions, is roughly estimated by $m_b v_{\mathrm{th,b}} \nu_{\mathrm{b}}$. The Coulomb collision frequency ν_{b} is inversely proportional to u_{-3}, where u is the relative velocity between the colliding two particles (i.e. between the test impurity and a background ion) as $\nu_{\mathrm{b}} \propto u^{-3}$. If the impurity velocity is negligible compared with the thermal speed of the background plasma, the relative velocity u is approximated by the thermal speed of background plasma ion $v_{\mathrm{th,b}} \equiv \sqrt{kT_{\mathrm{b}}/m_{\mathrm{b}}}$ with the mass of background ion m_{b}. Therefore, the momentum transfer to the test particle is written as:

$$m_b v_{\mathrm{th,b}} \nu_b \propto v_{\mathrm{th,b}}^{-2} = T_{\mathrm{b}}^{-1}, \tag{1.12}$$

.

From Fig. 1.10 and Eq. (1.12), the background fuel plasma ions coming from a lower temperature region exert stronger force on the test particle than those coming from a higher temperature region. As a result, the net force pushes the test particle toward the hotter region. This is the parallel thermal force due to parallel temperature gradient if the plasma is magne-

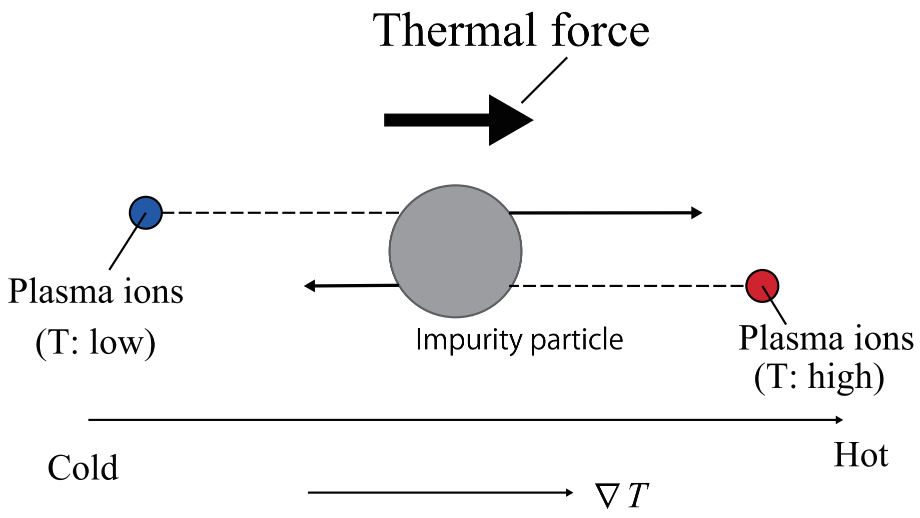

Figure 1.10: The schematic view of the thermal force parallel to the magnetic field line.

tized. In the direction along the magnetic field, the particle transport is basically determined by the balance between the parallel thermal force and the frictional force. The parallel thermal force is due to the parallel temperature gradient along the magnetic field line $\nabla_{\|} T_{\mathrm{b}}$. Figure 1.9 shows a schematic of parallel transport, with a temperature and a plasma flow profile typical in SOL region. The frictional force due to background plasma flow from the core drives impurities toward the divertor plate. On the other hand, the thermal force pushing impurities up to the core. With steep temperature gradients in the SOL, especially in a divertor region, the magnitude of the thermal force can be greater than that of the frictional force. In such condition, impurities are driven toward the core by the strong thermal force, which is unfavorable for continuous fusion device operation. Such negative effect of thermal force has to be correctly estimated.

1.5.2 Impurity transport process perpendicular to the magnetic field lines

Anomalous transport

The anomalous transport process is exerted by the local perturbation of the electric field and the magnetic field. However, it is very difficult to resolve both such a microscopic transport effects and a global transport effects in the simulation. Therefore, the present impurity transport simulation codes employs the anomalous diffusion coefficient $D^{\mathrm{AN}}{}_{\perp}$ in order to model the anomalous transport process as a simple diffusion model (the *anomalous diffusion*). The anomalous diffusion process is believed to be one of the dominant factors of cross-field transport process of impurities.

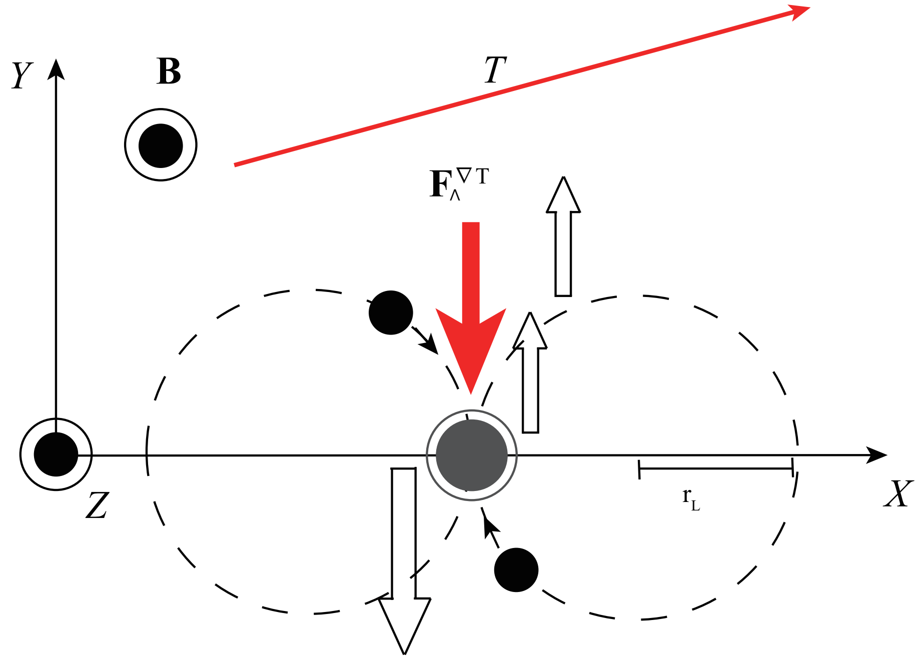

Figure 1.11: Thermal force perpendicular to the magnetic field $\mathbf{B}$. (cited from Ref. [32].)

Thermal force perpendicular to the magnetic field lines [31, 32]

Suppose a system that the perpendicular temperature gradient exists along the X-axis. Background ions, gyrating in circles with Larmor radius r_{L}, come to the test particle from different T_{b} regions. They collide with the test particle from different directions. The average speed of the background ions is estimated by the thermal speed $v_{\mathrm{th,b}}$ is supposed to be faster enough than the speed of test particle thus we can neglect the speed of the test particle itself. Since the amount of momentum transfer by collisions from a background ion to the test particle is estimated as $m_b v_{\mathrm{th,b}} \nu_{\mathrm{b}} \propto v_{\mathrm{th,b}}^{-2} = T_{\mathrm{b}}^{-1}$, the slower ions coming from the left side in Fig. 1.11 Push the test particle down more strongly than the faster ions from the right side push it up. Such unbalanced collisional momentum transfer leads to a net force on the test particle toward the Y-direction. This is the mechanism of the thermal force due to the perpendicular temperature gradient. As it is perpendicular to both the magnetic field and the temperature gradient, we call it the *diamagnetic thermal force* in this study.

In the perpendicular direction to the magnetic field (also referred to as radial direction), a steep temperature gradient is established within the SOL. It is because that the background plasma leaked from the core into the SOL escape very fast along the open magnetic field, much more quickly than the time scale for the plasma to move across the magnetic field by diffusion. As a result, a steep perpendicular temperature gradient $\nabla_{\perp} T_{\mathrm{b}}$ is formed in the SOL. Perpendicular motions of impurities across the magnetic field (abbreviated *cross-field transport*) is brought about by the diffusion due to Coulomb collisions and by the guiding center drift.

In addition to $\mathbf{E} \times \mathbf{B}$ drift and curvature drift, the diamagnetic thermal force and the magnetic field drives another drift which transports the impurity ions across the magnetic field, from the hot to cold plasma region. It is a macroscopic transport effect of thermal force called *classical temperature screening effect* (TSE) [32]. Since the TSE is expected to eject impurities from the hot core and prevent them to penetrate the core, the diamagnetic thermal force has to be correctly estimated. In addition, recently, Ref. [32] pointed out that the magnitude of TSE become non-negligible compared with the order of magnitude of the anomalous diffusion in fusion plasmas. However, the TSE has not taken into account in any previous impurity transport simulations.

Neoclassical transport

For the W transport in the SOL/divertor region, the friction force, the thermal force, the ExB drift and the anomalous radial transport are traditionally regarded as the dominant factors. In addition to these, it has recently pointed out that neoclassical transport processes, which are driven by the combination of poloidal aymmmetry of the impurity density profile, the grad-B drift, and the curvature drift, can have non-negligible effects on transport in the SOL/divertor region due to the steep temperature gradients of the background ions, particularly under H-mode and high recycling or partially detaches divertor operation conditions.

The neoclassical radial particle flux is given by the following formula:

$$\Gamma_{\mathrm{Z}}^{\mathrm{NC}} = -D_{\mathrm{Z}}^{\mathrm{NC}} \nabla_r n_{\mathrm{Z}} + n_{\mathrm{Z}} V_{\mathrm{IWP}}^{\mathrm{NC}} + n_{\mathrm{Z}} V_{\mathrm{TSE}}^{\mathrm{NC}}, \tag{1.13}$$

where the first term, the second term, and the third term are corresponding to neoclassical self-diffusion, neoclassical inward pinch (IWP), and neoclassical temperature shielding effect (TSE), respectively. The detailed descriptions of the terms appear in Eq. (1.13)are follows:

i) Neoclassical self-diffusion

   Neoclassical self-diffusion is the resultant effect of the combination of the grad-B drift, and Coulomb collisions with background ions. Consequently, the tungsten impurities have larger diffusion coefficient than that of the classical diffusion by a factor of q^2 (q: the *safety factor*).

ii) Neoclassical IWP

   Neoclassical IWP is driven by the radial background ion density gradient. The neoclassical IWP directs impurities toward a higher plasma density region across the magnetic field.

iii) Neoclassical TSE

   Neoclassical TSE is driven by the radial background ion temperature gradient. The neoclassical TSE directs impurities toward a lower temperature region across the magnetic field.

1.6 Status of tungsten impurity transport code development so far and IMPGYRO

To date, W transport processes in these regions have been kinetically studied by various SOL/divertor impurity global transport codes such as DIVIMP[33], IMPMC[34], and DORIS[35].

However, these codes were originally designed to calculate trajectories of low-Z impurity species, such as C, Ar, Ne, etc., using the guiding centre approximation, which assumes the Larmor radius to be small compared with local gradients. The characteristics of high-Z impurity species compared to low-Z impurities are: (1) larger Larmor radius due to their high mass, and (2) higher atomic number meaning that higher charge states can be reached, which has consequences for the neoclassical transport of impurities. Employing the guiding centre approximation cannot reproduce Larmor motion and its resultant effects, such as prompt re-deposition at the divertor plates, and the drifts of impurities. Therefore, dedicated high-Z impurity transport codes should be developed not only to account for these features, but also to obtain a better understanding of high-Z impurity transport.

To improve this understanding, we are continuing to develop the kinetic SOL/divertor impurity transport code IMPGYRO[36, 37, 38, 39]. The code has the following characteristics which are important for calculating W transport: (1) the exact Larmor motion of W ions is computed so that the effects of drifts are automatically taken into account; (2) Coulomb collisions between W impurities and background plasma ions are modelled using the Binary Collision Model [40] which provides a more precise kinetic numerical model of the friction and thermal forces. These characteristics are important especially for high-Z impurities like tungsten.

1.7 Purpose of Study

In order to realize the power generation by the nuclear fusion, the ITER is being constructed in France under the international collaboration project of seven parties. For the ITER and the subsequent demo reactor, tungsten (W) is considered as the most feasible material for plasma-facing components (PFCs). The performance of the fusion core plasma is influenced by the impurities coming out from the PFCs. The concentration of W impurities in the core plasma causes radiation cooling of the core plasma and the dilution of the plasma density. The ITER expects its maximum tolerance of a concentration of W 1.0×10^{-5} as a ratio between the W impurity density and the core plasma density. Therefore, it is indispensable to understand W impurity transport process in the plasma and to establish a method to control its transport. In this thesis, aiming to develop the reliable impurity transport code which can be used for designing fusion reactors, the Monte-Carlo heavy metal impurity transport code IMPGYRO has been improved and applied to the predictive W transport simulation of the ITER.

1.8 Thesis outline

The thesis is organized as follows.

In Chapter 1, the introduction of this study is given. The mechanism of tokamak fusion reactors, the influence of the core concentration of the W impurities on the core plasma performance, and transport process of the W impurity are explained.

In Chapter 2, the physical model of the multi-species plasma transport code SOLPS-ITER and the W impurity transport code IMPGYRO, which are used in this study, is explained. In Chapter 3, the W impurity transport process parallel to the magnetic field line is discussed by focusing on the effects of the thermal force and the friction force. The results show that the transport direction of the W impurities is mainly determined by the balance between the friction force and the thermal force. Under a such process, the W impurities transported towards upstream region of the edge plasma and then penetrate into the core plasma.

In Chapter 4, the detailed analysis of the W penetration process into the core discussed in Chapter 3 has been performed. The model improvement of the IMPGYRO code has been achieved by implementing the cross-field neoclassical transport model into the IMPGYRO code.

In Chapter 5, the predictive simulation of the W impurity transport in the ITER operation scenario has been performed. The W impurity transport has been compared between different typical ITER operation scenarios, (A) the high recycling state, and (B) the partially detached state in the outer divertor plate, calculated by the SOLPS-ITER code.

In Chapter 6, the achievements obtained by this study are summarized.

References in Chapter 1

[1] Egbert Boeker, Rienk van Grondelle, *Environmental Physics Sustainable Energy and Climate Change (Third Edition)*, Wiley, United Kingdom (2011).

[2] K. Miyamto, *Controlled Fusion and Plasma Physics*, Taylor & Francis Group, New York (2007).

[3] The Japan Society of Plasma Science and Nuclear Fusion Research, *Plasma Energy No Subete*, Nippon Jitsugyo Publishing, Tokyo (2007). (in Japanese)

[4] T. Fujita, Y. Kamada, S. Ishida, *et al.*, Nucl. Fusion **39** (1999) 1627.

[5] K. Tobita, the JT-60 Team, Plasma Phys. Control. Fusion **41** (1999) A333.

[6] S. Ishida, T. Fujita, H. Akasaka, *et al.*, Phys. Lev. Lett. **79** (1997) 3917.

[7] A. Herrmann, O. Gruber, Fusion Science and Technology **44** (2003) 569.

[8] J. Pamela, J. Ongena, *et al.*, Nucl. Fusion **45** (2005) S63.

[9] F. Romanelli, R. Kamendjeon, *et al.*, Nucl. Fusion **49** (2009) 104006.

[10] ITER Physics Basis Editors, *et al.*, Nucl. Fusion **39** (1999) 2137.

[11] K. Ikeda, Nucl. Fusion **50** (2010) 014002.

[12] R.J. Hawryluk, D.J. Campbell, G. Janeschitz, *et al.*, Nucl. Fusion **49** (2009) 065012.

[13] D. Maisonnier, Fusion Engineering and Design **83** (2008) 853.

[14] A.S. Kukushkin, *et al.*, Nucl. Fusion **42** (2002) 187.

[15] R.A. Pitts, *et al.*, J. Nucl. Mater. **438** (2013) S48.

[16] P. C. Stangeby, *The Plasma Boundary of Magnetic Fusion Devices*, IOP, Bristol, (2000), Chap. 2.

[17] P. C. Stangeby, *The Plasma Boundary of Magnetic Fusion Devices*, IOP, Bristol, (2000), Chap. 6.

[18] A. Hatayama， J. Plasma and Fusion Res. **77** (2001) 420.

[19] B. Lipschiltz, *et al.*, J. Nucl. Mater. **145-147** (1987) 15.

[20] N. Asakura, *et al.*, Nucl. Fusion **36** (1996) 795.

[21] H. Tamai, N. Asakura, N. Hosogome, J. Plasma Fusion Res. **74** (1998) 1336.

[22] O. Gruber, *et al.*, Phys. Rev. Lett. **74** (1995) 4217.

[23] A. Loarte, *et al.*, Nucl. Fusion **38** (1998) 331.

[24] S. Tsuji, N. Asakura, *Detachment and MARFE of divertor-plasma in JT-60* (NIFS-PROC–21). Japan (1995).

[25] A. Kallenbach, *et al.*, Plasma Phys. Control. Fusion **47** (2005) B207.

[26] R. Dux, *et al.*, J. Nucl. Mater. **390-391** (2009) 858.

[27] T. Pütterich, *et al.*, Nucl. Fusion **50** (2010) 025012.

[28] B.A. Trubnikov, *Particle Interactions in a Fully Ionized Plasma, in Reviews of Plasma Physics*, Vol. 1, Plenum, New York (1967).

[29] S.I. Braginskii, *Transport Process in a Plasma, in Reviews of Plasma Physics*, Vol. 1, Plenum, New York (1967).

[30] Y. Homma, A. Hatayama, J. Comput. Phys. **231** (2012) 3211.

[31] Yuki HOMMA, *Numerical modeling of the thermal force for impurity transport in fusion plasmas*, Keio University, Ph. D Thesis (March 2014).

[32] Y. Homma, A. Hatayama, J. Comput. Phys. **250** (2013) 206.

[33] P. C. Stangeby, C. Farrell, S. Hoskins, *et al.*, Nucl. Fusion **28** (1988) 1945.

[34] K. Shimizu, H. Kubo, T. Takizuka, *et al.*, J. Nucl. Mater. **220-222** (1995) 410.

[35] D. Reiser, D. Reiter, M. Z. Tokar, Nucl. Fusion **38** (1998) 165.

[36] A. Fukano, M. Noritake, K. Hoshino, *et al.*, J. Nucl. Mater. **363-365** (2007) 211.

[37] K. Hoshino, M. Noritake, M. Toma, *et al.*, Contrib. Plasma Phys. **48** (2008) 280.

[38] M. Toma, K. Hoshino, K. Inai, *et al.*, J. Nucl. Mater. **390-391** (2009) 207.

[39] M. Toma, X.Bonnin, Y. Sawada, *et al.*, J. Nucl. Mater. **438** (2013) S620.

[40] T. Takizuka, H. Abe, J. Comput. Phys. **25** (1977) 205.

Chapter 2

Simulation Model

2.1 Basic assumptions in tokamak geometry

Generally, a coodinate system of a tokamak magnetic configuration is expressed in the cylindrical coodinate system (R, ϕ, Z), where R is the major radius, ϕ is the toroidal, and Z is the height of the tokamak. The system is usually assumed to be an axisymmetric along ϕ ($\partial/\partial\phi$). Therefore, plasma parameters in tokamak geometries are usually discussed along the poloidal cross-section (or *R-Z plane*).

2.2 Simulation model of the SOLPS code suite

In this chapter, the physical models of the SOLPS code and the IMPGYRO code is explained. The SOLPS code is integrated code consists of the fluid plasma transport code B2.5[1, 2, 3, 4] and the kinetic neutral transport code EIRENE[5].

2.2.1 B2.5 fluid plasma transport code

The local orthogonal curvilinear coodinate system (x, y, z) used in B2.5 is shown in Fig. 2.1. The x-coodinate indicates the direction along the poloidal magnetic surfaces from the inner divertor plate to the outer divertor plate. The y-coodinate is the radial direction from the core to the SOL boundary. The symbol z indicates the direction of the toroidal field and the positive sign directs crockwise when seen from the top of the torus.

The metric coefficients are:

$$h_x = \frac{1}{|\nabla x|},\ h_y = \frac{1}{|\nabla y|},\ h_z = \frac{1}{|\nabla z|}, \tag{2.1}$$

$$\sqrt{g} = h_x h_y h_z\ . \tag{2.2}$$

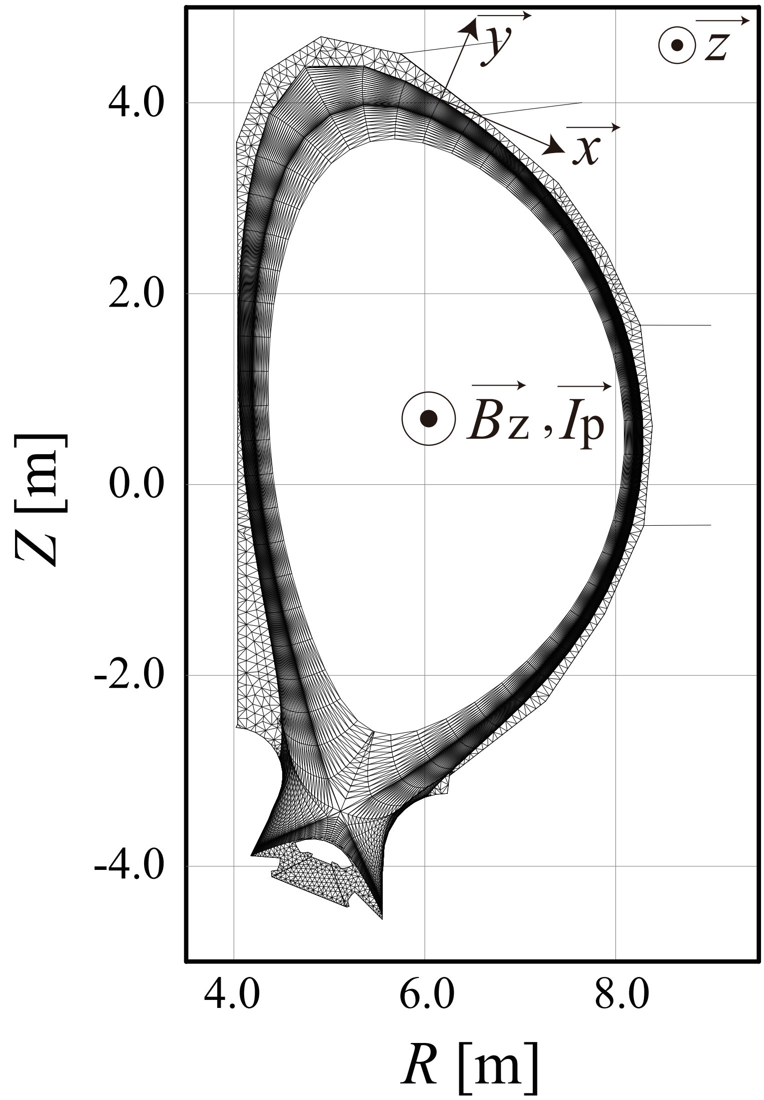

Figure 2.1: The schematic view of the coodinate system used in the B2.5.

The parameter h_z can be replaced by $h_z = 2\pi R$, where R is the local major radius. The magnetic field of the tokamak consists of toroidal magnetic field and poloidal magnetic field. Therefore, the magnetic flux density is described as $B = (B_x, 0, B_z)$. The unit vector parallel to the magnetic field line is given as:

$$\mathbf{b} = \frac{\mathbf{B}}{B} = b_x \mathbf{e}_x + b_z \mathbf{e}_z, \tag{2.3}$$

where $b_x = \frac{B_x}{B}$, and $b_z = \frac{B_z}{B}$.

The symbol $\|$ which appears hereby indicates the direction parallel to the magnetic field line. Also, $\perp$ indicates the direction of the vector product $\mathbf{B}$ and y-direction.

Prior to explain the basic equations, we will look at the velocities perpendicular to the magnetic field line. Ion velocities $V_\perp$ and V_y are determined from the momentum balance equation perpendicular to the magnetic field. Ion velocities perpendicular to the magnetic field is described as:

$$V_\perp = V_\perp^{(DF)} + V_\perp^{(E\times B)} + V_\perp^{(dia)} + V_\perp^{(in)} + V_\perp^{(vis)} + V_\perp^{(s)}, \tag{2.4}$$

$$V_y = V_y^{(DF)} + V_y^{(E\times B)} + V_y^{(dia)} + V_y^{(in)} + V_y^{(vis)} + V_y^{(s)}. \tag{2.5}$$

The first terms of the right-hand side of Eqs. (2.4) and (2.5) are the diffusive and thermo-diffusive velocities, respectively. These are described as:

$$V_\perp^{(DF)} = -\frac{D}{T_i+T_e}\frac{b_z}{h_x}\left(\frac{1}{n}\frac{\partial n}{\partial x} - \frac{3}{2}\frac{\partial T_e}{\partial x}\right) - D_{AN}^n \frac{1}{h_x n}\frac{\partial n}{\partial x} - D_{AN}^p \frac{1}{h_x n}\frac{\partial nT_i}{\partial x}, \tag{2.6}$$

$$V_y^{(DF)} = -\frac{D}{T_i+T_e}\frac{b_z}{h_y}\left(\frac{1}{n}\frac{\partial n}{\partial y} - \frac{3}{2}\frac{\partial T_e}{\partial y}\right) - D_{AN}^n \frac{1}{h_y n}\frac{\partial n}{\partial y} - D_{AN}^p \frac{1}{h_y n}\frac{\partial nT_i}{\partial y}, \tag{2.7}$$

The second terms are the $\mathbf{E}\times\mathbf{B}$ velocities and can be described as:

$$V_\perp^{(E\times B)} = -\frac{1}{B}\frac{1}{h_x}\frac{\partial \phi}{\partial x}, \tag{2.8}$$

$$V_y^{(E\times B)} = -\frac{1}{B}\frac{1}{h_y}\frac{\partial \phi}{\partial y}, \tag{2.9}$$

The third terms are the diamagnetic drift velocities and can be described as:

$$V_\perp^{(dia)} = -\frac{1}{enB}\frac{\partial nT_i}{h_y \partial y}, \tag{2.10}$$

$$V_y^{(dia)} = -\frac{B_z}{enB^2}\frac{\partial nT_i}{h_x \partial x}, \tag{2.11}$$

The terms fourth to sixth are the contributions from the inertial force, the viscosity, and the collisions with neutrals, respectively.

The B2.5 code has five unknown variables to solve: (i) the density n m^{-3}, (ii) the velocity parallel to the magnetic field line $V_\parallel$ m/s, (iii) the potential ϕ V, (iv) the ion temperature T_i eV, and (v) the electron temperature T_e eV. In order to solve these parameters, B2.5 code solves five equations: (1) the particle balance equation, (2) the parallel momentum balance equation, (3) the current continuity equation, (4) the energy balance equation for ions, and (5) the energy balance equation for electrons.

1. Particle balance equation

   The particle balance equation is described as:

$$\frac{\partial n}{\partial t} + \frac{1}{\sqrt{g}}\frac{\partial}{\partial x}\left(\frac{\sqrt{g}}{h_x} n \left(b_x V_\parallel + b_z V_\perp^{(0)}\right)\right) + \frac{1}{\sqrt{g}}\frac{\partial}{\partial y}\left(\frac{\sqrt{g}}{h_y} n V_y^{(0)}\right) = S^n, \tag{2.12}$$

Here the term S^n is the source-sink of particles per unit time, unit volume caused by ionization and recombination.

2. Parallel momentum balance equation for ions
   The parallel momentum balance equation for ions is described as:

$$\begin{aligned} & m_{\mathrm{i}}\left[\frac{\partial nV_{\|}}{\partial t}+\frac{1}{\sqrt{g}}\frac{\partial}{\partial x}\left(\frac{\sqrt{g}}{h_x}n\left(V_{\perp}^{(0)}+V_{\|}b_x\right)V_{\|}\right)+\frac{1}{\sqrt{g}}\frac{\partial}{\partial y}\left(\frac{\sqrt{g}}{h_y}nV_y^{(0)}V_{\|}\right)\right] \\ & =-\frac{b_x}{h_x}\frac{\partial nT_{\mathrm{i}}}{\partial x}-b_x\frac{en}{h_x}\frac{\partial\Phi}{\partial x}+F_k+F_{v_{\|}}+F_{q_{\|}} \\ & +\frac{1}{h_z\sqrt{g}}\frac{\partial}{\partial y}\left(\frac{h_z\sqrt{g}}{h_y^2}\eta_2\frac{\partial V_{\|}}{\partial y}\right)+\frac{1}{h_z\sqrt{g}}\frac{\partial}{\partial x}\left(\frac{h_z\sqrt{g}}{h_x^2}\eta_2\frac{\partial V_{\|}}{\partial x}\right) \\ & +b_xnm_{\mathrm{i}}V_{\|}^2\frac{1}{h_x}\frac{\partial\ln h_z}{\partial x}+S_{\mathrm{i},\|}^m+R_{\mathrm{ie},\|}, \end{aligned} \tag{2.13}$$

where m_{i} is the mass of ions. Each term in the right hand side of Eq. (2.13) corresponds to the force from the pressure gradient, the force from the electric field, the Coriolis force, the viscosity parallel to the magnetic field, the viscosity from the heat flux, the momentum variation from the collision with neutrals, and the momentum variation from the cross-interaction between ions and electrons, respectively. The pressure p is obtained from $p = n(T_{\mathrm{i}} + T_{\mathrm{e}})$.

3. Current continuity equation
   The current continuitiy equation is described as:

$$\frac{1}{\sqrt{g}}\frac{\partial}{\partial x}\left(\frac{\sqrt{g}}{h_x}\left(b_zj_{\perp}+b_xj_{\|}\right)\right)+\frac{1}{\sqrt{g}}\frac{\partial}{\partial y}\left(\frac{\sqrt{g}}{h_y}j_y\right)=0, \tag{2.14}$$

Here, $j_{\|}$ is the current parallel to the magnetic field and can be obtained from the Ohm’s law

$$j_{\|}=\sigma_{\|}\left(\frac{b_x}{e}\frac{1}{h_x}\left(\frac{\partial nT_e}{n\partial x}+0.71\frac{\partial T_e}{\partial x}\right)-\frac{b_x}{h_x}\frac{\partial\Phi}{\partial x}\right), \tag{2.15}$$

4. Energy balance equation for ions
   The energy balance equation for ions is described as:

$$\begin{aligned} & \frac{3}{2}\frac{\partial nT_i}{\partial t}+\frac{1}{\sqrt{g}}\frac{\partial}{\partial x}\left(\frac{\sqrt{g}}{h_x}\tilde{q}_{ix}\right)+\frac{1}{\sqrt{g}}\frac{\partial}{\partial y}\left(\frac{\sqrt{g}}{h_y}\tilde{q}_{iy}\right)+\frac{nT_i}{\sqrt{g}}\frac{\partial}{\partial x}\left(\frac{\sqrt{g}}{h_x}V_{\|}b_x\right) \\ & =Q_{ie}+S_i^E+nT_iB\frac{1}{h_xh_y}\left(\frac{\partial\Phi}{\partial y}\frac{\partial}{\partial x}\left(\frac{1}{B^2}\right)-\frac{\partial\Phi}{\partial x}\frac{\partial}{\partial y}\left(\frac{1}{B^2}\right)\right), \end{aligned} \tag{2.16}$$

where Q_{ie} is the energy exchange by ion-electron collision. The ion heat flux to the x-direction $\tilde{q}_{ix}$ and to the y-direction $\tilde{q}_{iy}$ is determined by the following equations:

$$\tilde{q}_{ix} = \frac{3}{2} n T_i \left(-b_z V_\perp^{(E\times B)} + b_x V_\|\right) + \frac{5}{2} n T_i \left(V_\perp^{(DF)} + \tilde{V}_\perp^{(dia)}\right) - \kappa_\| \frac{b_x^2}{h_x} \frac{\partial T_i}{\partial x} - \kappa_{i\perp} \frac{b_z^2}{h_x} \frac{\partial T_i}{\partial x}, \tag{2.17}$$

$$\tilde{q}_{iy} = \frac{3}{2} n T_{\mathrm{i}} V_y^{(E\times B)} + \frac{5}{2} n T_{\mathrm{i}} \left(V_y^{(DF)} + V_y^{(dia)}\right) - \kappa_{\mathrm{i}\perp} \frac{1}{h_y} \frac{\partial T_{\mathrm{i}}}{\partial y}, \tag{2.18}$$

where $\kappa_{\mathrm{i}\|}$ and $\kappa_{\mathrm{i}\perp}$ is the heat conductivity coefficient of ions parallel and perpendicular to the magnetic field, respectively.

5. Energy balance equation for electrons
   The energy balance equations for electrons are described as:

$$\begin{aligned} &\frac{3}{2} \frac{\partial n T_e}{\partial t} + \frac{1}{\sqrt{g}} \frac{\partial}{\partial x} \left(\frac{\sqrt{g}}{h_x} \tilde{q}_{ex}\right) + \frac{1}{\sqrt{g}} \frac{\partial}{\partial y} \left(\frac{\sqrt{g}}{h_y} \tilde{q}_{ey}\right) + \frac{n T_e}{\sqrt{g}} \frac{\partial}{\partial x} \left(\frac{\sqrt{g}}{h_x} \left(V_\| - \frac{j_\|}{en}\right) b_x\right) \\ &= -Q_{ie} + S_e^E + \frac{R_{ie} j_\|}{en} + n T_e B \frac{1}{h_x h_y} \left(\frac{\partial \Phi}{\partial y} \frac{\partial}{\partial x} \left(\frac{1}{B^2}\right) - \frac{\partial \Phi}{\partial x} \frac{\partial}{\partial y} \left(\frac{1}{B^2}\right)\right), \end{aligned} \tag{2.19}$$

Here, S_e^E is the energy exchange caused by the interactions between ions and electrons. The electron heat flux in the x-direction $\tilde{q}_{ex}$ and in the y-direction $\tilde{q}_{ey}$ is determined by:

$$\begin{aligned} \tilde{q}_{ex} &= \frac{3}{2} n T_e \left(b_z V_\perp^{(E\times B)} + b_x V_\| - b_x \frac{j_\|}{en}\right) + \frac{5}{2} n T_e \left(b_z V_\perp^{(DF)} + b_z \tilde{V}_{e\perp}^{(dia)}\right) \\ &- 0.71 b_x j_\| T_e / e - \kappa_{e\|} \frac{b_x^2}{h_x} \frac{\partial T_e}{\partial x} - \kappa_{e\perp} \frac{b_z^2}{h_x} \frac{\partial T_e}{\partial x} + \frac{3}{2} \frac{T_e}{eB} \frac{\upsilon_{ei}}{\omega_{ce}} \frac{1}{h_y} \frac{\partial n \left(T_e + T_i\right)}{\partial x}, \end{aligned} \tag{2.20}$$

$$\begin{aligned} \tilde{q}_{ey} &= \frac{3}{2} n T_e V_y^{(E\times B)} + \frac{5}{2} n T_e \left(V_\perp^{(DF)} + \tilde{V}_{ey}^{(dia)}\right) \\ &- \kappa_{e\perp} \frac{1}{h_y} \frac{\partial T_e}{\partial y} + \frac{3}{2} \frac{T_e}{eB} \frac{\upsilon_{ei}}{\omega_{ce}} \frac{1}{h_y} \frac{\partial n \left(T_e + T_i\right)}{\partial x}, \end{aligned} \tag{2.21}$$

where υ_{ei} is the ion-electron collision frequency and ω_{ce} is the cyclotron frequency of electron.

2.2.2 Boundary conditions of B2.5 code

Figure 2.2 shows the definitions of the boundaries for the B2.5 code. The boundaries are composed of the Core Interface Boundary (abbreviated to CIB), the SOL boundary, the private region boundary, and the boundaries on the inner and outer divertor plates.

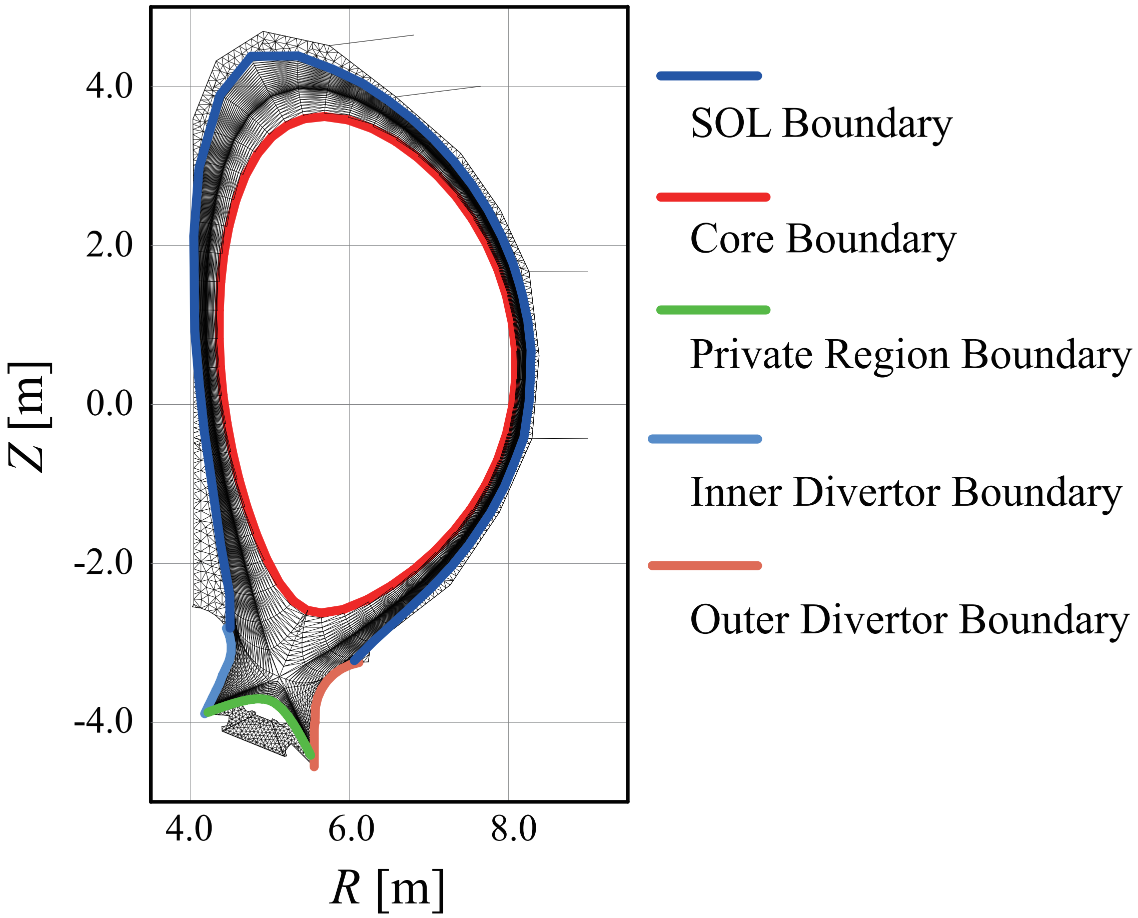

Figure 2.2: The definition of the boundaries for B2.5.

First, we explain the core side boundary conditions. In Chapter 3 and 4, the D^+ density at the core side boundary $n_{D^+}|_{\rm CIB}$, the ion and electron heat flux density at the core side boundary $q_{iy}|_{\rm CIB}$, $q_{ey}|_{\rm CIB}$ are given as the constant value. In Chapter 5, instead of keeping the D^+ density at the CIB, the particle flux densities of D^+ and He^{+2} at CIB ($\Gamma_{D^+}|_{\rm CIB}$ and $\Gamma_{He^{+2}}|_{\rm CIB}$, respectively) are specifically given as a constant parameter. These values are given specifically for the input parameters of the calculation. The boundary conditions for other ion species are given as:

$$\Gamma_y|_{\rm CIB} = 0, \tag{2.22}$$

$$V_{\|}|_{\rm CIB} = 0, \tag{2.23}$$

$$j_y|_{\rm CIB} = 0. \tag{2.24}$$

For the boundaries at the SOL and the private region, boundary conditions are given as:

$$\Gamma_y|_{\rm wall} = \alpha n c_s, \tag{2.25}$$

$$V_{\parallel}|_{\text{wall}} = 0, \tag{2.26}$$

$$\lambda_{T_{\text{i}}}|_{\text{wall}} = \text{const.}, \tag{2.27}$$

$$\lambda_{T_{\text{e}}}|_{\text{wall}} = \text{const.}, \tag{2.28}$$

$$j_y|_{\text{wall}} = 0, \tag{2.29}$$

where α is a leaking factor, $\lambda_{T_{\text{i}}}$ and $\lambda_{T_{\text{e}}}|_{\text{wall}} = \text{const.}$ are the decay length of ions and electrons, respectively. In the present study, the parameters $\alpha = 10^{-2}$, $\lambda_{T_{\text{i}}} = \lambda_{T_{\text{e}}}$ = 0.01 m are employed.

At the divertor plates, the Bohm criterion has been assumed to obtain a monotonic sheath potential drop. The boundary condition for the divertor plates is

$$V_{\parallel}|_{\text{div}} \geq c_s - \frac{b_z}{b_x} V_{\perp}|_{\text{div}}, \tag{2.30}$$

where c_s is the sound speed of ion $c_s = \sqrt{\frac{T_{\text{e}}+T_{\text{i}}}{m_{\text{i}}}}$.

The energy flux density of ions and electrons, $\tilde{q}_{ix}|_{\text{div}}$, $\tilde{q}_{ex}|_{\text{div}}$, and the current $j_x|_{\text{div}}$ flow into the divertor plates are described as:

$$\tilde{q}_{ix}|_{\text{div}} = \frac{3}{2} n T_{\text{i}} c_s b_x, \tag{2.31}$$

$$\tilde{q}_{ex}|_{\text{div}} = b_x \frac{n}{\sqrt{2\pi}} \sqrt{\frac{T_{\text{e}}}{m_{\text{e}}}} \exp\left(-\frac{e\Phi}{T_{\text{e}}}\right) (1-\gamma) \left(T_{\text{e}} \frac{1+\gamma}{1-\gamma} + e\Phi\right), \tag{2.32}$$

$$j_x|_{\text{div}} = en \left(b_x c_s - b_x \frac{1}{\sqrt{2\pi}} \sqrt{\frac{T_{\text{e}}}{m_{\text{e}}}} \exp\left(-\frac{e\Phi}{T_{\text{e}}}\right) (1-\gamma)\right), \tag{2.33}$$

where γ is the secondary electron emittion coefficient. In the present study, γ = 0.5 is assumed.

2.2.3 Transport coefficients

First, we will forcused on the diffusive plasma transport parallel to the magnetic field. The parallel particle diffusion coefficient can be described as:

$$D = \frac{T_{\text{i}} + T_{\text{e}}}{eB} \frac{\upsilon_{ie}}{\omega_{ce}}. \tag{2.34}$$

The heat conductivity is given as:

$$\kappa_{\parallel} = \kappa^0 T^{5/2}. \tag{2.35}$$

Here, κ^0 is $\kappa^0_{\text{e}} \sim 1915$ for electrons and $\kappa^0_{D+} \sim 55$ for deuterium ions. The transport process that the Coulomb collision is the dominant factor for the plasma transport is called classical transport.

The transport perpendicular to the magnetic field has different aspects. The characteristic step length of cross-field transport per collision nearly becomes the Larmor radius r_{L}. Therefore, we can write the classical perpendicular diffusion coefficient $D_{\perp}$ as

$$D_{\perp} \sim \frac{r_{\mathrm{L}}^{2}}{\tau_{\mathrm{coll.}}}. \tag{2.36}$$

The symbol $\tau_{\mathrm{coll.}}$ in Eq. (2.36) is the Coulomb collision time. In the same manner, we obtain the perpendicular heat conductivity:

$$\kappa_{\perp} \sim \frac{n r_{\mathrm{L}}^{2}}{\tau_{\mathrm{Coll.}}} = n\chi_{\perp}, \tag{2.37}$$

where $\chi_{\perp}$ is the thermal diffusivity of the plasma. However, the experimental results show larger $D_{\perp}$ and $\chi_{\perp}$ than those estimated from Eqs. (2.36), and (2.37) by the order of magnitude. To date, in order to fit the transport coefficient in with the experimental results, the *anomalous transport coefficients*, ${D^{\mathrm{AN}}}_{\perp}$ and $\chi_{\perp}^{\mathrm{AN}}$, where ${D^{\mathrm{AN}}}_{\perp}$ is the anomalous diffusion coefficient and $\chi_{\perp}^{\mathrm{AN}}$ is the anomalous thermal diffusivity, are given as input parameters in the B2.5 calculation. The parameters which agree with experimental result of the density profile and the temperature profile at the midplane and the divertor are employed as ${D^{\mathrm{AN}}}_{\perp}$ and $\chi_{\perp}^{\mathrm{AN}}$. A number of comparisons between calculation results and the experimental results has been performed so far in various tokamak devices after the designing activity of the ITER. Presently, the most of the simulations are employed the anomalous coefficients in the range of ${D^{\mathrm{AN}}}_{\perp} = 0.1 - 0.5\mathrm{m}^2/\mathrm{s}$ and $\chi_{\perp}^{\mathrm{AN}} = 1.0 - 5.0\mathrm{m}^2/\mathrm{s}$. In this study, ${D^{\mathrm{AN}}}_{\perp} = 0.3\mathrm{m}^2/\mathrm{s}$ and $\chi_{\perp}^{\mathrm{AN}} = 1.0\mathrm{m}^2/\mathrm{s}$ are employed.

2.2.4 Monte-Carlo neutral transport code, EIRENE

In this study, deuterium atom D, deuterium molecule D_2, and the carbon atom C are considered as neutral species for Chapter 3 and 4. In Chapter 5, in addition to these, except for C atoms, He, Ne atoms are considered. In order to calculate neutral transport, we use the EIRENE code. The EIRENE code directly solves the Boltzmann equation. The Boltzmann equation, which is the basic equation of the EIRENE code, is easier to understand when it is written in the integral form [6]. Boltzmann equation for a neutral specie i can be described as:

$$\begin{aligned}\Psi(\mathbf{r},\mathbf{v},i) = &\int Q(\mathbf{r}',\mathbf{v},i)\,T(\mathbf{v},i:\mathbf{r}'\rightarrow\mathbf{r})\,d\mathbf{r}' \\ &+\int\!\!\int \Psi(\mathbf{r}',\mathbf{v}',i')\,K(\mathbf{r}',\mathbf{v}',i'\rightarrow\mathbf{r},\mathbf{v},i)\,d\mathbf{r}'d\mathbf{v}'.\end{aligned} \tag{2.38}$$

Here, $\Psi(\mathbf{r},\mathbf{v},i)$ is the number of collisions occurred per unit volume in the phase space. The symbol $Q(\mathbf{r}',\mathbf{v},i)$ indicates the particle generation density at location $\mathbf{r}'$ with the velocity $\mathbf{v}$. The symbol $T(\mathbf{v},i:\mathbf{r}'\rightarrow\mathbf{r})$ is the probability that the particles can move from $\mathbf{r}'$ to $\mathbf{r}$ without any collision with the velocity $\mathbf{v}$. The symbol $K(\mathbf{r}',\mathbf{v}',i'\rightarrow\mathbf{r},\mathbf{v},i)$ is the probability of particles generated by collision at $\mathbf{r}'$ with velocity $\mathbf{v}$, moving from $\mathbf{r}'$ to $\mathbf{r}$ without any collision. Thus, the first term in the right hand side of Eq. (2.38) is the direct effect to the observing point from the point where the particles are generated. The second term indicetes the effect of collisions occurred at the other points.

To solve Boltzmann equation by Monte-Carlo method, we first need to put a test particle from the density generation distribution, and sample the collision point from $T\left(\mathbf{v}, i : \mathbf{r}' \to \mathbf{r}\right)$. Then we need to specify the collision type and the velocity after collision, and repeat this process.

The neutral production amount Q can be estimated as follows. The hydrogen neutral production is estimated with TRIM [7, 8] code. The carbon neutral production amount is estimated by physical and chemical sputtering. The physical sputtering rate is calculated from the Roth-Bodansky equation [9]. The emitting energy and the emitting angle are calculated from Thomson distribution [10] and cosine distribution, respectively. The generating process of chemical sputtering is still unclear therefore the sputtering rate and the emitting energy are given as the parameters. In the present study, the chemical sputtering rate 3% and the emitting energy $1\mathrm{eV}$ is assumed. All the carbon impurities are treated as the carbon neutral with the assumption that the hydrocarbons generated by chemical sputtering are dissociated immediately after they generated.

2.3 Simulation model of the IMPGYRO code

The IMPGYRO code is a Monte-Carlo high-Z impurity transport code. The IMPGYRO code includes most of important process of high-Z impurities: (1) the finite Larmor radius effect in a realistic tokamak geometries, (2) Coulomb collisions of impurity ions with background ions and (3) multi-step ionization/recombination process. In this section, the calculation flow and the physical model of the IMPGYRO code will be described. Figure 2.3 shows the flowchart of the IMPGYRO calculation.

The plasma parameters T_i, T_e, n_{D^+}, n_e, and $u_{\parallel,\mathrm{D}^+}$ are imported from the SOLPS calculation result. The components of the magnetic flux density vector $\mathbf{B}$ can be described as $\mathbf{B} = \mathbf{B}_\mathrm{p} + \mathbf{B}_\mathrm{t}$, where $\mathbf{B}_\mathrm{p}$ and $\mathbf{B}_\mathrm{t}$ are the poloidal magnetic field and the toroidal magnetic field, respectively. The poloidal magnetic field vector $\mathbf{B}_\mathrm{p}$ is obtained from the magnetic equilibrium data and $\mathbf{B}_\mathrm{t}$ is specified as

$$\mathbf{B}_\mathrm{t} = \frac{B_0 R_0}{R}\mathbf{b}, \tag{2.39}$$

where B_0 is magnetic flux density at the major radius R_0. The positive direction of $\mathbf{b}$ in Eq. (2.39) is clockwise direction when we see from the top of the torus.

2.3.1 Basic equation

The IMPGYRO solves equation of motion:

$$m_{\mathrm{W}}\frac{d\mathbf{v}}{dt} = q_{\mathrm{W}}\left(\mathbf{E} + \mathbf{v} \times \mathbf{B}\right) + \mathbf{F}_{\mathrm{coll}}, \tag{2.40}$$

where m_{W}, q_{W}, and $\mathbf{F}_{\mathrm{coll}}$ are the mass of tungsten, the charge of tungsten ion, and the coulomb collision term, respectively. The first term of the right hand side in Eq. (2.40) is Lorentz force and modeled by the Buneman-Boris method [11] and the second term of the right hand side, the Coulomb collision term is modeled by the Binary Collision Method (BCM) [12]. A simple diagram of the IMPGYRO calculation flow is shown in Fig. 2.3. Here, difference of the calculation flow between fluid thermal force and kinetic thermal force is emphasized with orange color in Fig. 2.3.

2.3.2 Lorentz force

The Buneman-Boris method is applied to simulate the Larmor gyro-motion of charged test particles in a magnetic field. The velocity change of test particle by the Lorentz force $\Delta\mathbf{v}^{\mathrm{GYRO}}$ is calculated. (see Ref. [11] for details.)

2.3.3 Modeling of Coulomb collision

The IMPGYRO code simulates Coulomb collision between impurity ion and background ion by BCM. The BCM simulates Coulomb collision by a randomly sampled background ion particle and an impurity test ion. The scattering angle Θ is given by

$$\Theta = 2\arctan\xi_1, \tag{2.41}$$

where ξ_1 is the random number sampled from the Gaussian distribution with the average and variance

$$\langle\xi_1\rangle = 0, \tag{2.42}$$

$$\langle\xi_1^2\rangle = \left(\frac{q_\alpha^2 q_\beta^2 n_\beta \ln\Lambda}{8\pi\varepsilon_0^2 m_r^2 u^3}\right)\Delta t, \tag{2.43}$$

where q_α, q_β, and n_β, are the charge state of the test impurity, the charge state of the background ion, and the background ion density, respectively. The constant $\ln\Lambda$, ϵ_0, and m_r are the Coulomb logarithm, the permittivity of vacuum and the reduced mass, respectively. The sybol Δt is the time step of simulation.

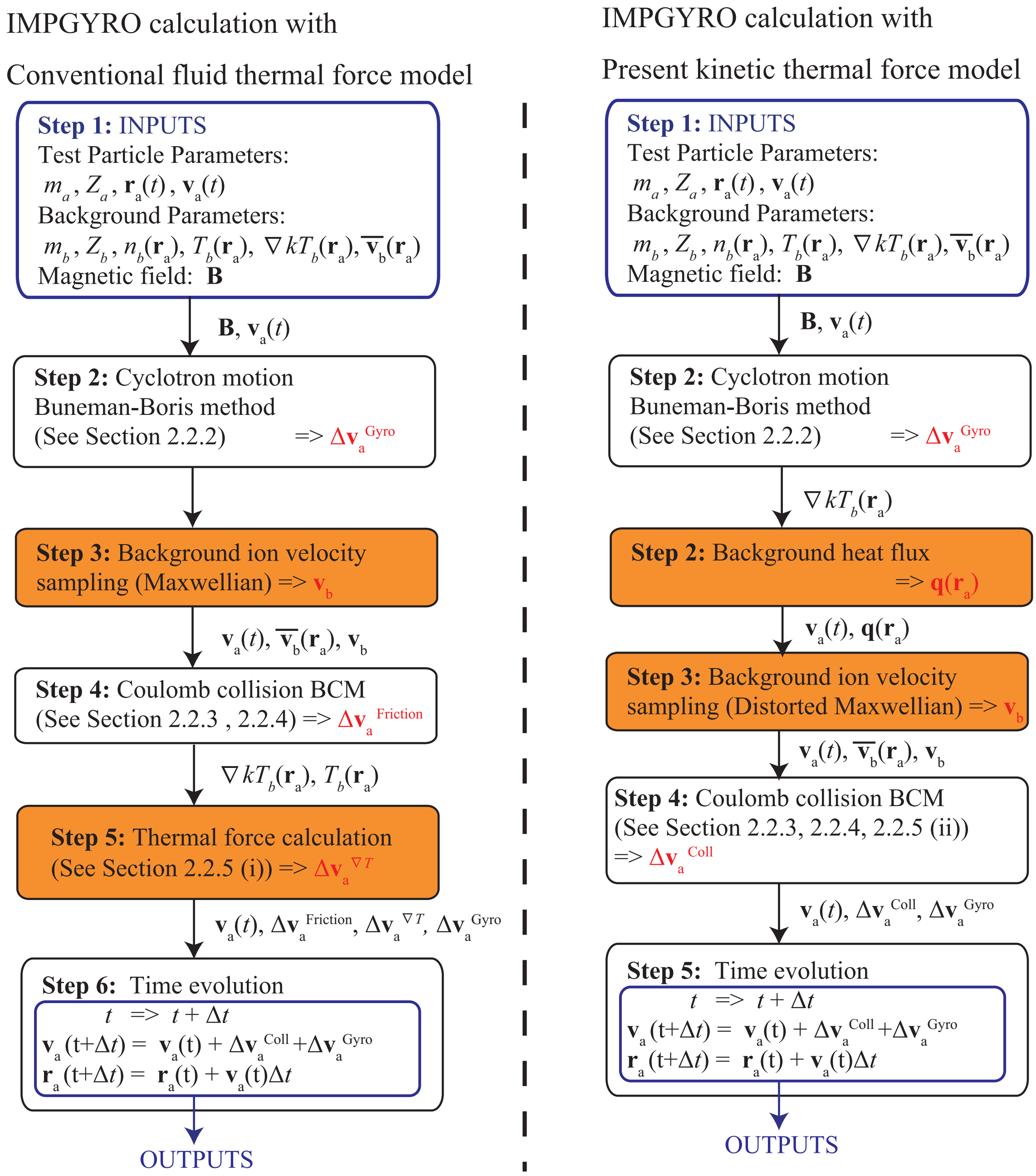

Figure 2.3: The flow of the IMPGYRO calculation

The azimuthal angle Φ is sampled with the uniform random number ξ_2:

$$\Phi = 2\pi\xi_2, \tag{2.44}$$

The variation of the relative velocity between the impurity and the background ion Δu, which is essential for modeling the Coulomb collision process, can be calculated by giving above scattering angle Θ and azimuthal angle Φ. The detail is explained as follows. The impurity velocity and the background ion velocity after collision, $\mathbf{v}'_\alpha$ and $\mathbf{v}'_\beta$, are obtained from the conservation of momentum since Coulomb collisions are elastic collisions:

$$\mathbf{v}'_\alpha = \mathbf{v}_\alpha + \frac{m_\beta}{m_\alpha + m_\beta}\Delta\mathbf{u}, \tag{2.45}$$

$$\mathbf{v}'_\beta = \mathbf{v}_\beta - \frac{m_\beta}{m_\alpha + m_\beta}\Delta\mathbf{u}, \tag{2.46}$$

where $\mathbf{v}_\alpha$, $\mathbf{v}_\beta$, m_α, and m_β are the initial impurity velocity, the initial background ion velocity, the mass of the impurity, and the mass of the background ion, respectively. If we define relative velocity before the collision $\mathbf{u}\,(= \mathbf{v}_\alpha - \mathbf{v}_\beta)$ and after the collision $\mathbf{u}' = \mathbf{v}'_\alpha - \mathbf{v}'_\beta$, $\Delta\mathbf{u}$ can be described as:

$$\Delta\mathbf{u} = \mathbf{u} - \mathbf{u}'. \tag{2.47}$$

Therefore, we can obtain $\mathbf{v}'_\alpha$ and $\mathbf{v}'_\beta$ through the calculation of $\Delta\mathbf{u}$.

The relative velocity before the collision $\mathbf{u} = (u_x, u_y, u_z)$ can be expressed with polar coordinate system (u, θ, φ) in the velocity space as shown in Fig. 2.3.3:

$$\mathbf{u} = \begin{pmatrix} u_x \\ u_y \\ u_z \end{pmatrix} = \begin{pmatrix} u\mathrm{sin}\theta\mathrm{cos}\phi \\ u\mathrm{sin}\theta\mathrm{cos}\phi \\ u\mathrm{cos}\theta \end{pmatrix}. \tag{2.48}$$

Suppose the new coordinate system (X, Y, Z) that $\mathbf{u}$ heads to Z-axis. Here, $\mathbf{u}_\perp$ is on the $X - Z$ plane. The relative velocity vector in the (X, Y, Z) system $\mathbf{U} = (U_x, U_y, U_z) = (0, 0, u)$

becomes

$$\begin{aligned}
\mathbf{U} &= \begin{pmatrix} U_x \\ U_y \\ U_z \end{pmatrix} = \begin{pmatrix} 0 \\ 0 \\ u \end{pmatrix} \\
&= \begin{pmatrix} \cos\theta & 0 & -\sin\theta \\ 0 & 1 & 0 \\ \sin\theta & 0 & \cos\theta \end{pmatrix} \begin{pmatrix} \cos\phi & \sin\phi & 0 \\ -\sin\phi & \cos\phi & 0 \\ 0 & 0 & 1 \end{pmatrix} \begin{pmatrix} u_x \\ u_y \\ u_z \end{pmatrix} \\
&= \begin{pmatrix} \cos\theta\cos\phi & \cos\theta\sin\phi & -\sin\theta \\ -\sin\phi & -\cos\theta & 0 \\ \sin\theta\cos\phi & \sin\theta\sin\phi & \cos\theta \end{pmatrix} \begin{pmatrix} u_x \\ u_y \\ u_z \end{pmatrix}.
\end{aligned} \tag{2.49}$$

Next, we calculate the variation of the relative velocity $\Delta\mathbf{U}$. If we define the scattering angle (Θ, Φ) in the (X, Y, Z) coordinate system, shown in Fig. 2.3.3, the relative velocity before the collision is $\mathbf{U} = (0, 0, u)$ and after the collision $\mathbf{U}'$ is

$$\mathbf{U}' = \begin{pmatrix} u\sin\Theta\cos\Phi \\ u\sin\Theta\sin\Phi \\ u\cos\Theta \end{pmatrix}. \tag{2.50}$$

Therefore, the variation of the relative velocity $\Delta\mathbf{U} = \mathbf{U}' - \mathbf{U}$ is obtained as

$$\begin{cases} \Delta U_x = u\sin\Theta\cos\Phi, \\ \Delta U_y = u\sin\Theta\sin\Phi, \\ \Delta U_z = u\cos\Theta - \mathrm{u} = -\mathrm{u}(1 - \cos\Theta), \end{cases} \tag{2.51}$$

The inverse matrix calculation of Eq. (2.50) gives

$$\begin{pmatrix} u_x \\ u_y \\ u_z \end{pmatrix} = \begin{pmatrix} \cos\phi\cos\theta & -\sin\phi & \cos\phi\sin\theta \\ \sin\phi\cos\theta & \cos\phi & \sin\phi\sin\theta \\ -\sin\theta & 0 & \cos\theta \end{pmatrix} \begin{pmatrix} U_x \\ U_y \\ U_z \end{pmatrix}. \tag{2.52}$$

Thus, $\Delta\mathbf{u}$ becomes

$$\begin{pmatrix} \Delta u_x \\ \Delta u_y \\ \Delta u_z \end{pmatrix} = \begin{pmatrix} \cos\phi\cos\theta & -\sin\phi & \cos\phi\sin\theta \\ \sin\phi\cos\theta & \cos\phi & \sin\phi\sin\theta \\ -\sin\theta & 0 & \cos\theta \end{pmatrix} \begin{pmatrix} \Delta U_x \\ \Delta U_y \\ \Delta U_z \end{pmatrix}. \tag{2.53}$$

Here, from Fig. 2.3.3, the relations among $u_x,\ u_y,\ u_\perp,\ \theta,\ \phi$, $\sin\theta = u_\perp/u$, $\cos\phi = u_x/u_\perp$, and $\sin\phi = u_y/u_\perp$ are derived. By substituting above equations into each component of Eq. (2.53),

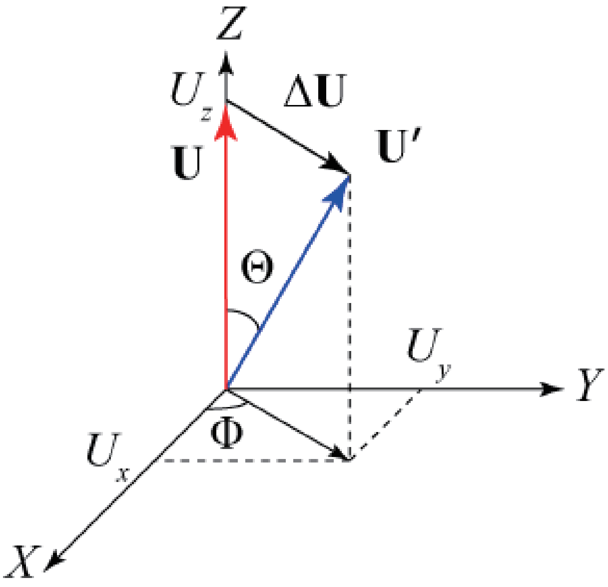

Figure 2.4: (X, Y, Z) coodinate system

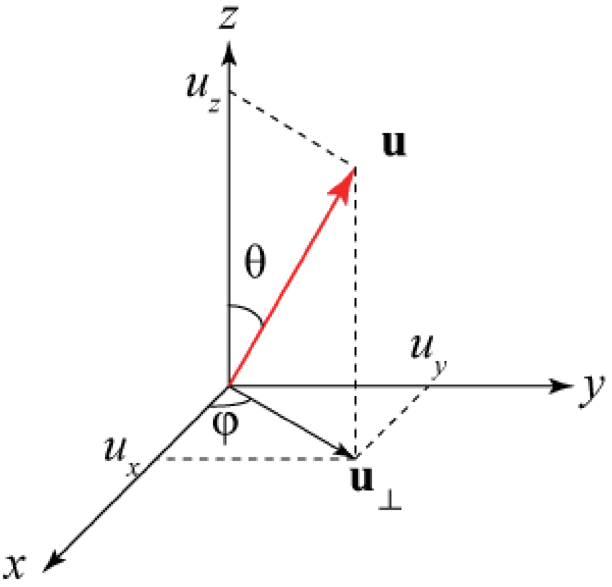

Figure 2.5: (x, y, z) coodinate system

we obtain

$$\Delta u_x = \left(\frac{u_x}{u_\perp}\right) u_z \sin\Theta\cos\Phi - \left(\frac{u_y}{u_\perp}\right) u \sin\Theta\sin\Phi - u_x\left(1-\cos\Theta\right), \tag{2.54}$$

$$\Delta u_y = \left(\frac{u_y}{u_\perp}\right) u_z \sin\Theta\cos\Phi + \left(\frac{u_x}{u_\perp}\right) u \sin\Theta\sin\Phi - u_y\left(1-\cos\Theta\right), \tag{2.55}$$

$$\Delta u_z = -u_\perp \sin\Theta\cos\Phi - u_z\left(1-\cos\Theta\right). \tag{2.56}$$

Therefore, the variation of the relative velocity can be calculated by giving scattering angle Θ and azimuthal angle Φ.

In summary, the velocity variation by Coulomb collision can be calculated by following steps:

1) Pick up a colliding particle randomly from the background plasma.

2) Calculate scattering angle Θ amd azimuthal angle Φ in accordance with Eqs. (2.41) and (2.44).

3) Calculate the relative velocity variation $\Delta\mathbf{u}$ with Eqs. (2.54), (2.55), and (2.56).

4) Substitute resulting Δu for Eqs. (2.45) and (2.46).

With this calculation, we can correctly obtain a velocity variation by Coulomb collision $\Delta\mathbf{v}_{\mathrm{coll}}$:

$$\Delta\mathbf{v}_{coll} = \frac{m_\beta}{m_\alpha + m_\beta}\Delta\mathbf{u}. \tag{2.57}$$

Here, the Step 1 is strongly related to the kinetic thermal force. In the newest version of the IMPGYRO model, a colliding particle is picked up from the *distorted Maxwellian distribution function* [13, 14]. This enables to calculate both the friction force and the thermal force together by the BCM.

2.3.4 Friction force

The friction force is exerted by the relative velocity between the background ion velocity and the impurity velocity. The background plasma ion velocity is given as:

$$\mathbf{v}_\beta = \mathbf{V}_\beta + \tilde{\mathbf{v}}_\beta \tag{2.58}$$

where $\mathbf{V}_\beta$ is the average flow velocity of the background ions, and $\tilde{\mathbf{v}}_\beta$ is the random component of the velocity due to the thermal motion. The random velocity $\tilde{\mathbf{v}}_\beta$ is sampled from the Maxwellian distribution function with the background ion temperature T_i.

The resulting friction force $\mathbf{F}^0$ is analytically obtained as:

$$\mathbf{F}^0 = -\frac{C}{4\pi}\frac{n_\beta}{2kT_\beta}\frac{\mathrm{erf}\left(\tilde{v}_\alpha\right) - \tilde{v}_\alpha \mathrm{erf}'\left(\tilde{v}_\alpha\right)}{\tilde{v}_\alpha^3} \cdot \tilde{\mathbf{v}}_\alpha. \tag{2.59}$$

The symbols appear in Eq. (2.59) are defined as follows:

$$C \equiv (\ln \Lambda)\left(\frac{q_\alpha q_\beta}{\varepsilon_0}\right)^2 \left(1 + \frac{m_\beta}{m_\alpha}\right), \tag{2.60}$$

$$\tilde{\mathbf{v}}_a \equiv \sqrt{\frac{m_b}{2kT_b}}\left(\mathbf{v}_\alpha - \bar{\mathbf{v}}_b\right), \tag{2.61}$$

$$\mathrm{erf}\left(v\right) \equiv \frac{2}{\sqrt{\pi}}\int_0^v \exp\left(-t^2\right) dt, \tag{2.62}$$

$$\mathrm{erf}'\left(v\right) \equiv \frac{d\Phi\left(v\right)}{dv} = \frac{2}{\sqrt{\pi}}\exp\left(-v^2\right). \tag{2.63}$$

2.3.5 Thermal force

In this study, the *kinetic* thermal force model [13, 14] has been implemented into the IMPGYRO. Owing to the new model, not only the effects of the friction force but also the effects of thermal force can be calculated by the BCM at the same time. The kinetic thermal force model samples the random background ion velocity $\tilde{\mathbf{v}}_\beta$ in Eq. (2.58) from the distorted Maxwellian distribution function:

$$f_\beta\left(\mathbf{v}_\beta\right) = n_\beta\left(\frac{m_\beta}{2\pi T_\beta}\right)^{\frac{3}{2}} \exp\left(-\frac{m_\beta w^2}{2T_\beta}\right) \times \left[1 - \frac{m_\beta}{n_\beta}\frac{1}{T_\beta^2}\left(1 - \frac{w^2}{5v_{th,\beta}^2}\right)\mathbf{q}\cdot\mathbf{w}\right], \tag{2.64}$$

where the random velocity of the background ion is defined as $\mathbf{w} \equiv \mathbf{v}_\alpha - \bar{\mathbf{v}}_\beta$. The symbol $\mathbf{q}$ is the heat flux density:

$$\mathbf{q} = -\kappa_\parallel \nabla_\parallel kT_\beta + \kappa_\wedge \mathbf{e}_\parallel \times \nabla_\perp kT_\beta - \kappa_\perp \nabla_\perp kT_\beta. \tag{2.65}$$

The symbols $\kappa_\parallel$, $\kappa_\wedge$, and $\kappa_\perp$ are the heat conductivities parallel to the magnetic field line, respectively.

$$\kappa_\parallel \equiv 3.9 \frac{n_\beta T_\beta \tau_\beta}{m_\beta}, \tag{2.66}$$

$$\kappa_\wedge \equiv \frac{5 n_\beta T_\beta}{2 m_\beta \Omega_\beta}, \tag{2.67}$$

$$\kappa_\perp \equiv 2 \frac{n_\beta T_\beta}{m_\beta \Omega_\beta^2 \tau_\beta}. \tag{2.68}$$

Equations (2.66), (2.67), and (2.68) respectively indicate the heat conductivities along the magnetic field line, along the diamagnetic direction of the field line, and along the radial direction of the field line.The characteristic collision time τ_β of background ions is defined by

$$\tau_\beta \equiv 12 \pi^{\frac{3}{2}} \frac{\varepsilon_0^2 \sqrt{m_\beta} T_\beta^{3/2}}{n_\beta q_\beta^4 (\ln \Lambda)}. \tag{2.69}$$

The resulting thermal force $\mathbf{F}^{\nabla T}$ is analytically obtained as:

$$\mathbf{F}^{\nabla T} = -\frac{C}{10\pi\sqrt{\pi}} \sqrt{\frac{m_\beta}{2kT_\beta}} \frac{1}{(kT_\beta)^2} \exp\left(-\tilde{v}_\alpha^2\right) \cdot \left[\mathbf{q} - 2\left(\mathbf{q} \cdot \tilde{\mathbf{v}}_\alpha\right) \tilde{\mathbf{v}}_\alpha\right]. \tag{2.70}$$

Here, the definitions of symbols C and $\tilde{\mathbf{v}}_\alpha$ are the same as those appeared in Eq. (2.59).

2.3.6 Calculation time step

In this study, we define calculation time step Δt from Larmor gyration frequency ω_c in order to calculate Larmor gyration correctly. The Larmor gyro frequency is

$$\omega_c = \frac{ZeB}{m_\mathrm{W}}. \tag{2.71}$$

In order to calculate Larmor gyration in the simulation, time step Δt should be determined as

$$\Delta t \leq \frac{1}{10} \frac{1}{\omega_c}. \tag{2.72}$$

Through the calculations performed in Chapter 3, 4, and 5, $\Delta t = 10^{-8}$ s has been employed as a time step which satisfies the criterion Eq. (2.72).

Not only the Larmor motion, but also Coulomb collisions are important for the impurity transport. A well-known time scale for Coulomb collisions is the *slowing down time* τ_s. The slowing down time τ_s is described as

$$\tau_s = \frac{1}{\left(1 + \frac{m_\alpha}{m_\beta}\right)\mu(\chi)} \frac{4\pi\varepsilon_0^2 m_\alpha^2 v_0^3}{q_\alpha^2 q_\beta^2 n_\beta \ln\Lambda}, \tag{2.73}$$

where $v_0 = |\mathbf{v}_\alpha(t=0)|$, $\chi = m_\beta v_0^2/2kT_\beta$, and $\mu(\chi) = (2/\sqrt{\pi})\int_0^\chi \exp(-\xi)\sqrt{\xi}d\xi$. The slowing down time is the time required for the particle with initial velocity $v_0 = |\mathbf{v}_\alpha(t=0)|$ decelerates to $\mathbf{v}_\alpha(\tau_s) = 0$. In order to calculate both the Coulomb collisions and the Larmor motion, the slowing down time should be considered to decide the calculation time step.

2.4 Summary of Chapter 2

In this chapter, the physical modeling of the SOLPS, and the IMPGYRO code has been explained.

The SOLPS code is the multi species plasma-neutral transport code. The SOLPS consists of the fluid plasma transport part B2.5 and the kinetic neutral transport part EIRENE. The basic equations of the B2.5 are (1) the particle balance equation, (2) the parallel momentum balance equation for ions, (3) the current continuity equation, (4) the energy balance equation for ions, and (5) the energy balance equation for electrons. By solving these equations, following plasma parameters are calculated: (i) the density n m^{-3}, (ii) the velocity parallel to the magnetic field line $V_\parallel$ m/s, (iii) the potential ϕ V, (iv) the ion temperature T_i eV, (v) the electron temperature T_e eV.

The IMPGYRO code is the Monte-Carlo particle W impurity transport code. The code has the following characteristics which are important for calculating W transport: (1) the exact Larmor motion of W ions is computed so that the effects of drifts are automatically taken into account; (2) Coulomb collisions between W impurities and background plasma ions are modelled using the Binary Collision Model which provides a precise calculation of the friction and thermal forces. The details of such characteristics are described in this chapter.

References in Chapter 2

[1] B. J. Braams, NET Rep. 68 EURFU/XII-80/87/68, CEC, Brussels (1987).

[2] R. Schneider, *et al.*, J. Nucl. Mater., **196-198** (1992) 810.

[3] V. Rozhansky, *et al.*, Nucl. Fusion **41** (2001) 387.

[4] R. Schneider, *et al.*, Contrib. Plasma Phys. **46** (2006) 3.

[5] D. Reiter, *et al.* Plasma Phys. Control. Fusion **33** (1991) 1579.

[6] A. Hatayama，J. Plasma and Fusion Res. **77** (2001) 420.

[7] W. Eckstein and D. B. Heifetz, J. Nucl. Mater. **145-147** (1987) 332.

[8] G. Bateman, PPPL Appl. Phys. Rep. No. 1, PPPL, (1980).

[9] J. Roth and C. Gracia-Rosales, Nucl. Fusion **36** (1996) 1647.

[10] M. W. Thomson, Philos. Mag. **18** (1968) 377.

[11] C. K. Birdsall, A. B. Langdon, *Plasma physics via computer simulation, Adam-Hilger*, New York (1991).

[12] T. Takizuka, H. Abe, J. Comput. Phys. **25** (1977) 205.

[13] Y. Homma, A. Hatayama, J. Comput. Phys. **231** (2012) 3211.

[14] Y. Homma, A. Hatayama, J. Comput. Phys. **250** (2013) 206.

Chapter 3

Effects of Background Plasma Characteristics on Tungsten Impurity Transport in the SOL/Divertor Region using IMPGYRO Code [1]

In this chapter, the difference of tungsten impurity transport characteristics between a high recycling regime and a partially detached regime has been studied by IMPGYRO code. The background plasma profiles of the JT-60U model tokamak geometry calculated from SOLPS have been used. To obtain such characteristic regimes, we have changed input power of electron Q_e and ion Q_i at the core boundary. In the high-recycling regime, the tungsten impurities have been transported upstream of the SOL. On the other hand, in the partially detached regime, most tungsten impurities have been localized in the both inner and outer target plates. These features are mainly related to the background plasma temperature and ion flow.

3.1 Calculation settings and model improvement

3.1.1 Geometrical model and basic plasma parameters

To obtain background plasma profiles, SOLPS[2] has been used. Figure 3.1 shows the numerical grid corresponding to the plasma equilibrium considered. The vacuum vessel, the baffle plate, the dome structure, the inner and outer divertor plates are also shown in Fig. 3.1. The red line in Fig. 3.1 will be used later in Sec. 3.2 to analyze simulation data. The circle pointed by an arrow in Fig. 3.1 indicates the tungsten source point. This numerical grid is produced from a JT-60U tungsten experiment configuration [3] (shot #49540). The toroidal magnetic field B_0 value at the geometrical center of plasma is 3.6 T. The plasma current I_p is 1.6 MA.

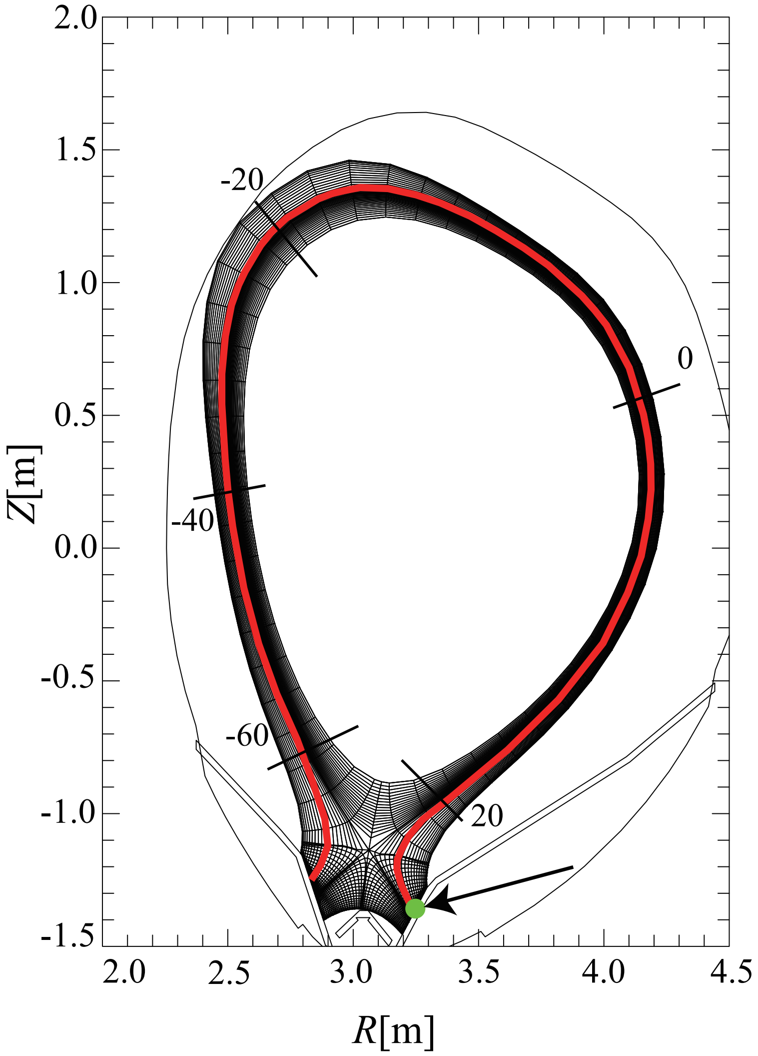

Figure 3.1: SOLPS numerical mesh for whole computational domain. The distance along the magnetic field line s, from the light green starting point s=29.48, is measured along the red line. (cited from Ref. [1])

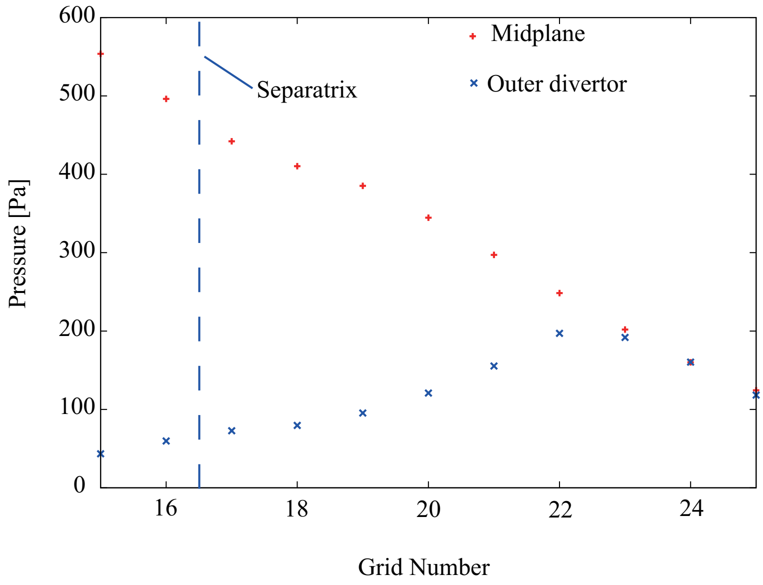

Figure 3.2: Radial profile of the total pressure at the midplane and the outer divertor for Case B (partially detached state). The broken line shows the location of the separatrix. In the region near the separatrix, total pressure apparently does not conserve between the midplane and the outer divertor.

3.1.2 SOLPS5.0 calculation setups

The following two cases have been calculated by the SOLPS code, to obtain characteristic regimes of divertor plasma i.e. a high recycling state and a partially detached state. To obtain such characteristic regimes of divertor plasma, we have changed input power at the core side boundary which are independent of specific experiments:

Case A : $Q_{\mathrm{e}} = Q_{\mathrm{i}}$ = 5.0 MW, (High-recycling state),

Case B : $Q_{\mathrm{e}} = Q_{\mathrm{i}}$ = 1.5 MW, (Partially detached state),

where Q_{e} and Q_{i} are the electron and ion input power supplied, respectively, at the core side boundary.

As will be shown later, Case A (see Fig. 3.4(a), (b)) is in a high-recycling state, while Case B (see Fig. 3.9(a), (b)) is in a partially detached state. For Case B, the electron temperature becomes less than 5 eV in front of the outer divertor near the separatrix. Also, we have carefully checked the total pressure balance between the midplane and the outer divertor plate (Fig. 3.2). The region near the separatrix, the total pressure does not conserve between the midplane and the outer divertor. This proves that Case B is in a partially detached state at least from the viewpoint of the momentum detachment.

Except for the heating powers, all other parameters are the same in both cases. The deuterium ion density at the core side boundary is kept constant $n_{\mathrm{D}^+} = 3.0 \times 10^{19} \mathrm{m}{-3}$ throughout the SOLPS calculation. The radial transport coefficients are given as $D = 0.3\mathrm{m}^2/\mathrm{s}$, $\chi_{\mathrm{e}} = \chi_{\mathrm{i}} =$

$1.0\mathrm{m}^2/\mathrm{s}$ in both cases, where D is the anomalous diffusion coefficient, while χ_e and χ_i are the thermal diffusivity of electrons and ions, respectively. These values of coefficients are similar to the previous simulations such as Ref. [4, 5].

3.1.3 IMPGYRO calculation setups

Tungsten impurity transport has been calculated by Monte-Carlo test particle modeling with the IMPGYRO [6] code. The trace impurity limit has been assumed. Therefore, the background plasma profiles are fixed and not affected by the impurities for each case above.

The tungsten impurities are launched from the outer divertor plate 1.4 cm outside from the separatrix, with the constant generation rate of 10^{18} /s. This initial position corresponds to the place where the tungsten tiles have been installed in the JT-60U tungsten experiments [3]. It should be noted that the impurity density shown later in Fig. 3.3 and Fig. 3.7 depends on the impurity generation rate (10^{18}/s) and it has uncertainty. Therefore the absolute values of impurity density don't have significant meaning. Only the relative value has significance.

Here, we simply assumed an initial monotonic energy distribution function of 10 eV for the injected impurities. In the future the parametric survey of initial energy and/or more realistic model to determine the initial energy will be needed. As for the angular distribution, a cosine distribution has been assumed. All the test impurity particles which reach the boundary (core, wall, divertor plates, baffle plate, dome structure, etc. in Fig. 3.1) are assumed to be absorbed. The self-sputtering of tungsten has been neglected throughout this study. In the IMPGYRO code, Coulomb collisions are modeled by the Monte-Carlo binary collision method. Therefore, classical and neoclassical self-diffusion processes are included. The anomalous diffusion of impurity ions has been neglected. In addition, the kinetic modeling of the thermal force along the field line proposed in Ref. [7] has been implemented into the IMPGYRO code, while fluid modeling of the thermal force was used in previous studies [8, 9].

3.2 Results and Discussion

Figure 3.3 shows the 2D profile of tungsten ions summing over all charge states, in Case A (high recycling state case). After being released from the outer divertor plate, the tungsten impurities are transported towards the upstream and localized around the top region of the SOL. Finally, they penetrate into the core region by grad-B drift.

To understand this behavior in Case A, the background profiles of ion temperature $T_\mathrm{i}(s)$ and parallel flow velocity $u_\parallel(s)$ along the red line in Fig. 3.1 are shown respectively in Fig. 3.4(a) and (b). The symbol s denotes the distance from the point $s = 0$ in Fig. 3.1 along the field line, near the outboard midplane.

In this high recycling state (Case A), tungsten neutrals are ionized immediately after they are launched at the target plate, because of sufficiently high electron temperature T_e in front

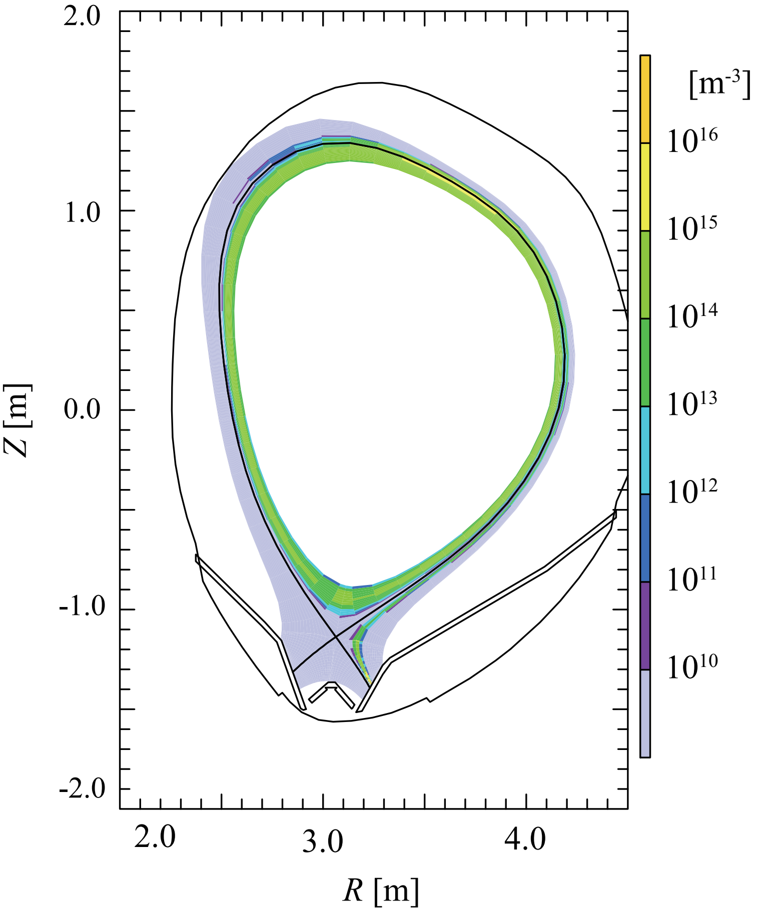

Figure 3.3: 2D profile of tungsten impurity density in Case A in poloidal cross section. The densities for all the charge states are summed up. (cited from Ref. [1])

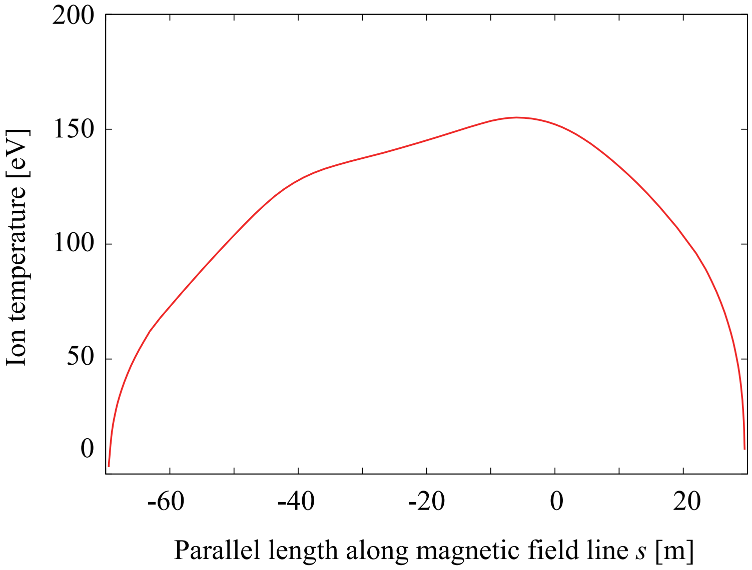

(a)

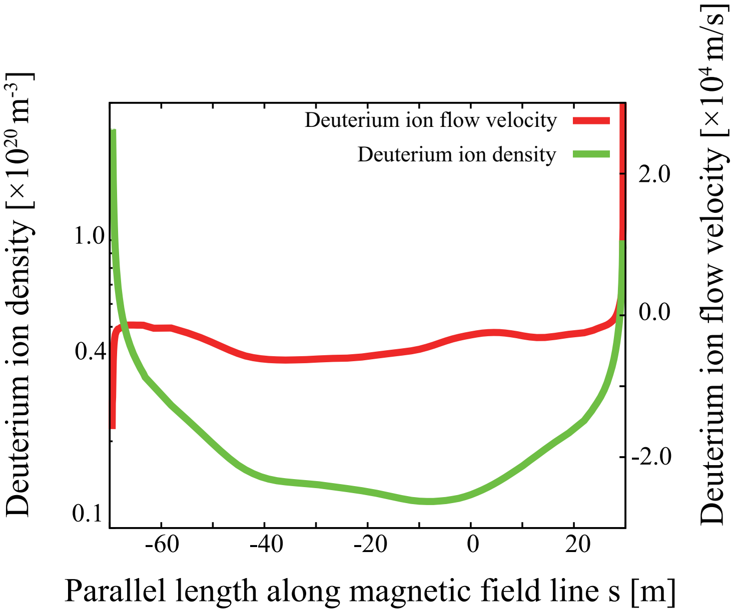

(b)

Figure 3.4: Profiles of background plasma parameters in Case A along magnetic field line : (a) Ion temperature, (b) Ion flow velocity. (cited from Ref. [1])

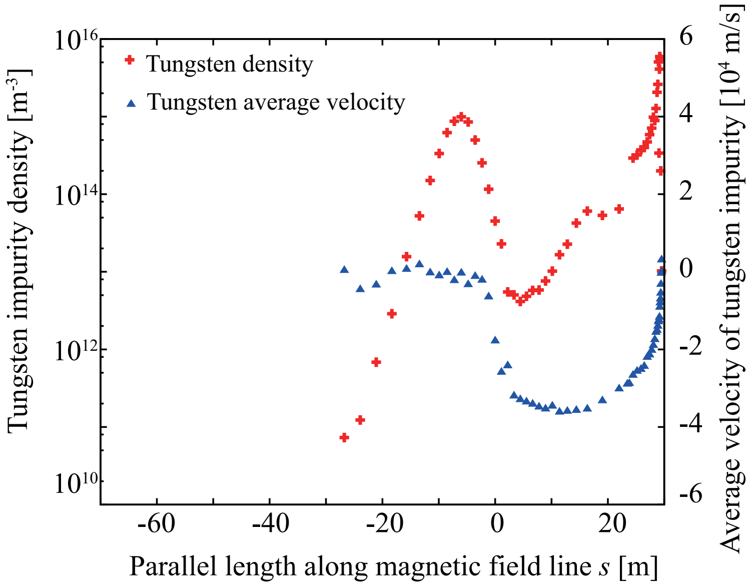

Figure 3.5: Density and average velocity of tungsten impurity plotted along magnetic field line. The positive value means that the velocity is in the direction towards the outer divertor plate, while the negative values towards the inner divertor. (cited from Ref. [1])

of the target plate ($T_e \approx 18\mathrm{eV}$). Then, the tungsten ions are transported upstream toward the SOL top region by the thermal force. In this case, the thermal force pushes the tungsten ions toward the upstream, more strongly than the friction force pushes them toward the outer divertor plates. This is understood from the following observations: (1)A large ion temperature gradient $\partial T_{\mathrm{i}}/\partial s(\approx 10\mathrm{eV/m})$ exists near the target plate in Fig. 3.4 (a), leading to a strong parallel thermal force component. (2) The background plasma flow velocity $u_{\parallel}$ is large only very near the divertors. The drag effect by the friction force is thus weakened. The spatial profile of the tungsten average parallel velocity $u_{\parallel}^{\mathrm{W}}(s)$ and the density $n_{\mathrm{W}}(s)$ along the field line are plotted in Fig. 3.5. As seen from Fig. 3.5, at first $u_{\parallel}^{\mathrm{W}}(s)$ rapidly increases in the region ($s \approx 25-30$) near the outer target plate, where the negative sign of $u_{\parallel}^{\mathrm{W}}(s)$ indicates the direction towards the inner target plate, while the positive sign is the direction towards the outer divertor. As explained above, this is because tungsten ions are accelerated by the thermal force due to the large temperature gradient near the divertor plate in Fig. 3.4 (a).

As shown in the impurity velocity profile in Fig. 3.5, however, the acceleration is getting smaller as the traveled distance from the outer divertor plate increases (around $s < 20$), because the temperature gradient is getting smaller. In the region $s > 20$, $\left|u_{\parallel}^{\mathrm{W}}\right|$ becomes almost constant, and then $\left|u_{\parallel}^{\mathrm{W}}\right|$ decreases rapidly. Finally, $\left|u_{\parallel}^{\mathrm{W}}\right|$ becomes almost zero in the region $s \leq 0$. This behavior of impurity parallel flow velocity $u_{\parallel}^{\mathrm{W}}(s)$ along the field line is also mainly explained by the temperature profile in Fig. 3.4 (a) and the resulting thermal force. The background temperature T_{i} has a peak near the half way point of the SOL ($s \approx 0$) and the temperature gradient ∇T_{i} changes the sign. Due to this change of the directions, the flow reversal of the test

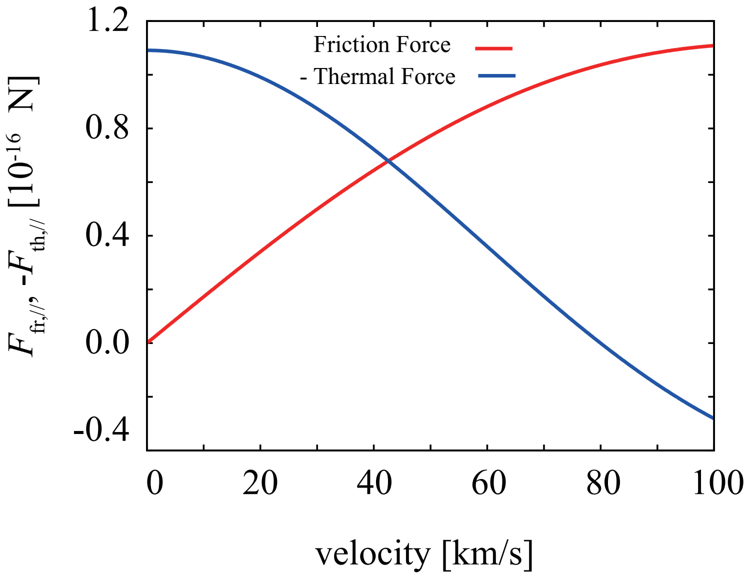

Figure 3.6: The analytical value of the friction force and the thermal force with negative [-] sign (using equations (3.1) and (3.2)) as a function of tungsten impurity velocity. The background parameters at s=15 are employed.

impurity ions takes place and the average impurity velocity $\left|u_{\parallel}^{\mathrm{W}}\right|$ rapidly decreases. Because of these processes, the residence time of the impurity ions increases in the region $s \leq 0$ and the impurity density $n_{\mathrm{W}}(s)$ becomes larger in this low flow-velocity region as shown in Fig. 3.5. This long residence time makes it possible for the impurities to penetrate the core by the grad-B drift. The detailed machanism of the core penetration will be discussed in Chapter 4.

If there is no temperature gradient in the system, i.e. the thermal force does not exist, only the friction force act on the impurity particles. In such case, the impurity velocity will be relaxed to the background ion velocity. However, if temperature gradient exists in the system, the friction force should be balanced with the thermal force. Thereby, the relative velocity between impurity ions and background ions should exist. In the present calculation, relatively large temperature gradient exists. Therefore the thermal force is very strong. In order to balance such a strong thermal force, it is necessary for the relative velocity between impurity ions and background ions to become large. This explains why the impurity velocity is one order higher than the background ion velocity.

More quantitatively, the friction force and the thermal force has been calculated as a function of impurity velocity; shown in Fig. 3.6. We have estimated the value of the forces as a function of parallel impurity velocity by using the following well-known equations for the friction force $F_{\parallel,\mathrm{fr}}$ and the thermal force $F_{\parallel,\mathrm{th}}$ [10, 11]:

$$F_{\parallel,\mathrm{fr}} = -\frac{(\ln\Lambda)}{4\pi} Z_{\mathrm{W}}^2 \left(\frac{e^2}{\varepsilon_0}\right)^2 \left(1+\frac{m_{\mathrm{b}}}{m_{\mathrm{a}}}\right) \frac{n_{\mathrm{b}}}{2kT_{\mathrm{b}}} \frac{\Phi(\tilde{v}_{\parallel,\mathrm{W}}) - \tilde{v}_{\parallel,\mathrm{W}}\Phi'(\tilde{v}_{\parallel,\mathrm{W}})}{\tilde{v}^3_{\parallel,\mathrm{W}}} \tilde{v}_{\parallel,\mathrm{W}}, \tag{3.1}$$

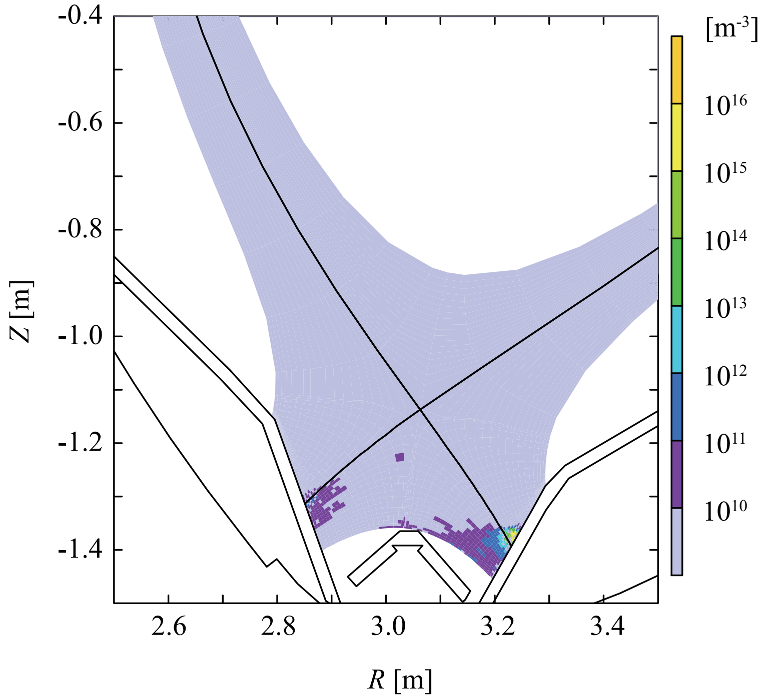

Figure 3.7: A zoom-in view of the 2D profile of tungsten impurity density in Case B in poloidal cross section. The densities for all the charge states are summed up. (cited from Ref. [1])

$$F_{\|,\mathrm{th}} = \frac{15\sqrt{2}}{8}\left(1+\frac{m_\mathrm{b}}{m_\mathrm{a}}\right) Z_\mathrm{W}^2 \exp\left(-\tilde{v}_{\|,\mathrm{W}}^2\right)\cdot\left[\nabla_\| kT_\mathrm{b} - 2\left(\nabla_\| kT_\mathrm{b}\cdot\tilde{v}_{\|,\mathrm{W}}\right)\tilde{v}_{\|,\mathrm{W}}\right], \tag{3.2}$$

$$\tilde{v}_{\|,\mathrm{W}} = \sqrt{\frac{m_b}{2kT_b}}\left(v_{\|,\mathrm{W}} - \bar{u}_{\|,\mathrm{b}}\right), \tag{3.3}$$

with background ion density n_b=1.65×10^{19} m^{-3}, ion temperature and its gradient T_b=133.5 eV, ∇T_b=-2.54 eV/m, tungsten charge state Z_W=10, and the relative velocity is assumed to be the impurity velocity because the background velocity is negligible compared with the impurity velocity. These parameters are from the calculation results at s = 15 m (see Fig. 3.4 (a) and (b)). The expressions and meanings of other symbols are the same as those in Ref. [7]

As shown in Fig. 3.6, the impurity velocity is around 40 km/s when the friction force and the thermal force are balanced. This result proves why the acceleration of averaged tungsten impurity velocity reaches 40 km/s in Case A.

Considering from these results discussed above, acceleration of tungsten impurity velocity up to 40 km/s is a reasonable result.

Figure 3.7 shows the 2D profiles of the impurity density in Case B (partially detached state), summed over all charge states, while Fig. 3.8 shows the 2D background electron temperature profile near the divertor region. As seen in Fig. 3.7, tungsten impurities are mainly localized close to the outer target plate, while some have reached the inner target plate. These characteristic features are explained in the following manner.

Figure 3.9 (a) and (b) show the background plasma profiles in Case B along the red line in Fig. 3.1. Compared with that in Case A, the ion temperature is relatively low in Case B.

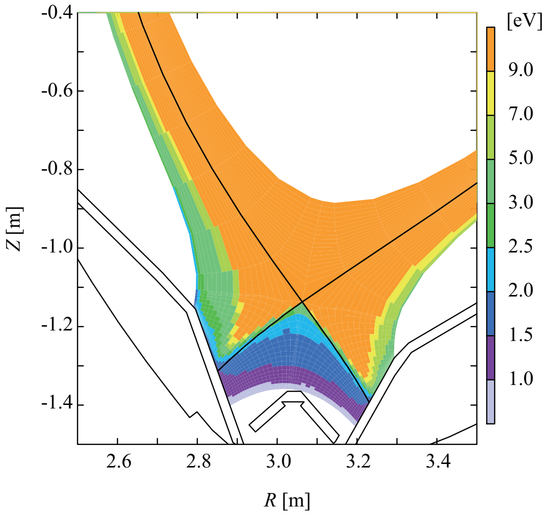

Figure 3.8: 2D profile of the background electron temperature in Case B. (cited from Ref. [1])

In addition, the ion temperature gradient parallel to the magnetic field line $\partial T_{\mathrm{i}}/\partial s (\approx 4\mathrm{eV/m})$ is less steep than that in Case A. Therefore, the thermal force becomes weaker in Case B. Furthermore, as seen from the comparison between Fig. 3.9 (b) and Fig. 3.4 (b), the background ion flow is higher and more broadened in Case B. Therefore, the friction force becomes larger than the thermal force. As a result, tungsten impurities cannot move towards the upstream in the SOL in Case B. As shown in Fig. 3.8, the electron temperature T_{e} and also the density ne in the private region, especially near the dome structure is very low. Therefore, the mean free path of tungsten neutrals λ_{mean} becomes very large, e.g. $\lambda_{\mathrm{mean}} \approx$ 3.3 m with typical T_{e} and ne near the dome structure ($T_{\mathrm{e}} \approx$ 1 eV, $n_{\mathrm{e}} \approx 10^{19}$ m^{-3}, $\langle\sigma v\rangle \approx 10^{-16}\mathrm{m}^3/\mathrm{s}$). This length is large enough for tungsten neutrals to cross over into the inner divertor region. However, due to the increase in the electron density and temperature, λ_{mean} becomes about 0.03 m in the region close to the inner target plate with $T_{\mathrm{e}} \approx$ 2 eV, $n_{\mathrm{e}} \approx 3 \times 10^{19}$ m^{-3}, $\langle\sigma v\rangle \approx 3 \times 10^{-15}\mathrm{m}^3/\mathrm{s}$. It is a reason why the ionized impurities are seen near the inner target plate in Fig. 3.7.

3.3 Summary of Chapter 3

In this study, we have investigated effects of background plasma characteristics on the transport process of tungsten impurities. Trajectories of test tungsten impurity particles have been kinetically simulated by the IMPGYRO code, under two different background plasma profiles corresponding, respectively, to the high-recycling regime and the partially detached regime. All the impurity particles have been launched from the outer divertor plate. In order to focus on the collisional transport process, simple models have been assumed for the impurity production and wall interaction. The anomalous impurity transport and the effect of the background electric field have also been neglected.

In the high-recycling regime where a steep parallel temperature gradient exists, the tungsten

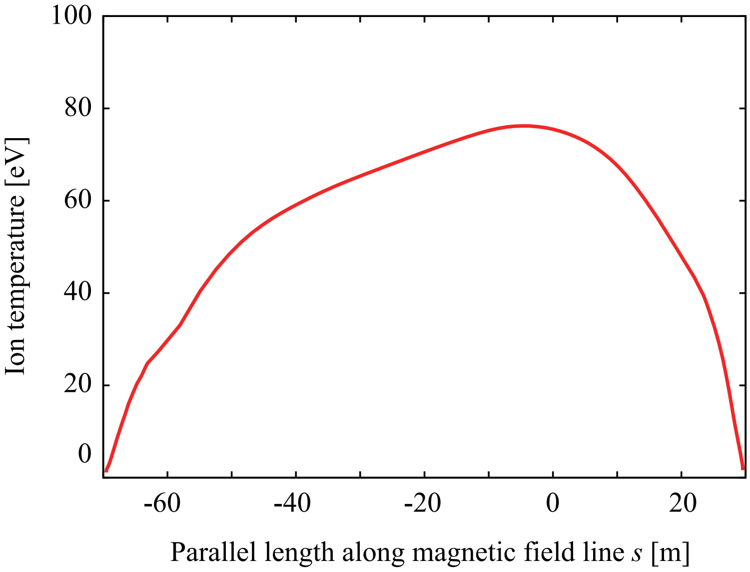

(a)

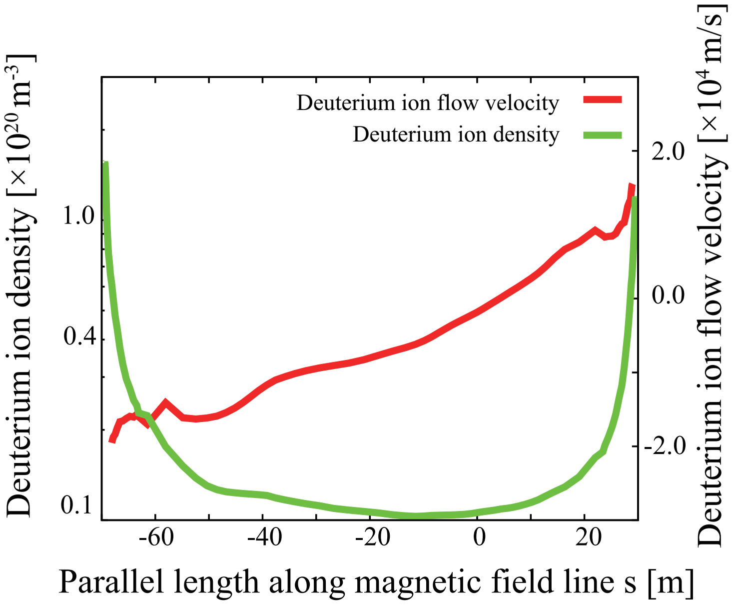

(b)

Figure 3.9: Profiles of background plasma parameters in Case B along magnetic field line : (a) Ion temperature, (b) Ion flow velocity. (cited from Ref. [1])

impurities are transported upstream, i.e. to the top region of the SOL, mainly by the thermal force which is larger than the friction force.

In the partially detached regime, most tungsten impurities have stayed in the vicinity of the outer divertor plate. The friction force is dominant in this regime because the parallel temperature gradient is much less steep. Some impurities could reach the inner divertor region by crossing the private region, because of the lower temperature and density profiles of the background plasma.

We have confirmed that the background plasma profiles have strong influences on the impurity transport process. The balance between the friction force and the thermal force along the magnetic field line plays a key role.

As a next important step, the effects of more complete impurity-wall interactions such as the prompt re-deposition and tungsten self-sputtering [12] will be investigated. In addition, as pointed out in Refs. [13] and [14], inward pinch and temperature screening effect due to perpendicular background ion density gradient and thermal force are also important in the SOL region.

References in Chapter 3

[1] S. Yamoto, *et al.*, J. Nucl. Mater. **463** (2015) 615.

[2] R. Schneider, *et al.*, Contrib. Plasma Phys. **46** (2006) 3.

[3] Y. Ueda, *et al.*, Nucl. Fusion **49** (2009) 065027.

[4] A. Hatayama, *et al.*, Nucl. Fusion **40** (2000) 2009.

[5] K. Shimizu, *et al.*, Nucl. Fusion **49** (2009) 065028.

[6] A. Fukano, *et al.*, J. Nucl. Mater. **363-365** (2007) 211.

[7] Y. Homma, A. Hatayama, J. Comput. Phys. **231** (2012) 3211.

[8] M. Toma, *et al.*, J. Nucl. Mater. **438** (2013) S620.

[9] S. Yamoto, *et al.*, Contrib. Plasma Phys. **54** (2014) 421.

[10] B.A. Trubnikov, *Particle interactions in a fully ionized plasma, in: M.A. Leontovich (Ed.), Reviews of Plasma Physics*, vol. 1, Consultants Bureau, New York (1965).

[11] S.I. Braginskii, *Transport processes in a plasma, in: M.A. Leontovich (Ed.), Reviews of Plasma Physics*, vol. 1, Consultants Bureau, New York (1965).

[12] D. Coster et al., In: 21st Intl. Conf. on Plasma Surface Interactions P3-059, 2014. (Kanazawa, Japan)

[13] Y. Sawada, *et al.*, Trans. Fusion Sci. Technol. **63** (1T) (2012) 352.

[14] Y. Homma, A. Hatayama, J. Comput. Phys. **250** (2013) 206.

Chapter 4

Effects of classical and neo-classical cross-field transport of tungsten impurity in realistic tokamak geometry [1]

In this chapter, for further discussion, we mainly focus on the transport process perpendicular to the magnetic field in order to obtain general understandings of core penetration process of impurities in realistic tokamak geometry by the IMPGYRO code [2, 3]. The cross-field transport process in the SOL is still unclear and it is assumed that impurity transport processes perpendicular to the magnetic field in the SOL are governed by the anomalous diffusion in kinetic impurity transport codes [4, 5]. Recently, it has been pointed out that neoclassical transport possibly becomes large in the SOL/divertor plasma where the perpendicular gradient of density and temperature are relatively steep [6, 7, 8]. However, these effects have not been considered in any SOL/Divertor kinetic impurity transport code with guiding center approximation.

The neoclassical radial particle flux is given by the following formula [9, 10]:

$$\Gamma_Z^{\mathrm{NC}} = -D_Z^{\mathrm{NC}} \nabla_r n_Z + n_Z V_{\mathrm{pinch}}^{\mathrm{NC}} + n_Z V_{\mathrm{TSE}}^{\mathrm{NC}}, \tag{4.1}$$

where the first term, the second term and the third term in Eq. (4.1) are corresponding to the neoclassical self-diffusion, the neoclassical inward pinch, and the neoclassical temperature screening effect, respectively. The neoclassical self-diffusion is the resultant effect of the combination of a magnetic drift and Coulomb collisions with background ions which leads tungsten impurities to have larger diffusion coefficient than the classical diffusion by a factor of q^2 (q: the safety factor) [11]. Since the Larmor motion (i.e. drifts) and collisions are already included in the IMPGYRO model [12], neoclassical diffusion has been already implemented into the

IMPGYRO code. However, the present modeling of the IMPGYRO can calculate only the neoclassical diffusion and not all neoclassical transport processes. For example, in order to take into account other neoclassical transport processes such as neoclassical inward pinch and temperature screening effect, the effect of the Pfirsch-Schlüter flow and the the Pfirsch-Schlüter heat flux [11] must be implemented in the parallel transport process of the impurities.

In this chapter, as the first step toward implementing whole the neoclassical effect into the IMPGYRO model, the effect of the neoclassical self-diffusion process of the impurity particles in realistic tolamak geometry has been investigated. In order to understand the effects of neoclassical self-diffusion and its magnitude, comparison between the full-gyro orbit motion model by IMPGYRO [2, 3, 13] and the guiding center approximation model has been performed under the background plasma parameter obtained from numerical code-package SOLPS5.0 [14].

4.1 Calculation settings

4.1.1 Geometrical model and basic plasma parameters

To obtain background plasma profiles, SOLPS5.0 [14] has been used. Figure 4.1 shows the numerical grid corresponding to the plasma equilibrium considered. The vacuum vessel, the baffle plate, the dome structure, the inner and outer divertor plates are also shown in Fig. 4.1. This numerical grid is produced from a JT-60U tungsten experiment configuration [15] (shot #49540). The toroidal magnetic field B_0 value at the geometrical center of plasma is 3.6 T. The plasma current I_p is 1.6 MA.

4.1.2 SOLPS calculation setups

Since our goal is to obtain general understandings of core penetration process of impurities, the following SOLPS calculation parameters are decided independent of specific experiments. The deuterium density n_{D^+} at the core side boundary is given as $n_{\mathrm{D}^+} = 3.0 \times 10^{19}\mathrm{m}^{-3}$. The input power at the core side boundary is $Q_{\mathrm{e}} = Q_{\mathrm{i}} = 5.0\mathrm{MW}$ where Q_{e} and Q_{i} are the electron and ion input power supplied, respectively.

Radial transport coefficients are given as $D_\perp = 0.3\mathrm{m}^2/\mathrm{s}$, $\chi_{\mathrm{e}} = \chi_{\mathrm{i}} = 1.0\mathrm{m}^2/\mathrm{s}$, where $D_\perp$ is the anomalous diffusion coefficient for the background plasma, while χ_{e} and χ_{i} are thermal diffusivity of electrons and ions, respectively. These values of coefficients are typical parameters in SOL/divertor simulation and similar values can be seen in Refs. [16, 17]

4.1.3 IMPGYRO calculation setups

Physics model implemented in the IMPGYRO code in the present study is the same as those in Ref. [3]. Effects of magnetic drifts have been automatically taken into account, because

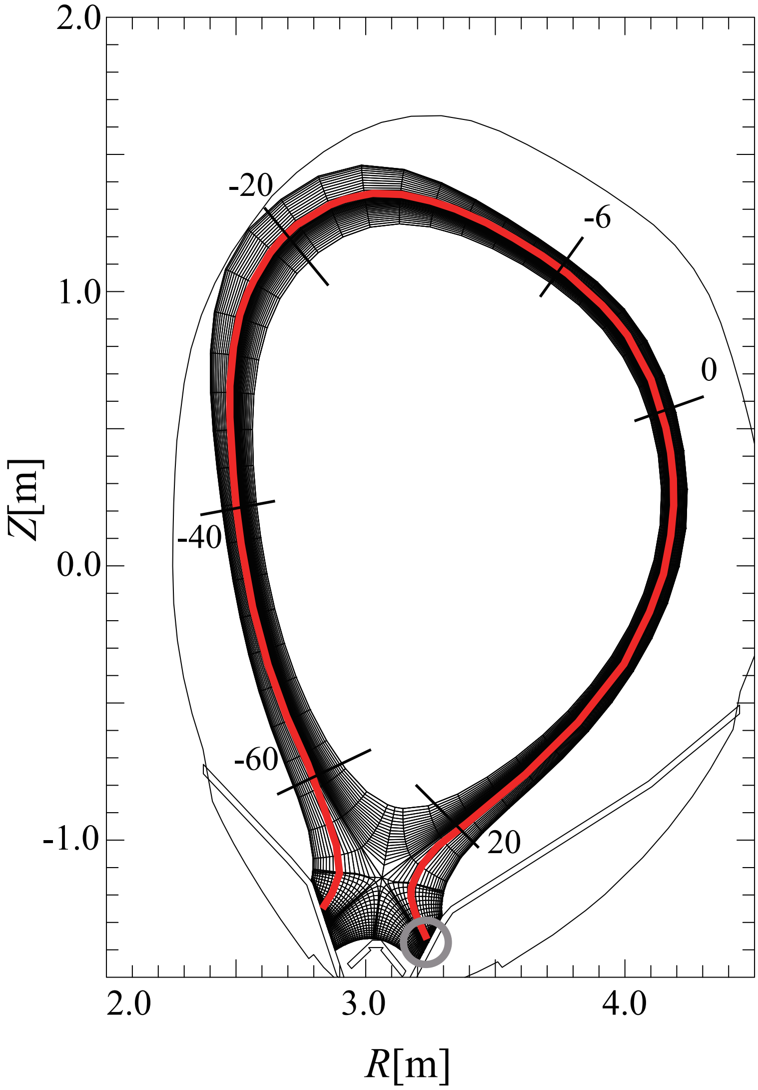

Figure 4.1: SOLPS numerical mesh for whole computational domain. The red line corresponds to the distance along the magnetic field line s, from the circled starting point s =29.48 m. (cited from Ref. [1])

the full orbit of each test particle has been followed in IMPGYRO code. As a result, not only classical, but also neoclassical self-diffusion of impurity ions is also automatically included in the simulation [12] with the Binary Collision Model [18]. Separately, we have made numerical program of impurity transport with guiding center approximation. The equation of motion for the guiding center parallel to the magnetic field has been solved, while the same model has been used such as Coulomb collision, multi-step ionization/recombination. In this study, the same Monte Carlo model of anomalous diffusion has been employed both in the IMPGYRO code and the program with guiding center approximation. In the Monte Carlo model, each random walk step by the anomalous diffusion perpendicular to magnetic surface is given by: $\Delta r = \sqrt{2D_{\mathrm{an}}\Delta t}\xi$ [4, 5] , where Δt and ξ are the time step and a normal random number sampled from a Gaussian distribution with the mean and variance being zero and one, respectively. In addition, D_{an} is anomalous diffusion coefficient ($D_{\mathrm{an}} = 0.3$ m ^{2}/s has been used throughout this study).

Tungsten impurities are launched from the outer divertor plate 1.4 cm outside from the separatrix. The location where the tungsten tiles have been installed in the JT-60U tungsten experiments [15] has been considered as the initial position of tungsten impurities.

As for the initial velocity, an initial monotonic energy distribution function of 10 eV with a cosine angular distribution for the injected impurities are assumed. All the test impurity particles which reach the boundary (core, wall, divertor plates, baffle plate, dome structure, etc.) are assumed to be absorbed.

4.2 Results and discussion

Figure 4.2 shows the tungsten impurity density profiles. In both cases, the tungsten impurities are localized around the top region of the SOL. This behavior can be explained by the balance between the friction force and the thermal force [3].

In this study, we will focus on the impurity penetration process into the core. Figure 4.3 shows the radial profiles of the averaged perpendicular velocity of the tungsten impurities at s =-6.0 m where the tungsten impurities are localized both in Case A (the full-orbit model with the IMPGYRO code) and Case B (the guiding center model), respectively. The positive sign of the velocity denotes the direction from the separatrix towards the wall. The horizontal axis denotes the distance from the separatrix $r = 0$ m and the positive sign region ($r > 0$m) represents the SOL region. In the full-orbit model (Case A), the perpendicular tungsten velocity has directed toward the core in the region $r < 0.015$ m. In the region $r > 0.015$ m, on the other hand, the velocity has directed outward of the SOL. The absolute value of the radial average velocities of impurities with the IMGYRO are larger than those with the guiding center approximation (Case B). To understand this behavior, we have plotted the radial profiles of the tungsten impurity density both in Case A and Case B (Fig. 4.4). If the diffusion process is assumed to be dominant,

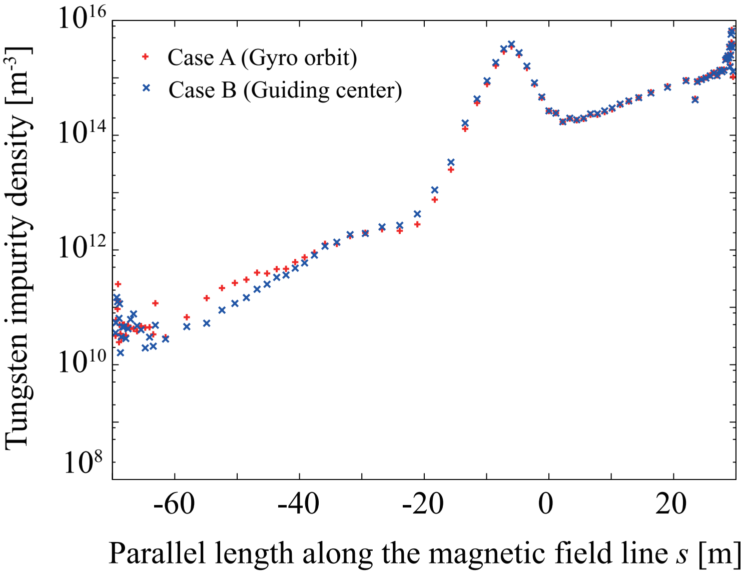

Figure 4.2: Tungsten density plotted along the magnetic field line. The horizontal axis s m corresponds to the red line in Fig. 4.1. (cited from Ref. [1])

the radial particle flux of impurity ions may be written as

$$n_Z V_r = -D\nabla_r n_Z, \tag{4.2}$$

where n_Z, V_r and D are the impurity density, the perpendicular impurity average velocity, and the diffusion coefficient, respectively.

In Case B, we only take into account the anomalous diffusion. From the calculated radial velocity shown in Fig. 4.3 and the density profile in Fig. 4.4, we can estimate the diffusion coefficient. For example, $V_r \approx 5.5$ m/s in Fig. 4.3 at $r = 2.3 \times 10^{-2}$ m, while $n_Z \approx 2.4 \times 10^{15}$ m^{-3} and $|\nabla_r n_Z| \approx 7.3 \times 10^{16}$ m^{-4} at the same position from Fig. 4.4. From these values, the diffusion coefficient becomes roughly $D \approx 0.2$ m^2/s. This value is roughly the same order as the specified value of the anomalous diffusion coefficient $D_{an} = 0.3$ m^2/s in the simulation.

In the same way as above, we can roughly estimate the diffusion coefficient in CaseA, namely, the results for the IMGYRO code with full orbit calculation. At the same position ($r = 2.3{\times}10^{-2}$ m), $V_r \approx 18$ m/s in Fig. 4.3, $n_Z \approx 2.2{\times}10^{15}$ m^{-3} and $|\nabla_r n_Z| \approx 6.8{\times}10^{16}$m^{-4} in Fig. 4.4. From these values, the diffusion coefficient in Case A becomes roughly $D \approx 0.6$ m^2/s. The diffusion coefficients in Case A have a trend to be larger than those in Case B. As we described in Sec. 4.1.3, in Case A with IMPGYRO calculation, full orbit has been followed. As a result, the effects of magnetic drifts and the resultant neoclassical self-diffusion process have been included in the calculation. In Ref. [12], it has been pointed out that the neoclassical self-diffusion coefficient possibly becomes the same order of magnitude as the anomalous diffusion coefficient used in the present study in the SOL/divertor plasma where

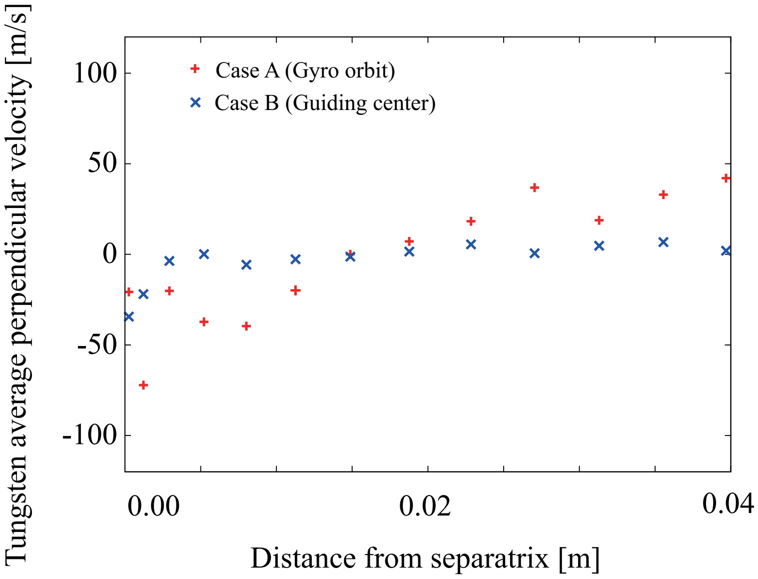

Figure 4.3: The radial profile of the averaged perpendicular velocity of the tungsten impurities at s =-6.0 m. The positive sign of the velocity denotes the direction from the core to the SOL. The horizontal axis denotes the distance from the separatrix $r = 0$ m and the region $r > 0$ m corresponds to the SOL region. (cited from Ref. [1])

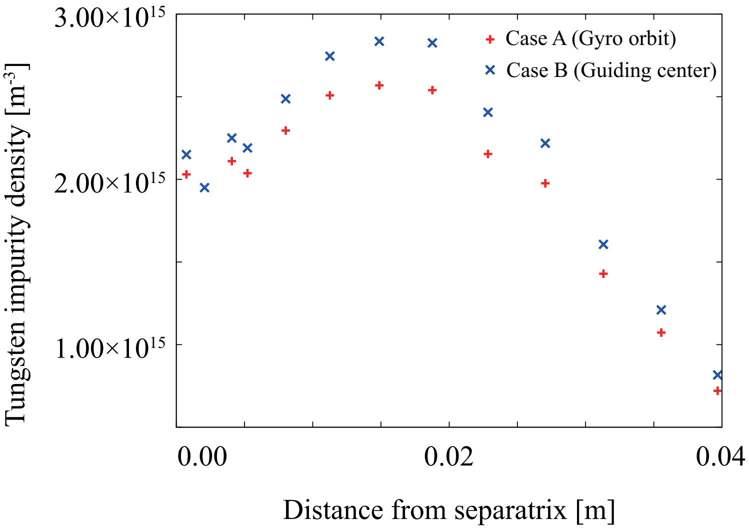

Figure 4.4: The radial profile of the tungsten impurity density. (cited from Ref. [1])

the ion temperature is much smaller than that in the core plasma region and the collisionality becomes larger. The neoclassical self-diffusion coefficient is estimated from the the following formula [11], $D_{\mathrm{PS}}^{\mathrm{NC}} \approx q^2 r_L^2 \nu$,where q, r_{L} and ν are the safety factor, the Larmor radius of the impurity ion and the Coulomb collision frequency between the impurity and the background ion, respectively. The estimated values of the neoclassical self-diffusion coefficient indeed becomes relatively large as $D_{neo} = 0.1 - 0.5$ m^2/s with the following parameters: $Z = 12$, $n_{\mathrm{D}^+} = 1.5 \times 10^{19}$ m^{-3}, $T_{\mathrm{W}} = 40 - 80$ eV, $T_{\mathrm{i}} = 40 - 200$ eV, $B = 3.2$ T, and $q = 5$ (at 98$\%$ magnetic flux surfaces) which are the typical values in the numerical simulation.

If this neoclassical self-diffusion is taken into account, the diffusion coefficient in Eq. (4.1) would become $D = D_{\mathrm{an}} + D_{\mathrm{neo}}$ and larger than the value only with the anomalous diffusion. Above tendency of larger perpendicular flux is possibly explained by the neoclassical self-diffusion effects.

4.3 Summary of Chapter 4

In this study, we have investigated the tungsten transport process perpendicular to the magnetic field in realstic tokamak geometry. Especially, we have focused on the effect of the neoclassical self-diffusion. The comparison between the IMPGYRO full-gyro orbit motion model and the guiding center approximation model has been performed in order to understand the effects of the neoclassical self-diffusion and its magnitude on the radial impurity transport.

The radial average velocities of impurities with the gyro orbit model by the IMPGYRO code (Case A) tend to be larger than those with the guiding center approximation model (Case B). The difference between those two results has been explained by estimating the diffusion coefficient of each case. The diffusion coefficient in Case A have a trend to be larger than those in Case B.

The reason why such a difference occurs may be explained by the neoclassical self-diffusion process, which is automatically taken into account in Case A. The more detailed comparison will be performed in the near future.

In addition to the neoclassical self-diffusion, other neoclassical effects such as the inward pinch and the temperature screening effects will be implemented into the IMPGYRO code by the numerical scheme developed in Refs. [6, 7, 8, 12]. These effects have been pointed out to be larger at least in a simple circular tokamak geometry in above references and will be studied as well in the near future.

References in Chapter 4

[1] S. Yamoto, *et al.*, Contrib. Plasma Phys. **56** (2016) 646.

[2] A. Fukano, *et al.*, J. Nucl. Mater. **363-365** (2007) 211.

[3] S. Yamoto, Y. Homma, K. Hoshino, *et al.*, J. Nucl. Mater. **463** (2015) 615.

[4] K. Shimizu, T. Takizuka, *et al.*, J. Nucl. Mater. **241-243** (1997) 167.

[5] D. Reiser, D. Reiter, *et al.*, Nucl. Fusion **38** (1998) 165.

[6] Y. Homma and A. Hatayama: J. Comp. Phys. **250** (2013) 206.

[7] Y. Homma *et al.*, in Proc. of the 25th IAEA Fusion Energy Conference, TH/P7-8, 2014. (St. Petersburg, Russian Federation)

[8] Y. Homma, *et al.*, Nucl. Fusion **56** (2016) 03609.

[9] S. P. Hirshman and D. J. Sigmar, Nucl. Fusion **21** (1981) 1079.

[10] D. Naujoks, K. Asmussen, M. Bessenrodt-Weberpals, *et al.*, Nucl. Fusion **36** (1996) 671.

[11] P. Helander and D. J. Sigmar, *Collisional Transport in Magnetized Plasmas*, Cambridge University Press, New York (2002).

[12] Y. Sawada, *et al.*, Transactions of Fusion Science and Technology, **63** (1T) (2012) 352.

[13] M. Toma, *et al.*, J. Nucl. Mater. **438** (2013) S620.

[14] R. Schneider, *et al.*, Contrib. Plasma Phys. **46** (2006) 3.

[15] Y. Ueda, *et al.*, Nucl. Fusion **49** (2009) 065027.

[16] A. Hatayama, *et al.*, Nucl. Fusion **40** (2000) 2009.

[17] K. Shimizu, *et al.*, Nucl. Fusion **49** (2009) 065028.

[18] T. Takizuka, *et al.*, J. Comp. Phys. **25** (1977) 205.

Chapter 5

Kinetic modeling of high-Z tungsten impurity transport in ITER plasmas using the IMPGYRO code in the trace impurity limit [1]

By using the IMPGYRO code, the W production/transport in the ITER geometry has been calculated under two different divertor operation modes (Case A: partially detached state and Case B: high recycling state) obtained from the SOLPS-ITER code suite calculation without the effect of drifts. The results show that the core penetration of W impurities strongly depends on the divertor operation mode. From the comparison of the W impurity transport between Case A and Case B, it is shown that the effectiveness of obtaining a partially detached state to reduce the core concentration of W impurities. In this first application of the IMPGYRO code to ITER plasmas, however, several important effects such as drifts of the background plasmas have not yet been included in the model. The limitations of the employed model and the validity of the above results are discussed and future problems are summarized for further applications of IMPGYRO code to ITER plasmas.

5.1 Introduction

With the move in current and future devices to all-metal walls, and particularly to tungsten (W) plasma-facing components, understanding heavy ion impurity transport processes in the scrape-off layer (SOL)/divertor region is becoming one of the most critical issues for tokamak operation. To date, W transport processes in these regions have been kinetically studied by various SOL/divertor impurity global transport codes such as DIVIMP [2], IMPMC [3], and DORIS [4].

However, these codes were originally designed to calculate trajectories of low-Z impurity species, such as C, Ar, Ne, etc, using the guiding centre approximation, which assumes the Larmor radius to be small compared with local gradients. The characteristics of high-Z impurity species compared to low-Z impurities are: (1) larger Larmor radius due to their high mass, and (2) higher atomic number meaning that higher charge states can be reached, which has consequences for the neoclassical transport of impurities. Employing the guiding centre approximation cannot reproduce Larmor motion and its resultant effects, such as prompt re-deposition at the divertor plates, and the drifts of impurities. Therefore, dedicated high-Z impurity transport codes should be developed not only to account for these features, but also to obtain a better understanding of high-Z impurity transport.

To improve this understanding, we are continuing to develop the kinetic SOL/divertor impurity transport code IMPGYRO [5, 6]. The code has the following characteristics which are important for calculating W transport: (1) the exact Larmor motion of W ions is computed so that the effects of drifts are automatically taken into account; (2) Coulomb collisions between W impurities and background plasma ions are modelled using the Binary Collision Model [7] which provides a precise kinetic numerical model of the friction and thermal forces [8, 9]. These characteristics are important especially for high-Z impurities like tungsten.

So far, a number of predictive W transport simulation of the ITER have been performed by various codes. The ERO code [10], which tracks the full orbit of W with sophisticated modeling of the sheath acceleration of W and plasma wall interactions, has been used to simulate the erosion of the W divertor targets in JET-ILW [11]. The DIVIMP code, which traces the guiding centre of W particles, has calculated the W density and the W erosion flux under various combinations of the wall materials [12]. However, as far as the W transport process in the SOL concerned, the simulation performed by ERO is limited to only the vicinity of the divertor plate. Also, as mentioned before, the DIVIMP code only follows the guiding centre of W particles and cannot calculate the effects of the drifts. In order to obtain a better understanding of the W transport processes in the SOL of the ITER, it is necessary to perform the global transport calculation with full orbit resolution.

In this chapter, we make a first step toward the predictive W transport simulation of the ITER operation scenario by kinetic impurity transport simulation code (IMPGYRO) to obtain basic understandings of the W transport processes in the SOL/ divertor.

In section 5.2, a brief summary of the simulation model and calculation conditions will be described. In section 5.3, numerical results are presented and discussed together with the background plasma profiles. We focus on the two typical ITER divertor operation scenarios, i.e. Case A (high recycling state) and Case B (partially detached state). In section 5.4, the limitations of the employed model and the validity of the results in section 5.3 will be discussed in detail. Finally, in section 5.5 the conclusion and the future problems are summarized.

5.2 Calculation Conditions

To calculate background plasma parameters, the SOLPS-ITER code suite [13, 14] has been used. The computational mesh for the ITER geometry is shown in Fig. 5.1. The background plasma is computed for burning plasma cases with the toroidal magnetic field B_0 = 5.3 T, the plasma current I_p = 15 MA and 100 MW of input power into the SOL, shared equally between ions and electrons. The toroidal field is taken to be the forward direction, i.e., the magnetic drifts of ions direct towards the X-point in Fig. 5.1.

The plasma species considered in this case are D, He, and Ne without drifts. Particle fluxes of 9.10×10^{21} $\mathrm{D}^{+}\ \mathrm{s}^{-1}$ and 2.13×10^{20} $\mathrm{He}^{2+}\ \mathrm{s}^{-1}$ are set at the inner core boundary. In this study, following two different amounts of Ne and D^2 seeding rate have been selected for the comparison:

Case A: Particle fluxes of $2.80 \times 10^{20}\ \mathrm{Ne\,s}^{-1}$ and $1.21 \times 10^{23}\ \mathrm{D}^2\ \mathrm{s}^{-1}$,
Case B: Particle fluxes of $1.50 \times 10^{20}\ \mathrm{Ne\,s}^{-1}$ and $2.44 \times 10^{22}\ \mathrm{D}^2\ \mathrm{s}^{-1}$.

An anomalous diffusion coefficient of $D_\perp = 0.3\ \mathrm{m}^2/\mathrm{s}$ and thermal diffusivities for electrons and ions of $\chi_\mathrm{e} = \chi_\mathrm{i} = 1.0\ \mathrm{m}^2/\mathrm{s}$ have been employed for radial transport coefficients in producing the SOLPS-ITER background. Above input parameters and conditions are specified based on the same baseline as those in modeling studies of ITER divertor performance in a carbon(C) free environment with SOLPS4.3 code suite [15]. The validity of these input parameters has been described in Ref. [16].

The W impurity transport has been calculated by means of the IMPGYRO code. The trace impurity limit has been supposed, therefore, the background plasma parameters are fixed and not affected by the W impurities for each of the cases above. Only the W sputtering by the bombardment of Ne particles onto the inner/outer divertor and baffle plates plates has been considered because the mass and the charge state are relatively larger than D and He. We have used the charge state resolved Ne fluxes from the SOLPS simulation The incident energy of Ne , Eincident, is calculated as $E_\mathrm{incident} = 2kT_\mathrm{i} + 3ZkT_\mathrm{e}$ [17], where Z is the charge state of Ne and k is the Boltzmann constant. The incident angle of Ne has been assumed to be normal to the divertor plate. By using E_incident and the incident angle obtained from the assumptions above, the sputtering yield and the initial energy of W is calculated from the tabulated TRIM.SP sputtering database [18]. A cosine distribution has been assumed for the angular distribution of sputtered W particles. All the particles reaching the core and wall boundaries are assumed to be absorbed. Therefore, the self-sputtering of W has been neglected. As for the cross-field transport process, the drifts are automatically taken into account. Also, the neoclassical self-diffusion of W [19], which is the resultant effect of the combination of the grad-B drift and Coulomb collisions, has been considered. The neoclassical temperature screening effect and the inward pinch of W [19], which are the consequence of the Pfirsh-Schluter flow and the heat flux of the background plasma, will be investigated in the future by considering the drifts

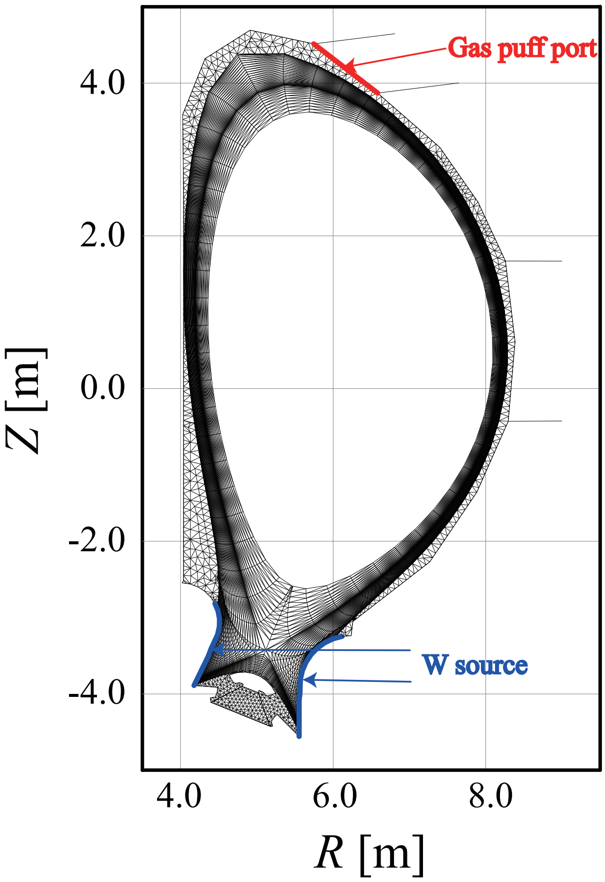

(a)

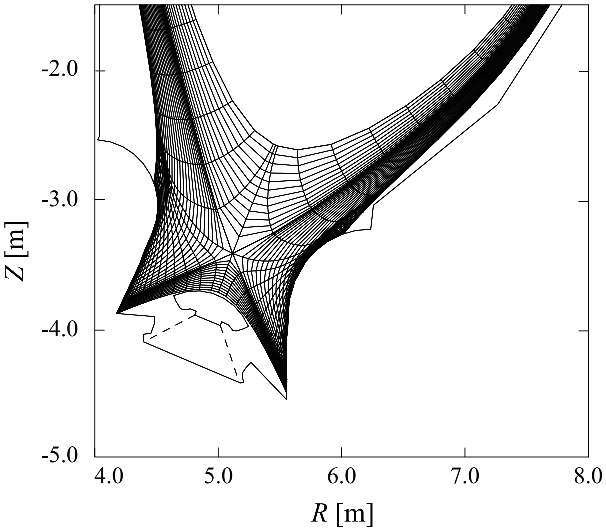

(b)

Figure 5.1: The SOLPS-ITER computational mesh for the ITER. The surface of the gas puff port and the W source in the calculation are also plotted in the figure: (a) the whole domain, and (b) the zoom in view of the divertor region. (cited from Ref. [1])

of the background plasma species in the SOLPS-ITER calculation. The anomalous diffusion coefficient $D_\perp = 0.3\ \mathrm{m^2/s}$ has been employed as same as that of the background ions.

5.3 Numerical Results

5.3.1 Background plasma profiles along the plates and divertor operation mode

In Fig. 5.2, the background temperature profiles calculated by SOLPS-ITER code suite have been shown along the outer divertor target and baffle plates as a function of the distance from the outer separatrix d m. Fig. 5.2 (a) and (b) are the ion temperature T_i and (b) the electron temperature T_e profiles, respectively. The profiles for Case A and Case B are compared with each other to understand the different characteristics of the divertor plasma. As seen from Fig. 5.2 for the outer divertor region, T_e and T_i are below 5eV near the strike point in Case A and a partially detached state has been reached in Case A. On the other hand, in Case B, T_e and T_i are still relatively high and have a peak at $d \sim 0.07$ m. Therefore the outer divertor region is considered to be a still high recycling state. In Fig. 5.3 (a) and (b) show T_i and T_e profiles, respectively, in the inner divertor region along the inner divertor and baffle plates. The results for Case A and Case B are compared in the same manner as in Fig. 5.2. In both Case A and Case B, T_i and T_e in the inner divertor region tend to be smaller than those in the outer divertor region. In Case B, however, even in the inner divertor region, T_i and T_e are still high. From above results, more precisely, from the background plasma temperature profiles in the outer divertor region, we characterize Case A as *partially detached state* and Case B as *high recycling state* for their divertor operation mode in the following sections. More detailed comparisons of the background plasma profiles will be given later in Sec. 5.3.4 in relation to the impurity transport process.

5.3.2 Two dimensional (2D) W-density profiles and core penetration

Figure 5.4 (a) and (b) compare the 2D W-density profiles calculated by the IMPGYRO code between Case A and Case B in the poloidal cross section. In Fig. 5.4, the W-densities are normalized by the local electron density. Clear difference between Case A and Case B is seen from the comparison between Fig.5.4 (a) and (b). In Case A, the sputtered W particles are localized near the baffle plates as shown in Fig. 5.5. Almost no W penetration to the core can be seen in this case. On the other hand, in Case B, the W particles penetrate into the core. In order to understand above clear difference of the W-impurity density profiles between Case A and Case B in Fig. 5.4, especially, to understand significant difference of core penetration

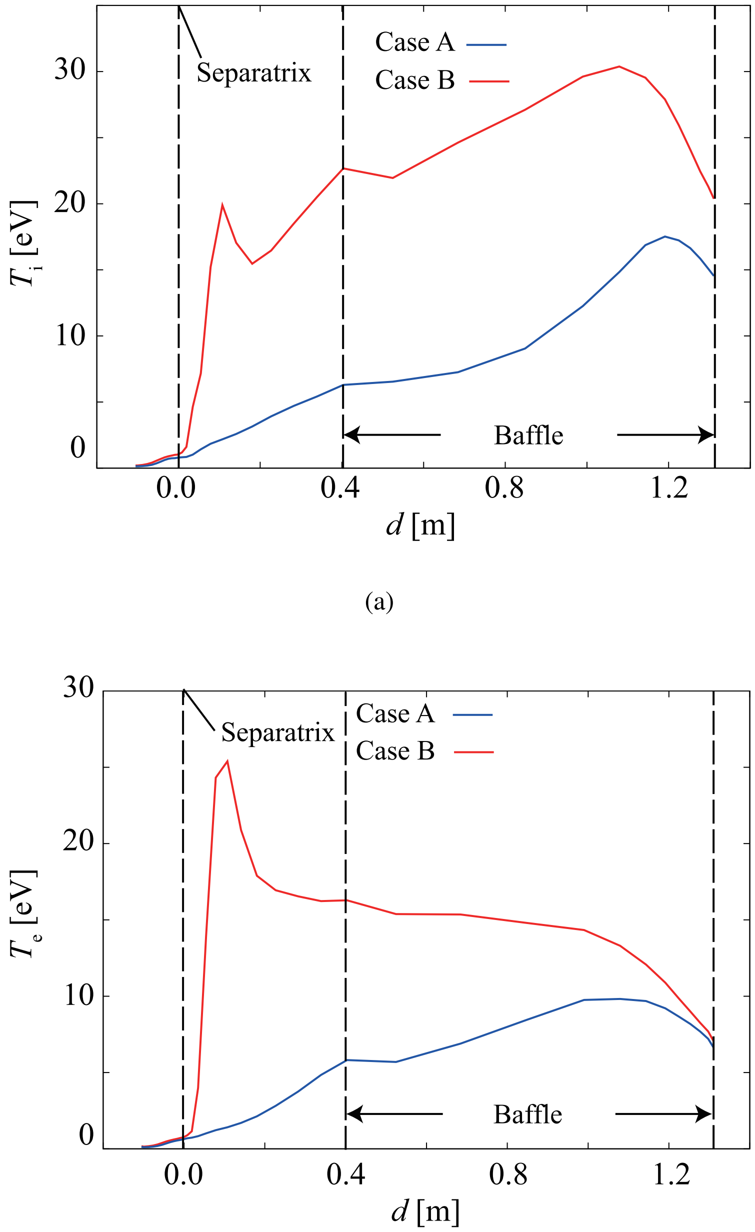

(a)

(b)

Figure 5.2: Temperature profiles along the outer divertor plate in both cases: (a) the ion temperature, and (b) the electron temperature, where d is the distance from the separatrix. (cited from Ref. [1])

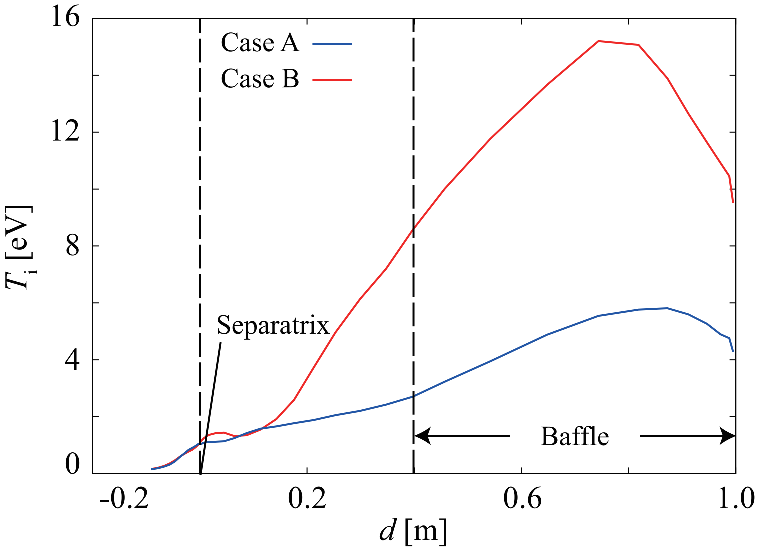

(a)

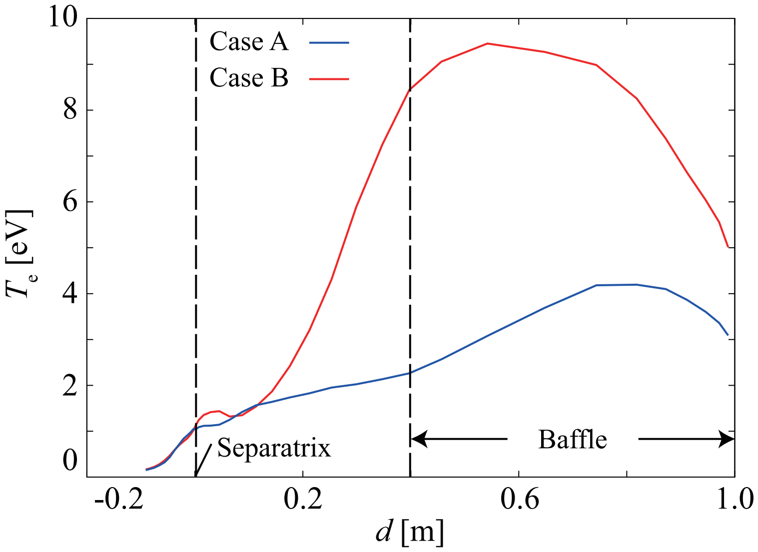

(b)

Figure 5.3: Temperature profiles along the inner divertor plate in both cases: (a) the ion temperature, and (b) the electron temperature. (cited from Ref. [1])

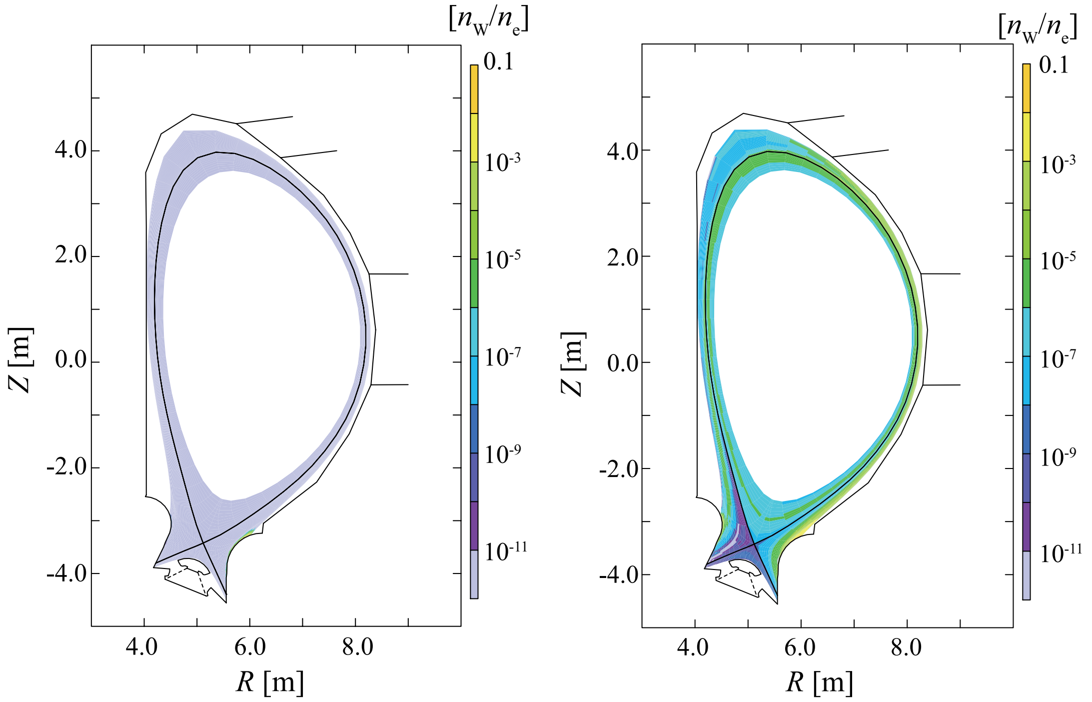

(a) (b)

Figure 5.4: Normalized W density profiles in both cases: (a) Case A, and (b) Case B. (cited from Ref. [1])

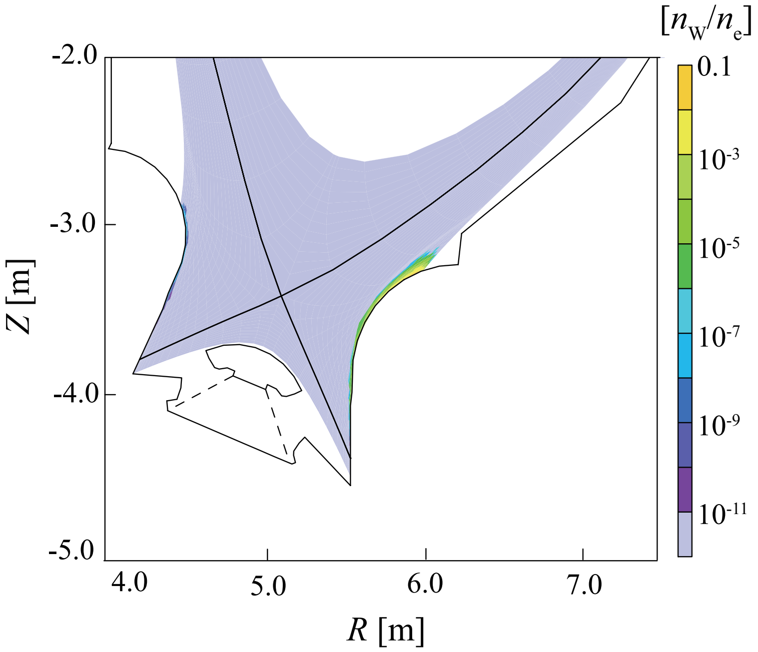

Figure 5.5: Zoom in view of the divertor region for the W density profile in Case A. (cited from Ref. [1])

characteristics, we will look into 1) the impurity source strength by sputtering on the divertor and baffle plates in Sec.5.3.3 and 2) the impurity transport process in Sec. 5.3.4 below.

5.3.3 W-impurity out-flux from the plates

First, we focus on the production amount of the W impurities, i.e., impurity source strength by sputtering and compare the W out-fluxes from the plates between Case A and Case B. The production amount depends mainly on the background plasma conditions in front of target plates. By using the temperature profiles in front of the target plates shown in Fig. 5.2 and Fig. 5.3 together with the Ne particle flux calculated by the SOLPS-ITER code suit, the W out-flux from the divertor and baffle plates is calculated as the product of the Ne flux and the W sputtering yield. Taking these W out-fluxes as the sources, the IMPGYRO follows the impurity transport process.

The calculated results of W out-fluxes are shown for the inner and outer region, respectively, in Fig. 5.6 (a), and (b). First, we focus on the inner divertor region in Fig. 5.6(a). A significant difference can be seen in Fig. 5.6(a). The W out-fluxes, i.e., the W source strengths for Case B along the divertor and baffle plates in the inner divertor region are considerably larger (about one order of magnitude) than those for Case A. At a first glance, this large difference of the W out-flux by sputtering in the inner region seems to be a possible reason for the difference of the W-impurity density in the core shown in Fig. 5.4. The W-densities in the core for Case B (high recycling state) in Fig. 5.6 are much larger than those for Case A (partially detached state), which is the same tendency as for the W out-flux in the inner divertor region shown above in Fig. 5.6(a).

The reason is, however, not so simple. We have done an additional calculation in order to make clear which region (the inner region and/or the outer region) is dominant source to explain the large W-penetration into the core for Case B in Fig. 5.6(b). In this additional calculation, all of the W-sources (W out-fluxes) along the outer divertor target plate and baffle plate in Fig. 5.6(b) have been artificially switched off, while the inner sources in Fig. 5.6(a) are kept the same as in the reference calculation. The result shows the amount of the W-impurity inside the core has been drastically reduced ($n_{\mathrm{W}}/n_{\mathrm{e}} < 10^{-11}$) and almost no W-impurity has been seen in the core region without the W impurity source in the outer region. Above result of the additional calculation suggests that the inner region is not the dominant source of the core W-impurity content in Case B, while the outer region is the dominant source of the large W-content in Case B.

From above discussion, next we focused on the outer divertor region and compare the source strength in Case A and Case B. As seen from Fig. 5.6(b), the source strength, i.e., W out-fluxes from the outer part (d >0.1 m in Fig. 5.6(b)) of the outer divertor region are almost the same for Case A and Case B. Although the W out-fluxes close to the separatirix ($d <$ 0.1 m in Fig. 5.6(b)) are much smaller than those in the outer part (d >0.1 m,especially d >0.4 m in Fig.

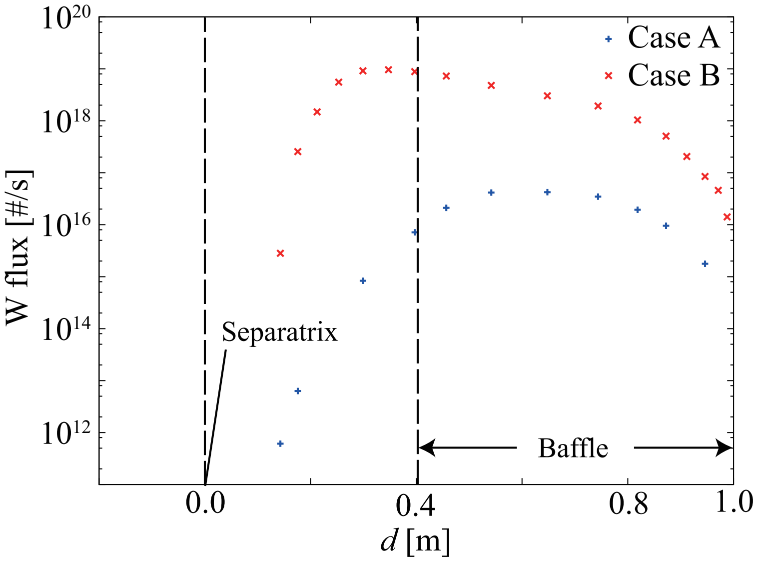

(a)

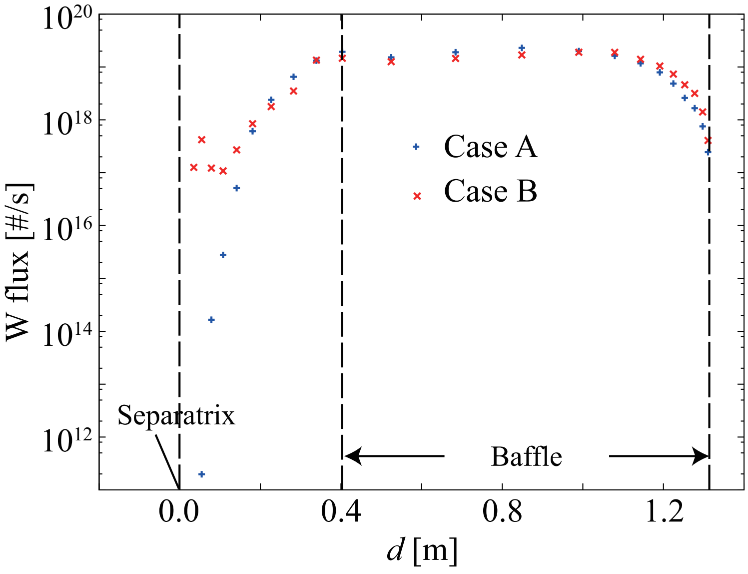

(b)

Figure 5.6: W outflux from the divertor plates: (a) the inner divertor plate, (b) the outer divertor plate. (cited from Ref. [1])

5.6(b)), the difference of W out-fluxes between Case A and Case B is significant. The peak of W out-flux observed in Case B at $d \sim 0.07$ m is mainly due to the peak of the background plasma temperature T_i and T_e shown in Fig. 5.2 in the outer divertor region, while W out-fluxes in Case A close to the separatrix drastically and monotonically decrease due to decrease in T_i and T_e by the partial detachment.

5.3.4 Impurity transport process

Impurity transport process in the SOL along the magnetic field line strongly depends on the force balance between the friction force $F_{\|,\mathrm{fr}}$ and the thermal force $F_{\|,\mathrm{th}}$ [20, 21]. These forces are caused by the Coulomb interaction between the background plasma ions and the W-impurity ions.

As explained below, it is difficult to separate the contribution from each force in the IMPGYRO calculations. We have used simple analytic expressions to estimate the contribution from each force. Before discussing the force balance in Case A and Case B in detail, we will first briefly summarize the calculation model of the collisional force acting on Monte Carlo test W-impurity particles in the IMPGYRO code and simple analytic expressions used to estimate separately the friction force and the thermal force. Then, the collisional force acting on the impurity particle and the resultant transport port process along the field line in the SOL/divertor will be shown to explain the difference in the 2D W-density profiles between Case A and Case B in Fig. 5.4.

Simple analytic expressions used to estimate the friction force

In the IMPGYRO code, the Monte-Carlo BCM (Binary Collision Model) model developed in Ref. [8, 9] has been implemented to simulate Coulomb collisions. In this model, the velocity of the background ion involved in each binary collision event $\mathbf{v}_b$ is sampled from the distorted Maxwellian $f(\mathbf{v}_b)$ for the background ion with a temperature T_i, a flow velocity $\mathbf{u}_($b)and a temperature gradient ∇T_i [see Eq.(3) of Ref. [8]]. With the velocity $\mathbf{v}_{(\mathrm{W,ip})}$ of the ip-th Monte Carlo test W-impurity ion, the relative velocity $\mathbf{u}^{rel}_{(W,ip-b)} = \mathbf{v}_{(\mathrm{W,ip})} - \mathbf{v}_b$ is used to calculate the velocity change $\Delta\mathbf{v}_{(\mathrm{W,ip})}$ of the W-impurity test ion by successive small angle Coulomb scattering during the time step Δt. Then, we can calculate the net force including both the friction force and the thermal force for the ip-th test ion by $\mathbf{F}_{(\mathrm{W,ip})} = m_\mathrm{W}((\Delta\mathbf{v}_{(\mathrm{W,ip})})/(\Delta t))$, where m_W is the mass of W ion.

In the present IMPGYRO calculations, the background ion temperature T_i, the flow velocity $\mathbf{u}_{(\mathrm{D}^+)}$ and temperature gradient ∇T_i have been given by the background profiles calculated from the SOLPS-ITER code suite in each numerical mesh. In other words, the shifted and distorted Maxwellian for the background ions $f(\mathbf{v}_b)$ has been reconstructed consistently with the fluid model, i.e., with the SOLPS-ITER code results.

Therefore, it is difficult to separate the contribution of the friction force and thermal force from the simulation results, because $\Delta\mathbf{v}_{(\mathrm{W,ip})}$ includes both effects of the friction and the thermal force. Instead, here, we estimate these forces from the following simple analytic equations Eqs. (5.1) and (5.2) below. These expressions have been used to check the numerical results calculated by the Monte-Carlo BCM model [8, 9]. Namely, the sum of the friction force and thermal force obtained from Eqs. (5.1) and (5.2) has been compared with the total average force obtained by taking the ensemble average of $\mathbf{F}_{(\mathrm{W,ip})}$ over the Monte-Carlo test W-ions, $<\mathbf{F}_{(\mathrm{W,ip})}>= (1/N_T)\sum_{ip}\mathbf{F}_{(\mathrm{W,ip})}$ (NT : the total number of test W-ions and reasonable agreement has been obtained in the test calculations in Ref. [8, 9]. The analytic expressions for the friction force $\mathbf{F}_{\mathrm{fr}}$ and the thermal force $\mathbf{F}_{\mathrm{th}}$ are given respectively as follows,

$$\mathbf{F}_{\mathrm{fr}} = -\frac{C}{4\pi}\frac{n_{D^+}}{2kT_{\mathrm{i}}}\frac{\Phi\left(u_{\mathrm{W}}\right) - u_{\mathrm{W}}\Phi'\left(u_{\mathrm{W}}\right)}{u_{\mathrm{W}}^3}\cdot\mathbf{u}_{\mathrm{W}}, \tag{5.1}$$

$$\mathbf{F}_{\mathrm{th}} = -\frac{C}{10\pi\sqrt{\pi}}\sqrt{\frac{m_{\mathrm{D}^+}}{2kT_{\mathrm{i}}}}\frac{1}{\left(kT_{\mathrm{i}}\right)^2}\exp\left(-u_{\mathrm{W}}^2\right)\cdot\left[\mathbf{q} - 2\left(\mathbf{q}\cdot\mathbf{u}_{\mathrm{W}}\right)\mathbf{u}_{\mathrm{W}}\right], \tag{5.2}$$

where $C \equiv (\ln\Lambda)\left(\frac{q_{\mathrm{W}}q_{\mathrm{D}^+}}{\varepsilon_0}\right)^2\left(1 + \frac{m_{\mathrm{D}^+}}{m_{\mathrm{W}}}\right)$, $\mathbf{q} = -\kappa_{\|}\nabla_{\|}kT_{\mathrm{i}} + \kappa_{\wedge}\mathbf{e}_{\|}\times\nabla_{\perp}kT_{\mathrm{i}} - \kappa_{\perp}\nabla_{\perp}kT_{\mathrm{i}}$, and $\mathbf{u}_{\mathrm{W}} \equiv \sqrt{\frac{m_{\mathrm{D}^+}}{2kT_{\mathrm{i}}}}\left(\mathbf{v}_{\mathrm{W}} - \mathbf{u}_{\mathrm{D}^+}\right)$. The Coulomb logarithm $\ln\Lambda = 15$ has been employed in the calculation. The symbol Φ and Φ' are described by the following equations:

$$\Phi\left(\mathbf{u}_{\mathrm{W}}\right) \equiv \frac{2}{\sqrt{\pi}}\int_0^{u_{\mathrm{W}}}\exp\left(-t^2\right)\mathrm{d}t, \tag{5.3}$$

$$\Phi'\left(\mathbf{u}_{\mathrm{W}}\right) \equiv \frac{\mathrm{d}\Phi\left(\mathbf{u}_{\mathrm{W}}\right)}{\mathrm{d}\mathbf{u}_{\mathrm{W}}} = \frac{2}{\sqrt{\pi}}\exp\left(-u_{\mathrm{W}}^2\right). \tag{5.4}$$

To obtain $\mathbf{F}_{\mathrm{fr}}$ and $\mathbf{F}_{\mathrm{th}}$ from Eqs. (5.1) and (5.2), the SOLPS-ITER results have been used to specify the heat flux density q, D^+ density n_{D^+}, the ion temperature T_{i}, and the D^+ flow velocity $\mathbf{u}_{\mathrm{D}^+}$. The W ion velocity $\mathbf{v}_{\mathrm{W}}$ and its charge q_{W} are specified from those of the ip-th test W-ion from the IMPGYRO calculation, and $\mathbf{F}_{\mathrm{fr}}$ and $\mathbf{F}_{\mathrm{th}}$ for each ip-th test W-ion ($\mathbf{F}_{\mathrm{fr},ip}$ and $\mathbf{F}_{\mathrm{th},ip}$) are calculated. Then, the ensemble average ($<\mathbf{F}_{\mathrm{fr}}>$, $<\mathbf{F}_{\mathrm{th}}>$) is taken over all the test W-ions in each numerical cell as in the actual IMPGYRO simulation described above. In this way, the parallel component of each force $F_{\|,\mathrm{fr}} =<\mathbf{F}_{\mathrm{fr}}\cdot\mathbf{e}_{\|}>$ and $F_{\|,\mathrm{th}} =<\mathbf{F}_{\mathrm{th}}\cdot\mathbf{e}_{\|}>$ can be separately obtained by taking the inner product of each force and the unit vector $\mathbf{e}_{\|}$ parallel to the magnetic field line.

Friction force and thermal force along the field line

The friction force $F_{\|,\mathrm{fr}}$ and the thermal force $F_{\|,\mathrm{th}}$ are calculated along the two magnetic field lines, which hit the outer target/baffle plate at the position d= 0.07 m and d=1.0 m in Fig. 5.6

(a), respectively. As was discussed in Sec.5.3.3 above, the outer region seems to be responsible for the core W-penetration seen shown in Fig. 5.4(b). The outer region may be further classified into two typical regions from the view point of the W-source strength discussed in Sec.5.3.3, i.e., 1) Region O1: the region close to the separatrix (d <0.1 m) and 2) Region O2 : the outer region mainly consists of the outer baffle plate in Fig. 5.6(b). Therefore, we have taken the point a) d =0.07 m and b) d =1.0 m as a representative point for each region (Region O1 and Region O2).

Figure 5.7(a) shows the friction force $F_{\|,\mathrm{fr}}$ and the thermal force $F_{\|,\mathrm{th}}$ for Case A (partially detached state) along the magnetic field line for d = 0.07 m in the Region O1 near the separatrix, while Fig. 5.7(b) shows $F_{\|,\mathrm{fr}}$ and $F_{\|,\mathrm{th}}$ along the same field line for Case B (high recycling state). In Fig. 5.7, the horizontal axis s is the distance along the field line and s=0 corresponds to the outer mid-plane (OM). In addition, XP, OD, and ID are corresponding to the X-point, the outer divertor plate and the inner divertor plate. The sign of $F_{\|,\mathrm{fr}}$ and $F_{\|,\mathrm{th}}$ is defined according to their direction. If the force directed towards the outer target, then $F_{\|,\mathrm{fr}}$, $F_{\|,\mathrm{th}} > 0$. On the other hand, if the force directed towards the inner target, then $F_{\|,\mathrm{fr}}$, $F_{\|,\mathrm{th}} < 0$. In the same way as Fig. 5.7, $F_{\|,\mathrm{fr}}$ and $F_{\|,\mathrm{th}}$ along the magnetic field line for d= 1.0 m in the Region O2 are shown in Fig. 5.8(a) and (b), respectively, for Case A and for Case B. The abbreviations IB, and OB are corresponding to the inner baffle, and the outer baffle, respectively.

Based on$F_{\|,\mathrm{fr}}$ and $F_{\|,\mathrm{th}}$ in Fig. 5.7, (a) the net force $F_{\|,\mathrm{fr}}+F_{\|,\mathrm{th}}$ together with the background plasma profiles of (b) D^+ density n_{D^+}, (c) the ion temperature T_i, and (d) the D^+ flow velocity $u_{\|,\mathrm{D}^+}$ along the field line with d=0.07 m in the Region O1 are plotted in Fig. 5.9(c), (d), (e) and (f), respectively. On the other hand, these parameters along the field line with d=1.0 m in the Region O2 are also shown in Fig. 5.10(a), (b), (c) and (d) respectively.

First, we focus on the outer region and look into the force balance. Table 5.1 summarizes the force balance for the outer divertor region with the results shown in Figs. 5.7-5.10. As seen from Table 5.1, the net force F_net only for Case B in the Region O1 close to the separatrix becomes $F_\mathrm{net} < 0$, while other cases F_net become $F_\mathrm{net} > 0$. As mentioned above, if the force directed towards the outer target, then $F_\mathrm{net} > 0$. On the other hand, if the force directed towards the inner target, then $F_\mathrm{net} < 0$. Therefore, only for Case B in the Region O1 close to the separatrix, W ions are driven towards the upstream, while all other cases W ions are forced to come back towards the outer diveror plate.

To confirm the summary in Table 5.1, we will look into the results shown in Fig. 5.7-5.10 in detail step-by-step. As seen from Fig. 5.7(a) for Case A in the Region O1 close to the separatrix with d=0.07 m, the friction force $F_{\|,\mathrm{fr}}$ towards divertor plate $F_{\|,\mathrm{fr}} > 0$) significantly large just in front of the outer divertor plate [we can see several data points almost along the vertical line OD in Fig. 5.7(a)]. This is due to rapid and significant increases in the flow velocity $u_{\|,\mathrm{D}^+}$ and also the density n_{D^+} of the background D^+ ions towards the plate [see Fig. 5.9(b) and (c)]. The thermal force also increases quite rapidly, but with the opposite direction $F_{\|,\mathrm{th}} < 0$) towards the upstream due to the large temperature gradient in front of the target plate [see Fig. 5.9(d)]. The

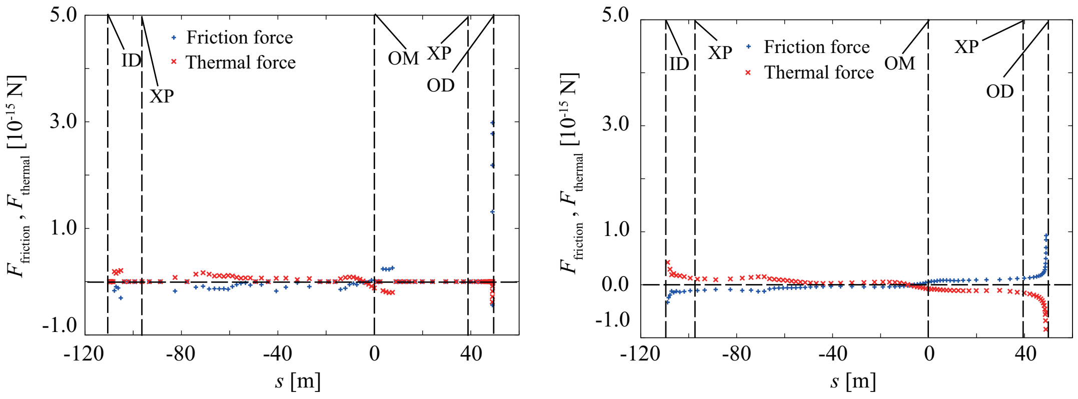

(a) Case A

(b) Case B

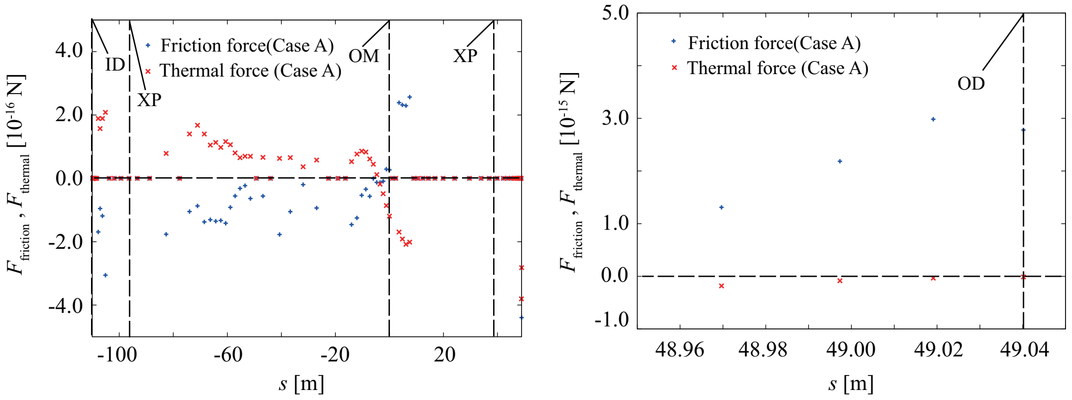

(c) Case A: in the SOL

(d) Case A: close to the outer divertor

Figure 5.7: Thermal force and friction force plotted along the field line at d =0.07 m:(a) Case A, (b) Case B. Figures (c) and (d) are the zoom in view of the forces in the SOL region and close to the outer target plate, respectively. The horizontal axis s is the distance along the field line and s =0 corresponds to the outer mid-plane (OM). In addition, XP, OD, and ID are corresponding to the X-point, the outer divertor plate and the inner divertor plate, respectively. (cited from Ref. [1])

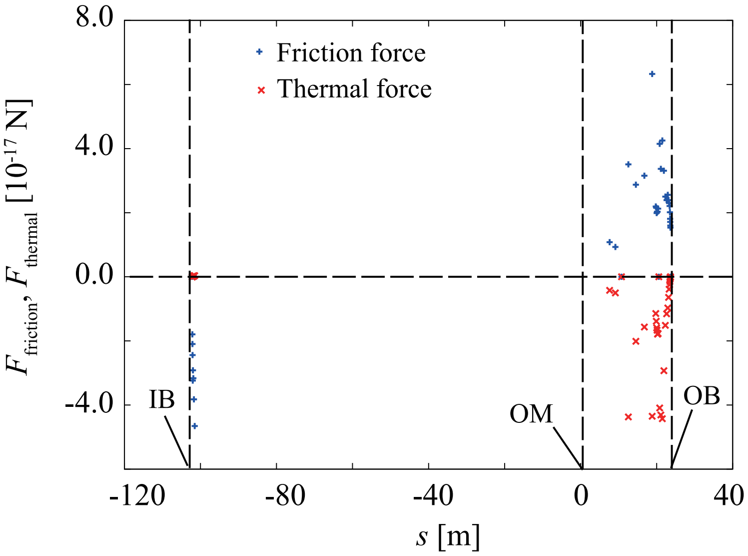

(a) Case A

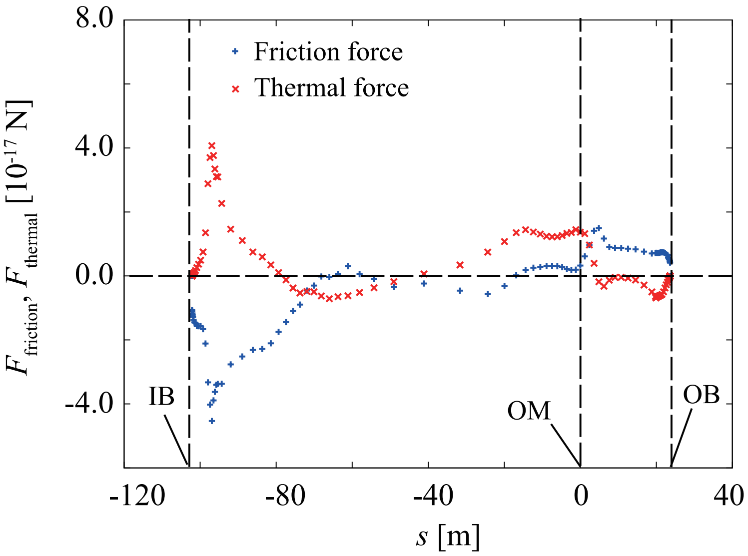

(b) Case B

Figure 5.8: Thermal force and friction force plotted along the field line at d =1.00 m: (a) Case A, (b) Case B. The horizontal axis s is the distance along the field line and s =0 corresponds to the outer mid-plane (OM). In addition, OB, and IB are corresponding to the outer baffle plate and the inner baffle plate. The dashed line in the horizontal axis indicates y=0. (cited from Ref. [1])

Table 5.1: Summary of the force balance along the magnetic field line in the outer divertor region; region O1 at $d = 0.07$ m and region O2 at $d = 1.00$ m. (cited from Ref. [1])

Outer divertor			
Region O1 (figures 5.7 and 5.9)	Case A	$F_{\mathrm{net}} > 0$	$\lvert F_{\mathrm{fr}}\rvert > \lvert F_{\mathrm{th}}\rvert$
	Case B	$F_{\mathrm{net}} < 0$	$\lvert F_{\mathrm{fr}}\rvert < \lvert F_{\mathrm{th}}\rvert$
Region O2 (figures 5.8 and 5.10)	Case A	$F_{\mathrm{net}} > 0$	$\lvert F_{\mathrm{fr}}\rvert > \lvert F_{\mathrm{th}}\rvert$
	Case B	$F_{\mathrm{net}} > 0$	$\lvert F_{\mathrm{fr}}\rvert > \lvert F_{\mathrm{th}}\rvert$

friction force dominates ($|F_{\|,\mathrm{fr}}| > |F_{\|,\mathrm{th}}|$) and the net force F_{net} becomes $F_{\mathrm{net}} > 0$ in front of the outer target plate close to the separatrix.

For Case B in Fig. 5.7(b), however, the thermal force dominates ($|F_{\|,\mathrm{fr}}| < |F_{\|,\mathrm{th}}|$) in front of the target plate and the net force becomes $F_{\mathrm{net}} < 0$ in front of the outer target [see Fig. 5.9(a)]. As a result, W ions are transported towards the upstream in Case B. The magnitude of the net force is not so large as that in Case A, because the difference between $|F_{\|,\mathrm{fr}}|$ and $|F_{\|,\mathrm{th}}|$ is not so large as seen from Fig. 5.7(b).

It should be noted that in Case B a flow reversal of the background D^+ ion ($u_{\|,\mathrm{D}^+} < 0$) takes place in front of the target plate, i.e., the background D^+ ion flow directs towards *not* the outer divertor plate, but the upstream in the outer divertor region close to the separatrix. This flow reversal in Case B (high recycling state) may be caused by a large amount of the recycling ionization source in front of the target plate close to the separatrix discussed in Ref.[22]. Although the D^+ ions flow towards the upstream ($u_{\|,\mathrm{D}^+} < 0$) due to the flow reversal, the friction force is still positive ($F_{\|,\mathrm{fr}} > 0$) in the outer SOL/divertor region (0 m $< s <$ 40 m) towards the outer divertor plate. The reason is the same as discussed in Ref. [23] and summarized as follows: 1)W ions are accelerated mainly due to the strong thermal force just in front the target plate and obtain a relatively high velocity towards the upstream ($u_{\|,\mathrm{D}^+} < 0$) than the background D^+ ions, 2) the friction force $F_{\|,\mathrm{fr}} \propto -(u_{\|,\mathrm{W}} - u_{\|,\mathrm{D}^+})$ possibly becomes positive $F_{\|,\mathrm{fr}} > 0$. Indeed, W ions transported from the outer plate by the strong thermal force start being decelerated after their passing through the outer mid-plane (vertical line OM in Fig. 5.9) due to the reversed temperature gradient [see Fig. 5.9(d)] and the resultant change of the thermal force direction. Then, the magnitude of the W ion velocity become smaller and if $|u_{\|,\mathrm{W}}| < |u_{\|,\mathrm{D}^+}|$, then $F_{\|,\mathrm{fr}} \propto -(u_{\|,\mathrm{W}} - u_{\|,\mathrm{D}^+})$ may change the sign, i.e., $F_{\|,\mathrm{fr}} < 0$.

As seen from Fig. 5.8(a) for Case A in the outer SOL/divertor region (Region O2 with d=1.0 m), these forces are almost same. The friction forth $F_{\|,\mathrm{fr}}$, however, becomes slightly larger than the thermal $F_{\|,\mathrm{th}}$. As a result, the net force becomes $F_{\mathrm{net}} > 0$ as shown in Fig. 5.10(a), but rather weak in comparison with F_{net} in the Region O1 close to the separatrix. It should be noted that the scale of the vertical axis is two order magnitude smaller than that in Fig. 5.7 and Fig. 5.9.

It should be also noted that almost no data points are seen in the upstream region beyond the outer mid-plane in Fig. 5.8(a). This might be explained by the strong decrease in the ion

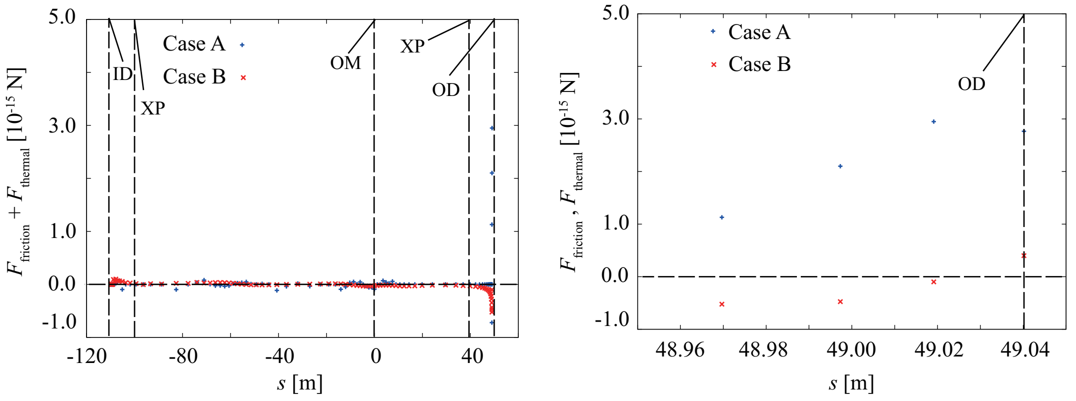

(a) Net force

(b) Net force: near the outer divertor

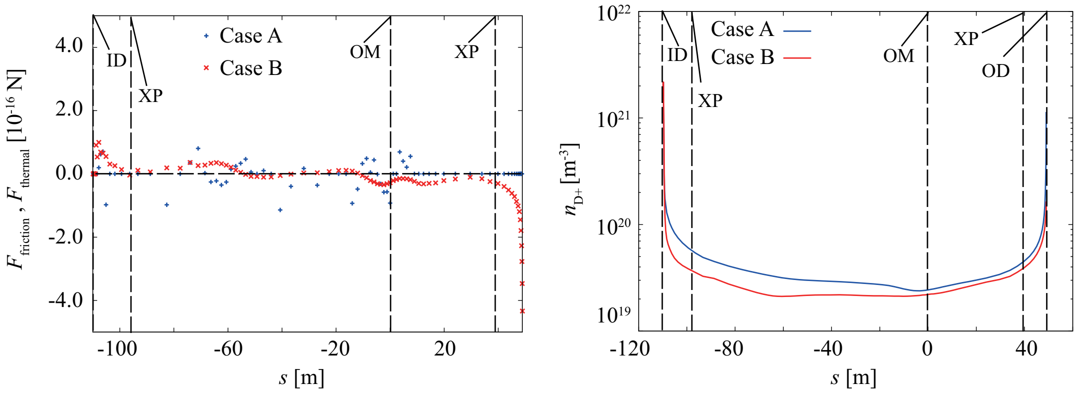

(c) Net force: away from the outer divertor

(d) D^{+} density

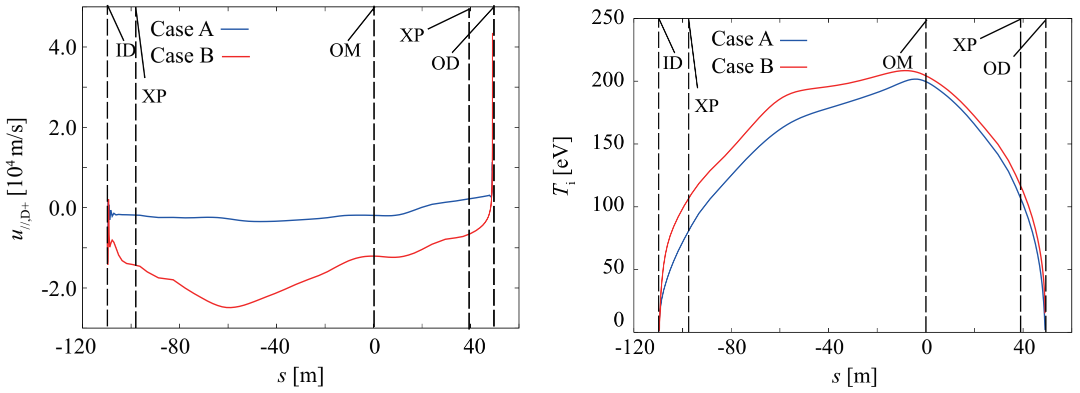

(e) D^{+} parallel flow velocity

(f) Ion temperature

Figure 5.9: Impurity and background plasma parameters plotted along the field line at d=0.07m:(a) the net force, (b) the zoom in view of the net force near the outer divertor plate, (c) the zoom in view of the net force away from the divertor plate. (d) the D^{+} density, (e) the D^{+} parallel flow velocity, and (f) the background ion temperature. (cited from Ref. [1])

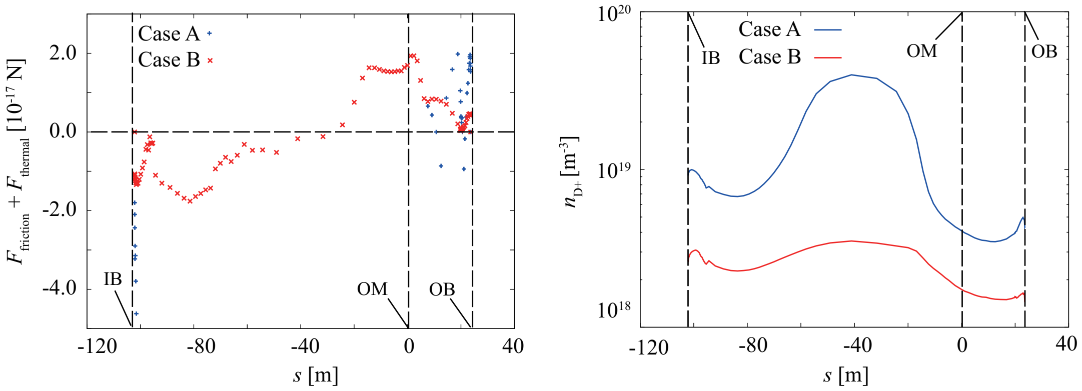

(a) Net force

(b) D^+ density

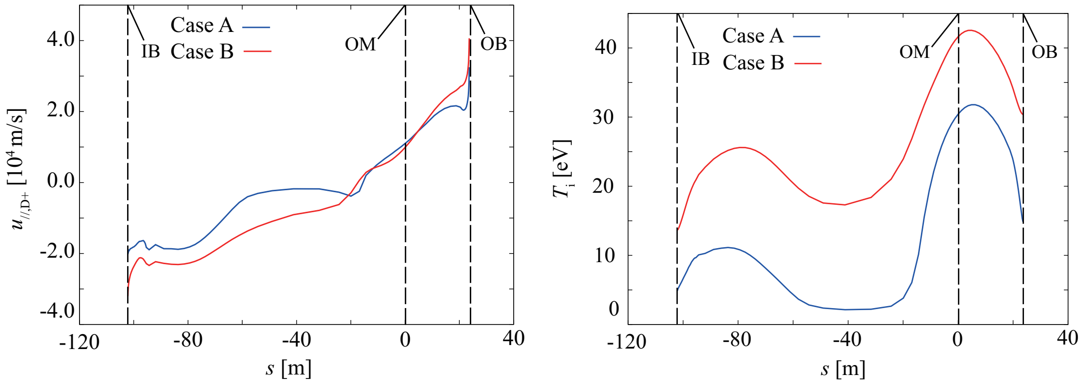

(c) D^+ parallel flow velocity

(d) Ion temperature

Figure 5.10: Impurity and background plasma parameters plotted along the field line d=1.00 m:(a) the net force, (b) the D^+ density, (c) the D^+ parallel flow velocity, and (d) the background ion temperature. The dashed line in the horizontal axis indicates y=0. (cited from Ref. [1])

Table 5.2: Summary of the force balance along the magnetic field line in the inner divertor region; region I1 at $d = 0.06$ m and region I2 at $d = 0.56$ m. (cited from Ref. [1])

Outer divertor			
Region I1 (figures 5.7 and 5.9)	Case A	–[1]	–[1]
	Case B	–[1]	–[1]
Region I2 (figures 5.8 and 5.10)	Case A	$F_{\rm net} < 0$	$\lvert F_{\rm fr}\rvert > \lvert F_{\rm th}\rvert$
	Case B	$F_{\rm net} < 0$	$\lvert F_{\rm fr}\rvert > \lvert F_{\rm th}\rvert$

temperature $T_{\rm i}$ towards the upstream beyond the vertical line OM (the outer mid-plane) [see Fig. 5.10(d)]. Due to this temperature gradient $\nabla T_{\rm i} > 0$, the thermal force directs towards the downstream towards the outer target, $F_{\parallel,\rm th} \propto \nabla T_{\rm i} > 0$. These two effects prevent W ions from transporting towards the upstream SOL in Case A.

As seen from Fig. 5.8(b) in the outer SOL/divertor region along the field line with d=1.0 m, the friction force towards the outer divertor plate $F_{\parallel,\rm fr}$ is slightly larger than the thermal force $F_{\parallel,\rm th}$ in the divertor region and the net force becomes $F_{\rm net} > 0$, and this makes W ions coming from the region O2 transport towards downstream along the field line. It should be noted that in Fig. 5.10(a), there exists a small amount of W ions in the upstream region, these particles may be originally transported towards upstream region from the Region O1, and then radially transported outward due to the anomalous diffusion. Indeed, this has been confirmed by the test run in which the W-outflux in the Region O2 has been turned off. The W density profiles in the upstream SOL has not been so much changed with and without the W-outflux in the Region O2.

Next, we look into the force balance in the inner divertor region. It should be noted that the magnetic field line starting from the point with $d = 0.07$ m on the outer divertor plate is mapped to the point near the inner separatrix with $d = 0.06$ m on the inner divertor plate, while the field line from $d = 1.00$ m in the outer baffle plate is mapped to the point with $d = 0.56$ m on the inner baffle plate.

Table 5.2 summarize the force balance just in front of the inner region (close to the vertical line ID). It has been already shown in Fig. 5.6(a) in Sec. 5.3.3 that the W-source strength, i.e., W out-fluxes close to the inner separatrix ($d <$ 0.1 m: Region I1) are significantly small even for Case B. As a result, almost no W-impurities are seen in this region in front of the inner target plate. Therefore, it is difficult to calculate the friction force $F_{\parallel,\rm fr}$ and the thermal force $F_{\parallel,\rm th}$ for the Region I1 close to the separatrix. In this case, we put symbol - (hyphen: -, which means almost no W ions) in Table 5.2.

On the other hand, in the outer part of the inner region with d = 0.56 m (Region I2), the net forces both for Case A and Case B direct towards the inner target plate as seen from Fig. 5.10(a). Therefore, in both Cases, W ions sputtered from the inner baffle plate are considered to be driven back towards the inner plates.

From Table 5.1 and 5.2, and above discussion, it has been shown that the W sputtering

---

[1] The forces could not be calculated since the W outflux is significantly small in the region I1

sources close to the outer separatrix for Case B possibly has a dominant contribution to the W ions in the upstream SOL at least under the present model and calculation conditions. The W particles mainly from the Region O1 in the outer divertor region close to the separatrix are stagnated around the region $s \sim$ -5 m due to the force balance parallel to the magnetic field line, where the temperature gradient becomes zero and then they are transported radially by the combination of anomalous diffusion and the grad-B drift.

From the results above, in Case A, almost no concentration of W ions can be seen, while relatively high W-density in Case B in the upstream SOL. The high W-density in the SOL in Case B is mainly due to the W particles sputtered out from the outer strike point. In this sense, to obtain partially detached divertor state is suggested to be effective to reduce the impurity content in the upstream SOL at least under the present model. As will be discussed in the next section, however, further model improvement including the effects of the drifts, neoclassical transport, ELMs will be necessary in the future.

5.4 Discussion

In order to make clear the limitation of the present modeling and to specify the range of validity of the results given in Sec. 5.3, we will discuss simplifications and/or assumptions used in the present model and also we will summarize important effects to be included for further progress in the future study.

5.4.1 Limitations of Present Impurity Production Modeling

Effects of sheath on the incident angle and the incident energy

As described in Sec. 5.2, a simple model has been adopted in the present study for the incident energy E_{incident} and the incident angle $\theta_{\mathrm{incident}}$ of Ne ions to the surface of the target plates and the baffle structures.

In order to specify these parameters more precisely, it is necessary to model the sheath potential structure and particle dynamics in the magnetic pre-sheath and the Debye sheath self-consistently by using full-kinetic approach, e.g., PIC (Particle in Cell) simulation. In Refs.[24, 25], systematic studies of incident angle distribution by full-Kinetic PIC simulation for various conditions (grazing angle ψ of the magnetic field to the surface, Larmor radius of incident ions ρ, electron Debye length λ_{De}) and also comparisons of the full-kinetic results with those by a simple model(In Ref.[24], gyro-kinetic approach, while in Ref. [25] a fluid Monte Carlo approach) have been done. For the small grazing angle of the magnetic field to the plate (e.g., ψ=85 degree) as in the present study, these studies suggest that the incident angle becomes in the range of $\theta_{\mathrm{incident}} \sim$ 60-80 degrees for the wide range of the parameter space $\rho/\lambda_{\mathrm{De}}$ =1-16.

Based on these results, we have done additional calculations of sputtering yield by taking the incident angle as a parameter with the TRIM-SP code. The calculated sputtering yield ($Y_{\mathrm{Ne}\to\mathrm{W}} \sim 0.8$) with $\theta_{\mathrm{incident}}$ = 70 degree becomes larger than that ($Y_{\mathrm{Ne}\to\mathrm{W}} \sim 0.55$) with $\theta_{\mathrm{incident}}$ = 0 degree (normal incidence), but only within a factor of 1.5 with a typical incident energy E_{incident} = 1keV of fully ionized Ne ion, which is roughly estimated from the formula $E_{\mathrm{incident}} = 2kT_{\mathrm{i}} + 3ZkT_{\mathrm{e}}$ with Z_{Ne} = 10, T_{e} = 30 eV. From this rough estimate, the W impurity amount in the upstream SOL for the Case B seems not to be so much changed.

The incident energy, however, is also affected by the sheath structure, and above simple formula of the E_{incident} is obtained for the simple Debye sheath without magnetic pre-sheath. Therefore, more detailed model (e.g., model used in Refs.[24, 25] above) will be needed in the future.

Effects of sputtering by other species (D, He) and wall sources

Effects of sputtering of W by D and He at the target and baffle plates have been neglected in this study. At least under the present background conditions (both Case A and Case B) and sputtering model used, sputtering of W by other species (D, He) except for Ne is negligible, because the sputtering yield of W by D and He are considerably smaller than by Ne. In addition, it has been pointed out that main chamber sources of W are not an issue for ITER because of the Be-wall - contrary to present day all-W devices in Ref. [26].

In the future, however, sputtering of these particles should be taken into account, especially, the effect of high energy charge exchange (CX) neutrals from the hot core and also high energy ions ejected from the core during ELMs (Edge Localized Mode) have to be taken into account.

Effects of W self-sputtering

In this paper, we have neglected the effect of W-self sputtering. In the present results, the charge state Z_{W} of W ions in front of the outer region becomes at most $Z_{\mathrm{W}} \sim 4$ and their average energy $< E_{\mathrm{W}} >$ is roughly $\sim$ 5 eV. The incident energy is estimated to be less than 200 eV from the simple formula $E_{\mathrm{incident}} = 2k < E_{\mathrm{W}} > +3Z_{\mathrm{W}}kT_{\mathrm{e}}$ described in Sec.2 with $T_{\mathrm{e}} \sim$ 15 eV in front of the outer baffle where the W densities are relatively high ($n_{\mathrm{W}}/n_{\mathrm{e}} \sim 10^{-3}$). The W self-sputtering yield Y_{W} becomes still less than 1 ($Y_{\mathrm{W}} \sim 0.1 - 0.2 < 1$) for above energy range from various sputtering formula/model (e.g., Bohdansky formula, Smith's formula, or Matsunami's formula : see Fig.8 of Ref. [27]) and also from TRIM data [18] used in the present simulation. However, more systematic analysis of prompt re-deposition and W-self-sputtering as in Ref. [5, 28, 29, 30] will be required.

5.4.2 Limitations of Present Impurity Transport Modeling

Effects of drifts of the background plasmas

As mentioned in Sec. 5.2, the present study is based on the SOLPS-ITER code suite with SOLPS version 4.3 and effects of the drifts for the background plasmas have been neglected. As has been pointed out in Refs.[31, 32] with SOLPS version 5.2, the drifts largely affect the flow-velocity distribution of the background plasmas in the SOL. In order to reproduce more realistic flow patterns observed in the experiments [31, and references therein], it is necessary to take into account the effects of drifts.

The change in the background flow pattern in the SOL affects the friction force on impurities [see Eq. (5.1)]. The drifts can also produce convective heat flows. As a result, ion temperature profiles and the resultant thermal force distribution on impurities [see Eq. (5.2)] are possibly altered. Based on above discussion, the SOLPS-ITER code suite [13, 14] with SOLPS 5.2[31, 32] to take into account the effects of drifts on the tungsten impurity transport will be necessary in the future.

Comparisons of the present results with those including the effects of drifts will be useful in order to more clearly understand and/or to make clear the effects of the drifts on the impurity transport. The present results without drifts gives a useful basis for such comparisons in the future.

Effects of Neo-Classical transport

Another important effects by the consequence of the background plasma drifts are the inward pinch effect (IWP) and temperature screening effect (TSE). The former (IWP) and the latter (TSE) effect are respectively caused by the Pfirsch-Schlüter (PS) particle flow and the PS heat flow of the background plasmas originally due to diamagnetic drifts. In the present study, however, we have neglected these neo-classical effects.

In Ref.[34], the neoclassical transport of tungsten in the H-mode edge transport barrier (ETB) of ITER has been investigated by almost the same model as that in Ref.[35], which will be explained more in detail below. It is shown that the radial convection velocity of tungsten is outward directed for a large proportion of the tested pedestal profiles. This is due to a combination of the high pedestal temperatures and the high separatrix densities making the outward directed TSE predominant contribution of the collisional convection. Therefore, it is important to model the effect of pedestal correctly and to take into account the resultant neoclassical transport for evaluation of the tungsten core concentration. In other words, not only the divertor operation mode considered present paper (i.e. Case A and Case B), but also core operation mode is very important for more overall understanding of impurity transport in the edge plasma and for the evaluation of the tungsten core content.

Recently, we have developed a new kinetic numerical scheme for neoclassical impurity particle transport simulation [19]. Our kinetic scheme is able to simulate the IWP, and the TSE, which have been neglected in most of existing kinetic impurity transport simulations in tokamak plasmas. Characteristics of the neoclassical transport (IWP and TSE), such as dependencies on the safety factor and on the impurity charge number, have been confirmed by a series of test simulations with a simple tokamak geometry in the collisional PS regime. The model has been extended also towards more collisionless regime [36].

This new kinetic numerical scheme can be implemented into kinetic/Monte Carlo impurity transport codes like IMPGYRO. Once if the background plasma profiles including the effects of drifts are given, more self-consistent kinetic simulations including the above effects of neoclassical transport will be possible. Therefore, now we are implementing the kinetic model above into IMPGYRO code, and the background profiles including the effects of drifts will be obtained by SOLPS-ITER code suite with SOLPS version 5.2. The results and comparisons with the present results will be reported elsewhere.

Effects of ELMs

As have been extensively studied in Refs.[35, 37], ELMs (ELM:Edge Localized Mode) and their effects on impurity transport are also crucially important to evaluate the tungsten content in the core.

In Ref. [37], simulations of ELMs by 2D fluids code SOLPS [38] show that W-impurity contamination of the core plasma strongly depends on the model for W expulsion by ELMs, i.e., core W-tungsten content increases with ELM frequency for gdiffusiveh model where W expulsion is modelled by an increase in the particle diffusion coefficient, while it decreases with ELM frequency for gconvectiveh model where W expulsion is modelled by an increase in the outward plasma velocity. In Ref.[35], the effects of ELMs in ASDEX-Upgrade tokamak have been studied by 1D radial transport code (STRAHL code [39] with neoclassical transport parameters calculated by using the NEOART code[40] and with a relatively simple model for the impurity transport loss along the field line in the SOL. The modeling results show that the impurity confinement time in the core shows a strong decrease with increasing ELM frequency as experimentally observed. The authors of Ref. [35], however, have pointed out that there is an equally strong dependence on the characteristic parallel loss time in the SOL. This statement indicates 2D simulations in the SOL is needed to evaluate impurity content during the ELM in more sophisticated manner.

Although studies of the effects of neoclassical transport and ELMs are beyond the scope of the present paper, IMPGYRO has a potential to study these effects in the future together with more sophisticated modeling of the background plasma by SOLPS-ITER code suite with SOLPS version 5.2 including the effects of drifts, the H-mode edge transport barrier (ETB) of ITER and so on discussed above.

5.4.3 Other effects/simplifications

In addition to important effects discussed above, there still exist several effects and simplifications which could alter the results obtained in this first application of IMPGYRO code to ITER plasmas. Here we list up these effects and simplifications /assumptions and give brief discussion for further study.

Core-Interface-Boundary (CIB) condition

As mentioned in Sec. 5.2, all the Monte Carlo test particles reaching the core boundary are assumed to be absorbed. This simplification provides an effective sink for tungsten and could have an impact on the amount of tungsten in the simulation domain. In order to evaluate more precisely the amount of tungsten in the simulation domain, it will be necessary to make an integrated core-pedestal-SOL modeling with impurity core-transport code as in Ref. [15] and it is beyond the scope of present analysis.

Trace Impurity Limit

As mentioned in Sec. 5.2, the trace impurity limit has been assumed, i.e., the background plasma parameters have been fixed and assumed not to be affected by the W impurities. As seen from Fig. 5.4(a) an (b), the W densities are considerably smaller than the background electron density ($n_\mathrm{W}/n_\mathrm{e} \sim 10^{-5} - 10^{-4}$) in most of the calculation domain. Therefore, the trace impurity limit seems to be reasonable assumption in the present first application of the IMPGYRO code to ITER plasmas. Even such a small amount of the W-concentration, however, the radiation loss could not be neglected. Therefore, effects of impurity on the background plasma have to be considered and self-consistent coupling of the IMPGYRO code with the SOLPS-ITER code suite will be necessary in the future. Now the integration of the IMPGYRO code into the SOLPS-ITER code, i.e., SOLPS-ITER-IMPGYRO coupling is undergoing [41]. The coupling code is also necessary for the study of ELMs discussed in Sec.4.2.

Anomalous transport of impurities

There still exist large uncertainties concerning anomalous transport of impurities. In most of the modeling studies by both fluid model and kinetic Monte-Carlo model, it has been assumed that anomalous diffusion coefficient for impurity ions across the magnetic field is the same as that of the background ions. In this study, the same assumption and anomalous diffusion coefficient $D_\perp$ = 0.3 m^2/s have been used. In addition, recently it has been pointed out non-diffusive transport of the background plasma in the SOL, i.e., so-called plasma blob and hole possibly affect the impurity transport [42]. The radial profiles and the core penetration of impurities depend on these effects. Sensitivity study of the results on these anomalous transport model as well as the effects of neoclassical transport in the H-mode ETB and ELMs will be needed in the future.

5.5 Summary of Chapter 5

The global W impurity transport calculation of ITER, tracking the full-orbit of W has been performed by means of the IMPGYRO code for two cases of the background plasma parameters calculated by SOLPS-ITER code suite. This is the first application of IMPGYRO to calculate the W transport in the ITER operating scenario. The cases are set to be: the partially detached state in the outer divertor (Case A), and the high recycling state in the outer divertor (Case B) which have been obtained by changing the injection rate of D_2 and Ne from the gas puff port with a fixed input power of 100MW into the SOL equally shared between ions and electrons.

Under the assumptions described in Sec. 5.2, and also under the limitations and the validity range of the model discussed in Sec. 5.4, the following results have been obtained.

In Case A, since the electron temperature is still high enough to sputter out the W, a little amount of W impurities is sputtered out mainly from the outer baffle. However, none of the sputtered W particles manage to transport toward the upstream SOL because the net force directs them toward the divertor plates.

In Case B, on the other hand, W particles which have been sputtered out from the region near the outer strike point have been transported toward the top region of the SOL mainly due to the strong thermal force directed toward the top region of the SOL. After passing through the mid-plane, they are decelerated due to the reversed temperature gradient and the resultant change of the thermal force direction. Then the W particles stagnates where the temperature gradient becomes zero and finally the radial transport by the anomalous diffusion and the grad-B drift become relatively important.

The results show that the W impurities in the upstream SOL strongly depends on the divertor operation mode. From the comparison of the W sputtering source and the W impurity transport between the partially detached state (Case A) and the high recycling state (Case B), we have clarified the effectiveness of obtaining a partially detached state to reduce the W impurities in the upstream SOL.

In the present first application of the IMPGYRO code to ITER plasmas, however, several important effects have been neglected, as have been already discussed in detail in Sec. 5.4.: (i)simplifying assumptions have been made for calculating the W sputtering yield, such as the incident angle of Ne has been assumed to be normal, the self-sputtering of W has been neglected, (ii) we have neglected the drifts of the background plasma and the resultant neoclassical transport of impurities (IWP and TSE), (iii) effects of the H-mode edge transport barrier and ELMs, (iv) employing the absorbing boundary condition for W, (v) the background plasma has been assumed to be fixed, i.e. the trace impurity limit has been assumed. These effects will be investigated in the near future.

References in Chapter 5

[1] S. Yamoto, *et al.*, Nucl. Fusion **57** (2017) 116051.

[2] P.C. Stangeby, *et al.*, Nucl. Fusion **28** (1988) 1945.

[3] K. Shimizu, *et al.*, J. Nucl. Mater. **241-3** (1997) 167.

[4] D. Reiser, *et al.*, Nucl. Fusion **38** (1998) 165.

[5] I. Hyodo, *et al.*, J. Nucl. Mater. **313-6** (2003) 1183.

[6] A. Fukano, *et al.*, J. Nucl. Mater. **363-5** (2007) 211.

[7] T. Takizuka, *et al.*, J. Comput. Phys. **25** (1977) 205.

[8] Y. Homma, A. Hatayama, J. Comput. Phys. **231** (2012) 3211.

[9] Y. Homma, A. Hatayama, J. Comput. Phys. **250** (2013) 206.

[10] D. Naujoks, *et al.*, Nucl. Fusion **33**, (1993) 581.

[11] A. Kirshner, *et al.*, J. Nucl. Mater. **463** (2015) 116.

[12] K. Schmid, *et al.*, J. Nucl. Mater. **363-5** (2007) 674.

[13] S. Wiesen, *et al.*, J. Nucl. Mater. **463** (2015) 480.

[14] X. Bonnin, *et al.*, Plasma Fusion Res. **11** (2016) 1403102.

[15] H.D. Patcher, *et al.*, J. Nucl. Mater. **463** (2015) 591.

[16] A.S. Kukushkin, *et al.*, Fusion Eng. Des. **86** (2011) 2865.

[17] G.A. Emmert, *et al.*, Phys. Fluids **23** (1980) 803.

[18] W. Eckstein, IPP-Report 9/117, Garching, Max Planck Institute for Plasma Physics (1998).

[19] Y. Homma, *et al.*, Nucl. Fusion **56** (2016) 03609.

[20] S.I. Braginskii, *Transport processes in a plasma, in: M.A. Leontovich (Ed.), Reviews of Plasma Physics*, vol. 1, Consultants Bureau, New York (1965).

[21] P.C. Stangeby, *The Plasma Boundary of Magnetic Fusion Devices*, Institute of Physics, Bristol (2000).

[22] P.I.H. Cooke, *et al.*, Nucl. Fusion **27** (1987) 1165.

[23] S. Yamoto, *et al.*, J. Nucl. Mater. **463** (2015) 615.

[24] G. Kawamura, *et al.*, Contrib. Plasma Phys. **48** (2008) 126.

[25] R. Khaziev, *et al.*, Phys. Plasmas **22** (2015) 043503.

[26] R. Dux, *et al.*, J. Nucl. Mater. **390-1** (2009) 858.

[27] J. Roth, *Physical sputtering of solids at ion bombardment, Physics of Plasma-Wall Interactions in Controlled Fusion*, NATO ASI Series, Prenum Press, New York (1984).

[28] D. Naujoks, *et al.*, Nucl. Fusion **36** (1996) 671.

[29] A.V. Chankin, *et al.*, Plasma Phys. Control. Fusion **56** (2014) 025003.

[30] K. Hoshino, *et al.*, J. Nucl. Mater. **390-1** (2009) 168.

[31] V.A. Rozhansky, *et al.*, Nucl. Fusion **41** (2001) 387.

[32] V.A. Rozhansky, *et al.*, Nucl. Fusion **49** (2009) 025007.

[33] N. Asakura, *et al.*, J. Nucl. Mater. **363-5** (2007) 41.

[34] R. Dux, *et al.*, Plasma Phys. Control. Fusion **56** (2014) 124003.

[35] R. Dux, *et al.*, Nucl. Fusion, **51** (2011) 053002.

[36] H. Inoue, *et al.*, Contrib. Plasma Phys. **56** (2016) 634.

[37] D.P. Coster, *et al.*, J. Nucl. Mater. **463** (2015) 620.

[38] R. Schneider, *et al.*, Contrib. Plasma Phys. **46** (2006) 3.

[39] R. Dux, IPP-Report, 10/30, Max Planck Institute for Plasma Physics (2006).

[40] A.G. Petters, Phys. Plasmas **7** (2000) 268.

[41] S. Yamoto, *et al.*, *IMPGYRO: development and coupling to SOLPS-ITER*, private communication (2016).

[42] H. Hasegawa, *et al.*, Nucl. Fusion **57** (2017) 116008.

Chapter 6

Conclusion

To obtain continuous D-T fusion reaction in the tokamak plasma, the impurity transport process in the Scrape-Off Layer (SOL)/divertor region and the penetration process into the fusion core plasma must be understood/controlled. Especially, with the move in current and future fusion devices to all-metal walls, and particularly with tungsten (W) plasma-facing components, understanding heavy ion impurity transport processes in the SOL/divertor region is becoming one of the most critical issues for tokamak operation.

In this thesis, aiming to develop the reliable impurity transport code which can be used for designing fusion reactors, Monte-Carlo heavy metal impurity transport code IMPGYRO has been improved and applied to the predictive W transport simulation of the ITER.

In Chapter 1, the introduction of this study is given. The basic mechanism of tokamak fusion reactors, the influence of the core concentration of the W impurities on the core plasma performance, and transport process of the W impurity are explained.

In Chapter 2, the physical model of the multi-species plasma transport code SOLPS-ITER and the W impurity transport code IMPGYRO, which are used in this study, is explained.

In Chapter 3, the W impurity transport process parallel to the magnetic field line is discussed by focusing on the effects of the thermal force and the friction force. The results show that the transport direction of the W impurities is mainly determined by the balance between the friction force and the thermal force.

In Chapter 4, the detailed analysis of the W penetration process into the core discussed in Chapter 3 has been performed. The model improvement of the IMPGYRO code has been achieved by implementing the cross-field neoclassical transport model into the IMPGYRO code. The perpendicular fluxes of W has been examined by comparing a conventional guiding center model and the improved IMPGYRO. The perpendicular flux of W from IMPGYRO tend to be larger than those from the guiding center model. The result suggests that the core penetration of W possibly takes place by the neoclassical transport.

In Chapter 5, the predictive simulation of the W impurity transport in the ITER operation scenario has been performed. The W impurity transport has been compared between different typical ITER operation scenarios, (A) the high recycling state, and (B) the partially detached state in the outer divertor plate, calculated by the SOLPS-ITER code. In both cases, W impurities are sputtered from the baffle region. However, none of the sputtered W impurities manage to penetrate into the core. In the high recycling state, the W impurities sputtered from the region near the strike point have been transported to the upstream SOL region. The important information of W impurity transport for the ITER plasma operations has been achieved.

In Chapter 6, the achievements obtained by this study are summarized.

Future work

Of course, not the whole problems have been solved by this study. For example, as discussed in Chapter 5, the W transport simulation has been performed under the various simplifications. Also, the validity of the IMPGYRO calculation results has not been sufficiently discussed yet. In this section, such problems which should be set as a short-term goal are summarized. Also, the ongoing works related to resolve the issues discussed below are briefly introduced.

Modeling improvements

1) Drifts of the background plasma species and neoclassical transport

   As mentioned in Sec. 5.2, the present study is based on the SOLPS-ITER code suite with SOLPS version 4.3 and effects of the drifts for the background plasmas have been neglected. As has been pointed out in Refs.[1, 2] with SOLPS version 5.2, the drifts largely affect the flow-velocity distribution of the background plasmas in the SOL. In order to reproduce more realistic flow patterns observed in the experiments [[3], and references therein], it is necessary to take into account the effects of drifts.

   The change in the background flow pattern in the SOL affects the friction force on impurities. The drifts can also produce convective heat flows. As a result, ion temperature profiles and the resultant thermal force distribution on impurities are possibly altered.

2) Self-sputtering of W

   We have neglected the effect of W self-sputtering in this study. The systematic analysis of prompt re-deposition and W self-sputtering will be required in the future. However, a part of the work is undergoing. For example, the W self-sputtering model has already imprenented into the IMPGYRO code and it has been used for the fusion DEMO designing, particularly, the IMPGYRO with W self-sputtering model has been used for the estimation of the W-wall erosion [4].

3) Self-consistent calculation of background plasma and W impurities

In order to evaluate the heat load toward the divertor plate including W radiation, the development of the SOLPS-ITER IMPGYRO coupled code will be required. So far, the coupled code development has been performed under the collaboration between ITER Organization and Keio University.

4) IMPGYRO coupling to a core W impurity transport code

The coupling of IMPGYRO with a core W impurity transport code enables to set more proper CIB which has been assumed to be absorbed in the study in Chapter 5. Also, The concentration of W^{+44} and W^{+45} in the core can be compared between the photometry analysis and the simulation result.

Code validation

1) Validation of the local transport processes

The amount of W redeposited to the divertor plates has been analyzed in the Large Helical Device (LTD)[5] and the JT-60U W tile experiment[6]. The experimental datas and the IMPGYRO simulation results can be compared to validate the local transport process of IMPGYRO.

2) Validation of the global transport processes

The photometry analysis of W line emission has been studied in a number of devices[7, 8, 9, 10]. In these experiments, the line emissions of W^0, W^{+44}, and W^{+45} have been observed. Neutral W atoms (W^0) are mainly localized in the vicinity of the divertor plates. On the other hand, W^{+44}, and W^{+45} are the typical charge states of W in the core region. Though it is indirect validation of the IMPGYRO in the tokamak edge regions, the comparison between experiments can be performed in following way: (i) compare W^0 density distributions with the line emission observed, and (ii) compare W^{+44}, and W^{+45} density distributions against the line emissions. This process makes it possible to validate the IMPGYRO code for a certain extent. More direct comparison might be possible if the line emissions of the typical charge states in the SOL region, W^{+10} to W^{+20}, in particular, can be observed. In order to do so, more discussions with experimentalists are needed.

Applicability of this study

1) Better understandings of the W impurity transport processes

The results obtained in Chapter 5 can be used as the reference case of the further W transport with more precise options: (i) the SOLPS-ITER background plasma calculation including the drifts of the background plasma, which enables to calculate W transport with neoclassical effects, (ii) the consideration of the W self-sputtering, which gives the consistent boundary condition of W transport on the divertor plates, and (iii) the self-consistent calculation by SOLPS-ITER IMPGYRO coupled code, which allows SOLPS-ITER to consider the radiation cooling of W, for example. Step-by-step analysis of the effects mentioned in the section ”Modeling improvements” above by comparing with the reference case can improve the understandings of the W transport processes.

2) Contribution to the future fusion reactor designing

   The IMPGYRO can be used as a tool to analyse the core-divertor consistency, i.e., evaluate both the heat load to the divertor, and the W core concentration ratio. The evaluation of the heat load toward the divertor can be performed by the SOLPS-ITER IMPGYRO coupled code. However, in order to do that, further improvements of the SOLPS-ITER IMPGYRO coupling scheme is necessary. As for the analysis of the W core concentration, this can be done by coupling the IMPGYRO code with a core W impurity transport code such as ASTRA[11] and STRAHL[12] code.

References in Chapter 6

[1] V.A. Rozhansky, *et al*., Nucl. Fusion **41** (2001) 387.

[2] V.A. Rozhansky, *et al*., Nucl. Fusion **49** (2009) 025007.

[3] N. Asakura, *et al*., J. Nucl. Mater. **363-5** (2007) 41.

[4] Y. Homma, *et al*., Nuclear Materials and Energy, **12** (2017) 323.

[5] M. Tokitani, *et al*., J. Nucl. Mater. **415** (2011) S87.

[6] Y. Ueda, *et al*., Nucl. Fusion **49** (2009) 065027.

[7] T. Nakano, *et al*., J. Phys. B: At. Mol. Opt. Phys. **48** (2015) 144023.

[8] T. Nakano, *et al*., J. Nucl. Mater. **415** (2011) S327.

[9] T. Pütterich, *et al*., Plasma Phys. Control. Fusion **50** (2008) 085016.

[10] T. Pütterich, *et al*., Nucl. Fusion **50** (2010) 025012.

[11] G. Pereverzev, P.N. Yushmanov, IPP-Report 5/98, Garching, Max Planck Institute for Plasma Physics (2002).

[12] K. Behringer, Rep. JET-R(87)08, JET Joint Undertaking, Abingdon (1987).

Acknowledgement

First of all, I would like to express the deepest appreciation to my supervisor Professor Dr. Akiyoshi Hatayama. He guided me through my Master course and Ph.D. course research, and taught me the joy of science. His knowledge about the plasma physics and the nuclear fusion, his enthusiasm and commitment, and his clear advices have always encouraged me to continue the study. And I also thank him to have given me precious chances to participate in many academic conferences and to do an internship at ITER Organization.

I would like to express my gratitude to Associate Professor Dr. Kohei Yokoi, Professor Dr. Kunihiko Okano, and Associate Professor Dr. Nobuhiko Nakano of Keio University for their helpful comments on this dissertation.

I would like to thank Dr. Tomonori Takizuka, Dr. Katsuhiro Shimizu, Dr. Gakushi Kawamura, Dr. Ryutaro Kanno, Dr. Nobuhiko Hayashi, Dr. Kazuo Hoshino, and for fruitful discussions and comments.

I would like to express my gratitude to Dr. Xavier Bonnin and Dr. Richard A. Pitts for supervising me during the internship at ITER Organization and the continuous efforts through my Ph. D. course research. I would also like to thank all the menbers at Science Division at ITER Organization.

I also appreciate very much the support from Professor Dr. Toshihisa Ueda, Professor Dr. Yasushi Kiyoki and Dr. David Campbell who gave me the opportunity to stay at ITER Organization (St-Paul-Lez-Durance, France) for 6 months, in the framework of Global Environmental System Leaders program.

I would like to thank all the members of Hatayama laboratory of Keio University. Especially, I would like to express my gratitude to Mr. Shu Nishioka and Mr. Kenjiro Nishida. My campus life was made so cheerful, active and splendid with them. In addition, I would like to thank Ms. Ryoko Tatsumi and Mr. Tomoyuki Maeda for taking over the maintainer of the computational environments.

This work was supported by Grant-in-Aid for JSPS (Japan Society for the Promotion of Science) Fellows.

Finally I would like to show my greatest appreciation to my parents for their support and encouragement.

List of Publications

(1) Articles on periodicals (related to thesis)

1. S. Yamoto, K. Hoshino, M. Toma, Y. Homma, A. Hatayama, X. Bonnin, D. Coster, R. Schneider, *Systematic Study of Tungsten Impurity Transport in Representative Regimes of Divertor Plasma*, Contributions to Plasma Physics, **54**, 421-425 (2014).
2. S. Yamoto, Y. Homma, K. Hoshino, Y. Sawada, A. Hatayama, X. Bonnin, D. Coster, R. Schneider, *Effects of background plasma characteristics on tungsten impurity transport in the SOL/divertor region using IMPGYRO code*, Journal of Nuclear Materials, **463**, 615-619 (2015).
3. Y. Homma, S. Yamoto, Y. Sawada, H. Inoue and A. Hatayama, *Kinetic modeling for neoclassical transport of high-Z impurity particles using Binary Collision Method*, Nuclear Fusion, **56**, 036009 (2016).
4. S. Yamoto, Y. Homma, H. Inoue, Y. Sawada, K. Hoshino, A. Hatayama, X. Bonnin, D. Coster, R. Schneider, *Effects of classical and neo-classical cross-field transport of tungsten impurity in realistic tokamak geometry*, Contributions to Plasma Physics, **56**, 646-650 (2016).
5. S. Yamoto, X. Bonnin, Y. Homma, H. Inoue, K. Hoshino, A. Hatayama, R.A. Pitts, *Kinetic modeling of the high-Z tungsten impurity transport in ITER plasmas using the IMPGYRO code in the trace impurity limit*, Nuclear Fusion, **57**, 116051 (2017).

(2) Other articles on periodicals

1. Y. Homma, A. Hatayama, Y. Sawada, S. Yamoto, *Test Simulations of Temperature Screening Effect by using Kinetic Monte Carlo Model, Plasma and Fusion Research*, **9**, 1403095 (2014).

2. H. Inoue, Y. Homma, S. Yamoto and A. Hatayama, *Extended Numerical Modeling of Impurity Neoclassical Transport in Tokamak Edge Plasmas, Contributions to Plasma Physics*, **56** 634-639 (2016).
3. Y. Homma, K. Hoshino, S. Yamoto, N. Asakura, S. Tokunaga, A. Hatayama, Y. Sakamoto, R. Hiwatari, K. Tobita and Joint Special Design Team for Fusion DEMO, *Numerical analysis of tungsten erosion and deposition processes under a DEMO divertor plasma and geometry, Nuclear Materials and Energy*, **12**, 323-328 (2017).

(3) Articles on international conference proceedings (reviewed full-length articles)

1. S. Yamoto, X. Bonnin, Y. Homma, H. Inoue, K. Hoshino, A. Hatayama, R.A. Pitts, *Kinetic modeling of impurity transport using the IMPGYRO code*, in Proc. Of the 26th IAEA Fusion Energy Conference, TH/P6-23, Kyoto, Japan (2016).

(4) Presentations at international conferences

1. S. Yamoto, K. Hoshino, M. Toma, Y. Homma, A. Hatayama, X. Bonnin, D. Coster, R. Schneider, *Systematic Study of Tungsten Impurity Transport in Representative Regimes of Divertor Plasma*, 14th International Workshop on Plasma Edge Theory in Fusion Devices, Cracow, Poland (2013/Sep./23-25). (Poster presentation)
2. S. Yamoto, Y. Homma, K. Hoshino, Y. Sawada, A. Hatayama, X. Bonnin, D. Coster, R. Schneider, *Effects of background plasma characteristics on tungsten impurity transport in the SOL/divertor region using IMPGYRO code*, 21st International Conference on Plasma Surface Interactions, Kanazawa, Japan (2014/May/26-30). (Poster presentation)
3. Y. Homma, Y. Sawada, S. Yamoto, A. Hatayama, *Kinetic Modeling of Classical And Neo-Classical Transport for High-Z Impurities in Fusion SOL/Divertor Plasma Using Binary Collision Method*, The 25th IAEA Fusion Energy Conference (IAEA CN-221), Saint Petersburg, Russian Federation (2014/Oct./13-18). (Poster presentation)
4. S. Yamoto, Y. Homma, H. Inoue, Y. Sawada, K. Hoshino, A. Hatayama, X. Bonnin, D. Coster, R. Schneider, *Effects of classical and neo-classical cross-field transport of tungsten impurity in realistic tokamak geometry*, 15th International Workshop on Plasma Edge Theory in Fusion Devices, Nara, Japan (2015/Sep./9-11). (Poster presentation)

5. S. Yamoto, X. Bonnin, Y. Homma, S.W. Lisgo, H. Inoue, A. Hatayama, R.A. Pitts, *IMPGYRO: Development and coupling to SOLPS-ITER*, 22nd International Tokamak Physics Activity Divertor Scrape-Off Layer Topical Group Meeting, Frascati, Italy (2016/Jan./25-28). (Oral presentation)

6. S. Yamoto, X. Bonnin, Y. Homma, H. Inoue, K. Hoshino, A. Hatayama, R.A. Pitts, *Kinetic Modeling of impurity transport using the IMPGYRO code*, The 26th IAEA Fusion Energy Conference (IAEA CN-234), Kyoto, Japan (2016/Oct./17-22). (Poster presentation)

7. S. Yamoto, X. Bonnin, Y. Homma, S.W. Lisgo, A. Hatayama, R.A. Pitts, *W transport simulations in divertor and SOL plasma using IMPGYRO and benchmark against DIVIMP*, The 23rd International Tokamak Physics Activity Divertor Scrape-Off Layer Topical Group Meeting, Naka, Japan (2016/Oct./24-27). (Oral presentation)

8. Y. Homma, and S. Yamoto, *Numerical analysis on prompt redeposition of tungsten impurity*, The 23rd International Tokamak Physics Activity Divertor Scrape-Off Layer Topical Group Meeting, Naka, Japan (2016/Oct./24-27). (Oral presentation)

(5) Presentations at domestic meetings

1. S. Yamoto, K. Hoshino, Y. Homma, A. Hatayama, X. Bonnin, D. Coster, R. Schneider, *Systematic Study of Tungsten Impurity Transport in Representative Three Regimes of Divertor Plasma*, 30th Annual Meeting of The Japan Society of Plasma Science and Nuclear Fusion Research, Meguro, Tokyo (2013/Dec.). (Poster presentation)

2. S. Yamoto, K. Hoshino, Y. Homma, A. Hatayama, X. Bonnin, D. Coster, R. Schneider, *Modeling of thermal force acting on fusion SOL plasma: comparison between kinetic thermal force and fluid thermal force*, 10th Rengo-Kouenkai on Nuclear Fusion Energy, Tsukuba, Ibaraki (2014/Jun.). (Poster presentation)

3. S. Yamoto, K. Hoshino, Y. Homma, A. Hatayama, X. Bonnin, D. Coster, R. Schneider, *Effects of drifts on W impurity transport codes: Benchmark between IMPGYRO and DIVIMP*, 33rd Annual Meeting of The Japan Society of Plasma Science and Nuclear Fusion Research, Meguro, Tokyo (2016/Nov.). (Poster presentation)

(6) Others

1. JT-60 Best Collaborator Award (2014).